

Determination of characteristic turbulence length scales from large-eddy simulation of the convective planetary boundary layer

Von der Fakultät für Physik und Geowissenschaften
der Universität Leipzig
genehmigte

DISSERTATION

zur Erlangung des akademischen Grades

DOCTOR RERUM NATURALIUM

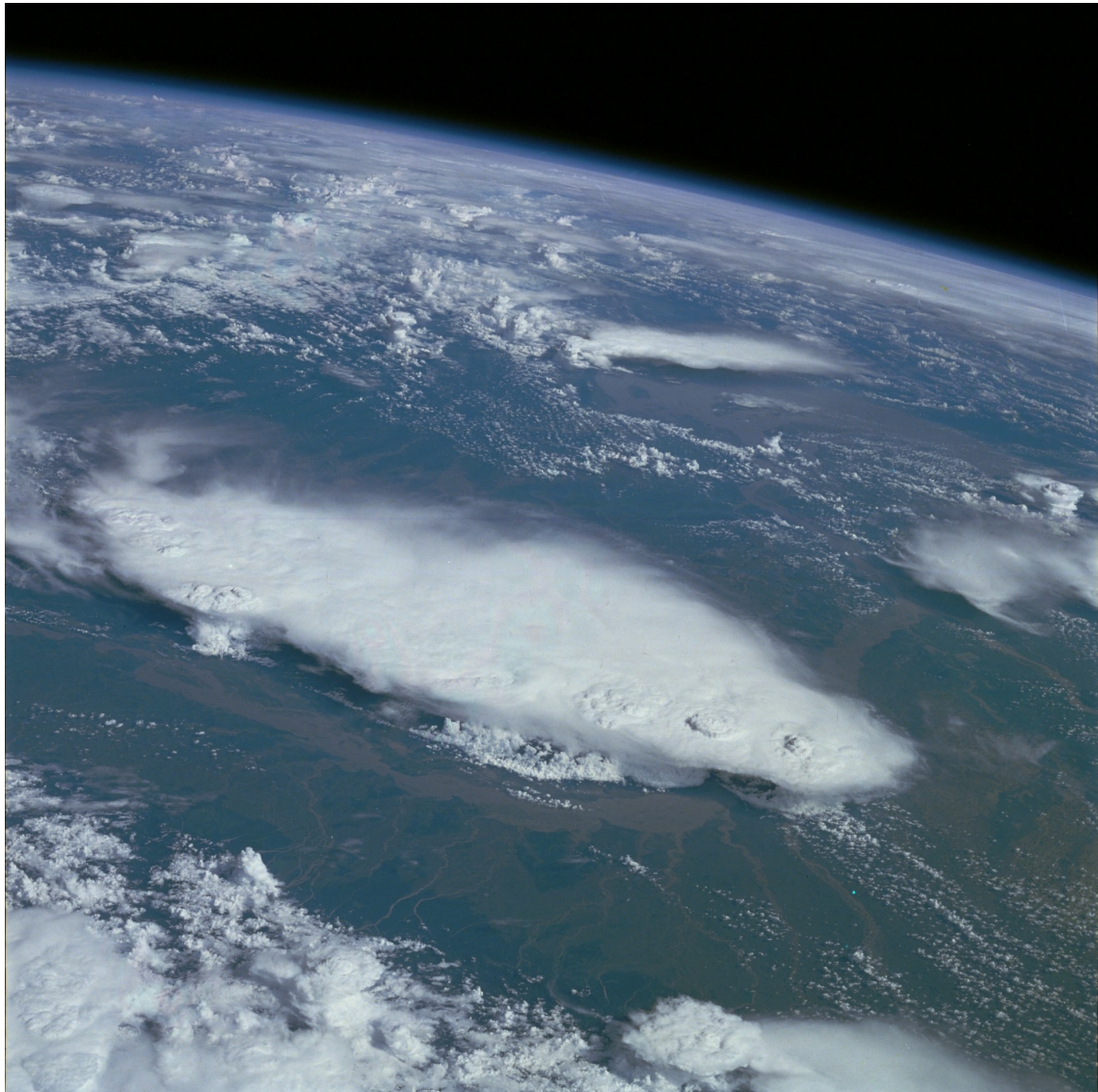
Dr. rer. nat.

vorgelegt

von Diplom – Physiker Jürgen Helmert
geboren am 2. September 1973 in Karl-Marx-Stadt jetzt Chemnitz

Gutachter: Prof. Dr. rer. nat. habil. Eberhard Renner
 Priv. Doz. Dr. rer. nat. habil. Andreas Chlond
 Dr. sc. nat. habil. Hans-Joachim Herzog

Tag der Verleihung: 15. September 2003



Monsoonal thunderstorms observed in Bangladesh & India July 1985 (NASA Photo-Gallery: Photo No.: STS51F-31-0069) taken from above the eastern Himalaya Mountains looking southeast across the floodplain of the Brahmaputra River and the cloud-covered Khasi Hills into the Bay of Bengal. A well-developed cluster of mature monsoonal thunderstorms over the Khasi Hills (centre of photograph) can be seen. A variety of meteorological phenomena, strong related to turbulent processes in the moist-convective atmosphere are visible, such as overshooting thunderstorm tops, towers, squall lines, and areas of probable high-speed downdrafts or microbursts.

Zusammenfassung der wissenschaftlichen Ergebnisse zur Dissertation

**Determination of characteristic turbulence length scales
from large-eddy simulation of the convective
planetary boundary layer**

(Bestimmung charakteristischer Turbulenzlängenskalen aus
Grobstruktursimulationen der konvektiven planetaren Grenzschicht)

der Fakultät für Physik und Geowissenschaften der Universität Leipzig
eingereicht von

Diplom – Physiker Jürgen Helmert

angefertigt am
Leibniz – Institut für Troposphärenforschung, Leipzig, Abteilung Modellierung

April 2003

Einleitung und Zielsetzung

Die numerische Simulation der komplexen Dynamik von nichtlinear gekoppelten physikalischen und chemischen Prozessen in der Erdatmosphäre stellt eine enorme Herausforderung für dynamische Atmosphärenmodelle dar. In gegenwärtig eingesetzten meso- und globalskaligen Atmosphärenmodellen werden turbulente Austauschprozesse in der atmosphärischen Grenzschicht als subskalige Prozesse behandelt, die unter Verwendung geeigneter Schließungsansätze parametrisiert werden müssen. Diese Prozesse besitzen jedoch eine zentrale Bedeutung für den vertikalen Materie-, Impuls-, und Wärmetransport in der Atmosphäre. Durch die Beeinflussung von Wasserdampf- und Aerosolverteilung [7] sind turbulente Austauschprozesse in der Lage, die raumzeitliche Entwicklung von Wolken zu modulieren, was zu erheblichen Veränderungen der Strahlungsbilanz der Erde führen kann.

Gegenwärtig in Atmosphärenmodellen verwendete Ansätze zur Parametrisierung des Einflusses subskaliger Turbulenz auf prognostizierte hydro- und thermodynamische Felder basieren vornehmlich auf einer lokalen Schließung [18]. Bei solchen Schließungsverfahren spielt die Spezifizierung der turbulenten Mischungslänge in Abhängigkeit vom Stabilitätszustand der Atmosphäre eine entscheidende Rolle. Lokale Schließungen nutzen häufig diagnostische Gleichungen der turbulenten Mischungslänge für neutrale Schichtung [2] in Verbindung mit dimensionslosen Stabilitätsfunktionen [19]. Diese Beschreibung turbulenter Mischungsprozesse zeigt jedoch Defizite sowohl im oberen Bereich der konvektiven Grenzschicht als auch innerhalb der Entrainmentzone, da dort starke vertikale Gradienten der Strömungsvariablen auftreten [1].

In früheren Arbeiten [23, 4] wurde deshalb die Bestimmung charakteristischer Turbulenzlängenskalen aus spektralen Eigenschaften der turbulenten kinetischen Energie vorgenommen [11]. Dies wird allgemein als ein möglicher Ansatz für eine verbesserte Beschreibung turbulenter Austauschprozesse betrachtet. Eine Anwendung empirischer Turbulenzlängenskalen in lokalen Schließungsverfahren erfordert jedoch die Bestimmung der charakteristischen Turbulenzlängenskalen für ein breites Spektrum von atmosphärischen Stabilitätszuständen.

Charakteristische Turbulenzlängenskalen, die aus Messungen in der Atmosphäre [3, 15, 5] oder Laborexperimenten [13] bestimmt wurden, sind in der Regel nur für einen eingeschränkten Parameterraum repräsentativ. Aufgrund der Nichtlinearität turbulenter Prozesse ist eine Extrapolation von Messergebnissen auf andere Stabilitätszustände nur sehr eingeschränkt möglich. In den letzten Jahren wurden daher charakteristische Turbulenzlängenskalen aus hochaufgelösten Grobstruktursimulationen bestimmt [14, 22].

In der hier vorgestellten Arbeit wurden charakteristische Turbulenzlängenskalen anhand von Grobstruktursimulationen für ein weites Spektrum von Stabilitätsbedingungen bestimmt. Hierbei wurden hochaufgelöste dreidimensionale Simulationen sowohl der trockenen als auch der feuchten, bewölkten Grenzschicht durchgeführt. In substanzieller Erweiterung bisheriger Arbeiten auf diesem Gebiet [6, 14, 22] wurden die abgeleiteten Turbulenzlängenskalen mittels nichtlinearer Datenmodellierung approximiert und die erhaltenen Ergebnisse in die Turbulenzparametrisierung eines mesoskaligen Atmosphärenmodells integriert.

Methoden

Der verwendete methodische Ansatz umfasst im wesentlichen drei Aspekte:

1.
 - Grobstruktursimulationen konvektiver atmosphärischer Grenzschichten unter Verwendung unterschiedlicher Anfangs- und Randwerte. Spektrale Analyse der Simulationsdaten und Bestimmung charakteristischer Turbulenzlängenskalen von Vertikalgeschwindigkeit, Temperatur und Feuchte.
 - Bestimmung charakteristischer Turbulenzlängenskalen von Vertikalgeschwindigkeit, Temperatur und Feuchte aus der spektralen Analyse der Simulationsdaten.
 - Verifizierung der Ergebnisse durch Vergleich mit weiteren numerischen Simulationen, mit Turbulenzmessungen in der atmosphärischen Grenzschicht und mit Laborexperimenten [8].
2.
 - Statistische Analyse der abgeleiteten Turbulenzlängenskalen.
 - Validierung existierender Ansätze und Entwicklung einer Mischungslängenparametrisierung durch nichtlineare Approximation der charakteristischen Turbulenzlängenskalen auf der Basis leicht verwendbarer analytischer Funktionen.
 - Bestimmung der freien Funktionsparameter in Abhängigkeit vom Stabilitätszustand der Grenzschicht und Untersuchung der statistischen Signifikanz der neuen Parametrisierung.
 - Verifizierung der entwickelten Mischungslängenparametrisierung in einer lokalen Schließung anhand von Grobstruktursimulationen [10].

3.
 - Mesoskalige Sensitivitätsstudie zur Untersuchung des Einflusses der turbulenten Mischungslänge auf die Prognose hydro- und thermodynamischer Strömungsfelder in einem regionalen Vorhersagemodell (Lokalmodell des Deutschen Wetterdienstes).
 - Implementierung der durch Grobstruktursimulationen revidierten Turbulenzschließung in das Lokalmodell.
 - Vergleich mit der originalen Schließung anhand eines mesoskaligen Simulationsszenarios durch statistische Analyse der Modellfelder.
 - Verifizierung der Simulationsergebnisse [9] durch Satellitendaten unter Verwendung eines “Model-to-Satellite” – Verfahrens sowie durch Analysedaten aus der 4dVar – Datenassimilation des Lokalmodells.

Ergebnisse

1. Die Grobstruktursimulationen konvektiver atmosphärischer Grenzschichten ergaben Labilitätszustände in einem weiten Parameterbereich ($-z_i/L = 2 - 48$). Die Vertikalstruktur der berechneten Felder stimmt mit atmosphärischen Messungen überein und entspricht theoretischen Erwartungen. Sie ist durch eine Mischungsschicht mit nach oben anschließender Entrainmentzone charakterisiert. Spezifische Eigenschaften der simulierten Grenzschichten wurden anhand der ersten und zweiten statistischen Momente atmosphärischer Strömungsvariablen diskutiert. Insbesondere konnte durch die Untersuchung der Vertikalgradienten von horizontaler Windgeschwindigkeit, Temperatur und Feuchte das Auftreten von Entrainmentprozessen im oberen Bereich der Grenzschicht nachgewiesen werden. Ein Zusammenhang zwischen Entrainmentstärke und atmosphärischem Stabilitätszustand wurde aus den Ergebnissen der Grobstruktursimulationen ermittelt.

Die Spektraleigenschaften turbulenter Fluktuationen der Strömungsvariablen, das raumzeitliche Verhalten kohärenter Strukturen sowie charakteristische Turbulenzlängenskalen wurden abgeleitet. Die Untersuchung kohärenter turbulenter Strukturen von Vertikalgeschwindigkeit, Temperatur und Feuchte erfolgte mit Hilfe zweidimensionaler Autokovarianzen dieser Variablen in verschiedenen Ebenen der Grenzschicht. Mit diesem Verfahren wurden horizontale Rollenstrukturen in der konvektiven Grenzschicht nachgewiesen. Die Wellenlänge dieser Strukturen betrug in der Grenzschichtmitte etwa das Doppelte der Grenzschichthöhe und stimmt damit größenordnungsmäßig mit Flugzeugmessungen [16], Laborexperimenten [13] und anderen numerischen Simulationen [17] überein.

Auf der Grundlage horizontal gemittelter eindimensionaler Spektren und Autokorrelationen turbulenter Fluktuationen von Vertikalgeschwindigkeit, Temperatur und Feuchte wurden charakteristische Turbulenzlängenskalen berechnet. Als charakteristische Turbulenzlängenskalen für skalige Turbulenz wurden dabei die Wellenlänge des spektralen Peaks im turbulenten Energiespektrum als auch die integrale Autokorrelationslänge verwendet [11]. Berechnete Vertikalprofile dieser Turbulenzlängenskalen zeigten eine Abhängigkeit vom Stabilitätszustand der simulierten Grenzschicht. Ein empirisch aus Messdaten abgeleiteter Zusammenhang zwischen der Peakwellenlänge und der Autokorrelationslänge der Vertikalgeschwindigkeit konnte anhand der Grobstruktursimulationen bestätigt werden. Die Simulationsergebnisse zeigen einen ähnlichen Zusammenhang auch für Temperatur und Feuchte, was bislang aber noch nicht experimentell bestätigt wurde.

Die Verifizierung der charakteristischen Turbulenzlängenskalen ergab eine gute Übereinstimmung der Ergebnisse mit Resultaten aus numerischen Simulationen [14, 6] und atmosphärischen Messungen [5]. Der Vergleich der Ergebnisse mit Laborexperimenten [13] zeigte jedoch Abweichungen. Eine Unterschätzung der Stärke von Entrainmentprozessen in den Laborexperimenten [12] konnte als eine mögliche Ursache für die beobachteten Abweichungen identifiziert werden. Für eine abschließende Beurteilung der in Laborexperimenten gemessenen Turbulenzlängenskalen sind weitere Grobstruktursimulationen erforderlich.

2. Im Rahmen der statistischen Analyse wurde eine aus atmosphärischen Messungen abgeleitete Approximation der Wellenlänge des spektralen Maximums der Vertikalgeschwindigkeit mit Hilfe der Grobstruktursimulationen in einem erweiterten Stabilitätsbereich validiert. Eine neu entwickelte Approximation bildete die Basis für eine verbesserte Parametrisierung integraler Autokorrelationslängen in Abhängigkeit vom Stabilitätszustand der Atmosphäre. Diese Approximation verwendet analytische Funktionen mit freien Parametern und berücksichtigt spezifische Eigenschaften der Autokorrelationslängen in konvektiven Grenzschichten.

Durch nichtlineare Datenmodellierung wurden die freien Parameter in Abhängigkeit vom Stabilitätszustand der simulierten Grenzschicht ermittelt. Die durchgeführte statistische Analyse belegte die statistische Signifikanz des verwendeten Parametrisierungsansatzes. Dieses Ergebnis legt die Verwendung der parametrisierten integralen Autokorrelationslänge als turbulente Mischungslänge in einer lokaler Schließung nahe.

Die Verifizierung dieser Mischungslängenparametrisierung wurde auf der Grundlage von Grobstruktursimulationen für das lokale Schließungsmodell nach Mellor-Yamada (Level 2.5 [19]) durchgeführt [10]. Insbesondere in der oberen Grenzschicht sowie in der Entrainmentschicht konnte durch diesen Ansatz eine gegenüber dem diagnostischen Ansatz [2, 19] verbesserte Übereinstimmung der ersten und zweiten statistischen Momente subskaliger Turbulenz erzielt werden.

3. Die mesoskalige Sensitivitätsstudie zum Einfluss der turbulenten Mischungslänge auf prognostizierte hydro- und thermodynamische Felder wurde mit dem nichthydrostatischen mesoskaligen Lokal-Modell (LM) des Deutschen Wetterdienstes durchgeführt. Die Turbulenzschließung des LM basiert auf dem Mellor-Yamada-Modell Level 2.5 [21] und verwendet in der originalen Formulierung den diagnostischen Ansatz für die turbulente Mischungslänge in Verbindung mit dimensionslosen Stabilitätsfunktionen.

Das verwendete Szenario basiert auf Rand- und Anfangsdaten, die 24 Stunden der Intensivmessphase (18.06.1998) des LITFASS-98 Feldexperimentes repräsentieren. Anhand eines Modell-Modell-Vergleichs konnte der Einfluss der turbulenten Mischungslänge auf das raumzeitliche Verhalten parametrisierter subskaliger turbulenter Flüsse identifiziert werden. Diese zeigten besonders in der Entrainmentzone der voll entwickelten konvektiven Grenzschicht eine hohe Sensitivität gegenüber der turbulenten Mischungslänge.

Eine quantitative statistische Analyse der Simulationsergebnisse wurde für prognostizierte dreidimensionale Felder von Bewölkungsgrad, Wolkenwassergehalt und Wasserdampf sowie zweidimensionale Niederschlagsfelder durchgeführt. Eine hohe Sensitivität des Be-

wölkungsgrades und des Wolkenwassergehaltes gegenüber der turbulenten Mischungslänge konnte im oberen Bereich der Grenzschicht während des Zeitraums stärkster Konvektion nachgewiesen werden. Darüber hinaus ergab sich für den gleichen Zeitraum eine starke Beeinflussung konvektiv induzierter Niederschlagsereignisse [9].

Die Verifizierung der Simulationsergebnisse erfolgte durch die Auswertung von Satelliten- und Analysedaten aus der 4D-Datenassimilation. Die Satellitendaten umfassten gemessene Strahlungstemperaturen im infraroten Spektralbereich. Diese wurden mit synthetischen Satellitenbildern verglichen, die aus prognostizierten Modellvariablen des LM mit Hilfe eines Strahlungstransfermodells [20] berechnet wurden. Für die Verifizierung der Simulationen auf Basis der Datenassimilation standen nur Analysedaten bodennaher Felder sowie Daten des Bedeckungsgrades mit tiefen, mittelhohen und hohen Wolken zur Verfügung.

Ein Vergleich der Simulationsergebnisse anhand berechneter synthetischer Strahlungstemperaturen sowie Modellvariablen in der bodennahen Grenzschicht mit Satelliten- und Analysedaten zeigte erwartungsgemäß nur eine geringe Sensitivität gegenüber der turbulenten Mischungslänge. Die Verifizierung der prognostizierten Wolkenbedeckungsgrade wies jedoch für das betrachtete Simulationsszenario eine Verbesserung der Prognose des Bedeckungsgrades für tiefe Wolken nach. Bei Verwendung der revidierten turbulenten Mischungslänge ergab sich gegenüber dem originalen Ansatz eine Verbesserung um bis zu $\sim 11\%$ [9].

Ausblick

Eine statistisch abgesicherte Validierung der turbulenten Mischungslänge in meso- und globalskaligen Atmosphärenmodellen kann nur auf der Basis einer Vielzahl von Modellsimulationen, d.h. routinemäßig, erfolgen. Eine umfassende Verifizierung prognostizierter hydro- und thermodynamischer Felder erfordert zeitlich und räumlich hochauflösende Messdaten, insbesondere des Flüssigwassergehaltes, des Wasserdampfes sowie mikrophysikalischer Wolkenparameter.

Die erzielten positiven Ergebnisse bei der Integration charakteristischer Turbulenzlängenskalen in die Turbulenzschließung des LM legen eine Verwendung dieses Ansatzes in der operationellen Wettervorhersage nahe. Es ist daher beabsichtigt, den neuen Mischungslängenansatz einer umfangreichen Verifikation im Rahmen routinemäßiger Wettervorhersage zu unterziehen. Diese erfolgt in enger Kooperation mit der Abteilung Forschung und Entwicklung des Deutschen Wetterdienstes.

Die Untersuchungsergebnisse dieser Arbeit sind für ein breites Spektrum von dynamischen Atmosphärenmodellen anwendbar. Sie bilden die Grundlage einer verbesserten Berücksichtigung subskaliger turbulenter Austauschprozesse in diesen Modellen und tragen damit zu einer weiteren Erhöhung von Signifikanz und Zuverlässigkeit numerischer Modellsimulationen der Erdatmosphäre bei.

Literatur

- [1] S. Bélair, J. Mailhot, J. W. Strapp, and J. I. MacPherson. *J. Appl. Met.*, 38:1499–1518, 1999.

- [2] A. K. Blackadar. *J. Geophys. Res.*, 67:3095–3102, 1962.
- [3] S. J. Caughey and S. G. Palmer. *Quart. J. R. Meteorol. Soc.*, 105:811–827, 1979.
- [4] G. A. Degrazia, H. F. Campos Velho, and J. C. Carvalho. *Contr. Atmos. Phys.*, 70:57–64, 1997.
- [5] P. Durand, F. Thoumieux, and D. Lambert. *Quart. J. R. Meteorol. Soc.*, 126:1889–1912, 2000.
- [6] J. Graf and U. Schumann. *Meteorol. Rdsch.*, 43:140–148, 1991.
- [7] O. Hellmuth and J. Helmert. In *Air Pollution Modeling and Its Application XV*, 2002.
- [8] J. Helmert and O. Hellmuth. Biennial report 1999/2000, Institute for Tropospheric Research, Leipzig, 2000.
- [9] J. Helmert and O. Hellmuth. Biennial report 2001/2002, Institute for Tropospheric Research, Leipzig, 2002.
- [10] J. Helmert and O. Hellmuth. *Quart. J. R. Meteorol. Soc.*, 2003. eingereicht.
- [11] J. C. Kaimal and J. J. Finnigan. Oxford University Press, 1994.
- [12] R. Kaiser. Dissertation, Institut für Hydrologie und Wasserwirtschaft, Universität Karlsruhe (TH), 1996.
- [13] R. Kaiser and E. Fedorovich. *J. Atmos. Sci.*, 55:580–594, 1998.
- [14] S. Khanna and J. G. Brasseur. *J. Atmos. Sci.*, 55:710–743, 1998.
- [15] D. H. Lenschow and B. B. Stankov. *J. Atmos. Sci.*, 43:1189–1209, 1986.
- [16] F. Lohou, A. Druilhet, and B. Campistron. *Boundary-Layer Meteorology*, 89:407–444, 1998.
- [17] F. Lohou, A. Druilhet, B. Campistron, J.-L. Redelsperger, and F. Said. *Boundary-Layer Meteorology*, 97(3):361–383, 2000.
- [18] G. L. Mellor and T. Yamada. *J. Atmos. Sci.*, 31:1791–1806, 1974.
- [19] G. L. Mellor and T. Yamada. *Rev. Geophys. Space Phys.*, 20:851–875, 1982.
- [20] J. J. Morcrette. *Mon. Wea. Rev.*, 119:1205–1224, 1991.
- [21] M. Raschendorfer. Quarterly Report of the Operational NWP-Models of the Deutscher Wetterdienst – Special topic: The new turbulence parameterization of LM, Deutscher Wetterdienst, Business Area Research and Development, 1999.
- [22] M. Schröter, J. Bange, and S. Raasch. *Boundary-Layer Meteorology*, 95:437–456, 2000.
- [23] W. Y. Sun and C.-Z. Chang. *J. Climate Appl. Meteor.*, 25:1445–1453, 1986.

Contents

Contents	3
1 Introduction	5
2 Treatment of turbulent processes in atmospheric models	9
2.1 Turbulence parameterisation approaches	12
2.1.1 Local closure approximation	12
2.1.2 Non-local closure approximation	13
2.1.3 Counter-gradient approximation	13
2.2 Local closure approximation after Mellor-Yamada	14
2.3 Turbulent mixing length formulations	16
2.4 Characteristic turbulence length scales	18
2.4.1 Peak wavelength of the wavenumber weighted energy spectrum	21
2.4.2 Integral length scale	21
2.4.3 Dissipation length scale	22
2.4.4 Relations between characteristic turbulence length scales	23
3 Large-eddy simulation of convective boundary layers	25
3.1 Modelling system and setup	25
3.1.1 The MPI 3D large-eddy simulation model	25
3.1.2 Initial and boundary conditions	26
3.2 Properties of the large-eddy simulation database	29
3.2.1 Flow statistics	31
3.2.2 Examination of coherent structures	36
3.2.3 Examination of characteristic turbulence length scales	40
3.3 Verification of large-eddy simulation results	50
3.3.1 Verification against numerical simulations	50
3.3.2 Verification against atmospheric measurements	52
3.3.3 Verification against laboratory experiments	57
3.4 Turbulent mixing length formulation based on characteristic turbulence length scales	58
3.4.1 Approximation of peak wavelength and integral length scale	58
3.4.2 Verification of the new turbulent mixing length formulation	59

4	Mesoscale response to turbulent mixing length formulation	65
4.1	Modelling system and setup of LITFASS	65
4.1.1	The mesoscale non-hydrostatic limited area model	65
4.1.2	Initial and boundary conditions of LITFASS	66
4.2	Intercomparison of the LITFASS simulation results	70
4.3	Verification of the LITFASS simulation results	74
4.3.1	Verification against satellite data	74
4.3.2	Verification against model-analysis data	75
5	Conclusions and future directions	81
A	Non-linear least square fit parameters of peak wavelength and integral length scale	85
A.1	Peak wavelength of the vertical velocity	85
A.2	Integral length scale of the vertical velocity	86
A.3	Peak wavelength of the virtual potential temperature	87
A.4	Integral length scale of the virtual potential temperature	88
A.5	Peak wavelength of the total water content	89
A.6	Integral length scale of the total water content	90
B	Approximation of peak wavelength and integral length scale	91
B.1	Approximation of the peak wavelength	91
B.2	Approximation of the integral length scale	91
C	Nomenclature	95
D	List of Figures	101
E	List of Tables	103
	Bibliography	105

Introduction

Long term political and economical decisions are increasingly based on results of numerical model simulations. Therefore, an estimation of the reliability and significance of models is of great importance. One of the present-day major challenges for the scientific community poses the numerical simulation of the earth atmosphere due to the large complexity of atmospheric processes associated with non-linearity as well as large spatial and temporal variability. However, uncertainties in knowledge about atmospheric processes account for some gaps in our present day knowledge concerning the effects of global change. These effects are related to changes in the frequency and characteristics of extreme weather events, possible impacts on natural and social systems, and their implications for disaster prevention (WGBU, 1996).

Among the processes of high climate sensitivity, clouds are considered as one of the important factors regulating the current climate system and future climate change (Ramanathan *et al.*, 1989; Harrison *et al.*, 1990; Alekseev *et al.*, 1996). Due to their widespread and persistent occurrence, clouds are of fundamental importance to the global energy budget. Despite of the crucial role of clouds in the radiation balance of the atmosphere and earth's surface they are treated very crudely in most regional integrated models (RIM). However, RIMs are considered as a possible approach for climate impact research at regional scale (IPCC, 2002; WGBU, 1995). The meteorological part of RIMs is often based on mesoscale numerical weather prediction (NWP) models. Within the framework of RIMs, NWP models are used to investigate changes of the local and regional climate resulting from the interaction of large-scale circulation patterns, circulation systems induced by geographical and topographic factors, and smaller processes at the earth's surface, which are subject to anthropogenic influences (WGBU, 1996; Renner, 2002).

Turbulent processes taking place in the planetary boundary layer (PBL) strongly affect the global distribution of clouds by controlling the evaporation and redistribution of water vapour into the atmosphere (Garrat, 1993). In convective boundary layers (CBL), turbulent transports of momentum, heat, moisture, and other chemical species are associated with buoyant thermals. These turbulent structures influence mainly the development of low clouds. However, even low clouds are considered to have a large climate sensitivity (Gibson and Wielicki, 2002).

Due to their complexity, associated with large spatial and temporal variability, turbulent transports are not resolved in NWP models. Therefore, NWP models at regional and global scale have to use turbulence parameterisations to describe the impact of the non-resolved subgrid-scale (SGS) turbulent transports on the evolution of the dynamic and thermodynamic state of the atmosphere (Ayotte *et al.*, 1996) as well as on reactions of chemical species (Hellmuth and Helmert, 2002). Thus, development and improvement of parameterisation schemes for subgrid-scale turbulent transports is of primary importance and subject of comprehensive integrated stud-

ies (Müller *et al.*, 1995) including measurements as well as numerical simulations (see, e.g., Herzog *et al.* (2002a)).

Depending on scale and atmospheric stability a large number of parameterisation schemes different in degree of sophistication have been developed in the past decades (Stull, 1997). To keep the computational costs at an acceptable level, most turbulence parameterisation schemes in NWP models use the local closure approximation with varying orders of closure (Mellor and Yamada, 1974; Wyngaard and Coté, 1974; André *et al.*, 1978). However, local closure schemes show some deficiencies in simulations of buoyancy-driven convective boundary layers (Deardorff, 1972; Ebert *et al.*, 1989; Holtslag and Moeng, 1991; Chrobok *et al.*, 1992). Here, the primary part of turbulent transports is associated with coherent and organised structures (turbulent eddies) containing most of the turbulent energy. Therefore, several approaches have been developed to circumvent this problem. They are often based on counter-gradient closures (Deardorff, 1972; Mailhot and Benoit, 1982; Troen and Mahrt, 1986; Holtslag and Moeng, 1991; Cuijpers and Holtslag, 1998) or non-local closures (Stull, 1984; Wyngaard and Brost, 1984; Berkowicz, 1984; Fiedler and Moeng, 1985). However, these schemes are numerically expensive. This limits their application in NWP models with regional and global scale of interest. Therefore, the parameterisation of turbulent transports in present-days and also near-future NWP models is carried on with local closure approximation.

One of the most popular local closure schemes used in NWP models (Ayotte *et al.*, 1996) is the Mellor-Yamada scheme (Mellor and Yamada, 1974; Cheng *et al.*, 2002). This scheme uses the down-gradient approach to parameterise subgrid-scale turbulent fluxes of momentum, heat and humidity based on the approximation of the eddy diffusivity coefficients for momentum and scalars. However, this approximation requires a formulation of the turbulent mixing length to relate the eddy diffusivity coefficient to the turbulent kinetic energy (TKE) of the flow (Durand *et al.*, 2000). The master length scale approach (Mellor and Yamada, 1974; Cheng *et al.*, 2002) is used in the Mellor-Yamada scheme as formulation for the turbulent mixing length. This approach is based on a characteristic length scale l , representative of the neutral stability state (Blackadar, 1962). All other characteristic model length scales are then assumed to be proportional to l .

Atmospheric measurements (Gossard, 1960; Busch and Larsen, 1972) and theoretical considerations (Dubrulle and Niino, 1992) indicated a pronounced dependence of characteristic length scales on atmospheric stability. Thus, to take into account deviations of atmospheric stability from the neutral state, formulations of turbulent mixing length based on the master length scale require additional dimensionless stability functions (Mellor and Yamada, 1974, 1982; Yamada, 1983; André *et al.*, 1978; Arritt, 1987; Duynkerke and Driedonks, 1987). However, these stability functions take not into account effects of varying vertical stratification throughout the whole depth of the PBL due to their dependence on local Richardson numbers (Bélair *et al.*, 1999). This is primarily a problem within the entrainment zone at the upper CBL, where strong changes in vertical stratification occur. However, these uncertainties of turbulent mixing lengths are critical for the simulation of cloud development, since a correct parameterisation of turbulent mixing is essential for obtaining proper entrainment fluxes at the CBL top (Abdalla and McFarlane, 1997; Cuijpers and Holtslag, 1998). Thus, uncertainties in turbulent mixing lengths can result in systematic shortcomings in numerical simulations of convective boundary layer processes (Bélair *et al.*, 1999). Therefore, the determination of stability dependent characteristic length scales even

for the CBL is of great importance and a challenging problem in turbulence parameterisations.

Characteristic turbulence length scales are related to the energy spectrum of turbulent fluctuations (Kaiser and Fedorovich, 1998). Therefore, they show an inherent dependence on atmospheric stability. Accordingly, attempts have been made to use these scales in formulations of turbulent mixing length (Sun and Chang, 1986; Degrazia *et al.*, 1997). However, this approach requires a database of characteristic turbulence length scales, representing a wide range of atmospheric stability states.

Atmospheric measurements (Kaimal *et al.*, 1972, 1976; Caughey and Palmer, 1979; Lenschow and Stankov, 1986; Durand *et al.*, 2000) and laboratory experiments (Willis and Deardorff, 1974; Kaiser and Fedorovich, 1998; Ahlers, 2001; Grossmann and Lohse, 2001) have provided valuable contributions in examinations of turbulent processes in CBLs. However, characteristic turbulence length scales, derived from measurements are often based on turbulence data, obtained only in a small parameter space of CBL stability states.

Therefore, large-eddy simulation (LES) of CBLs has been increasingly used in the last years to augment the database of turbulence data (Ayotte *et al.*, 1996). Based on the pioneering work of Deardorff (1970b) LES resolves explicitly the turbulent eddies and parameterise only the less energy-containing and more isotropic small-scale motions in a subgrid-scale model. Thus, LES covers a wide range of CBL stability states and provides three-dimensional fields of wind velocity, temperature, and moisture in high resolution. Furthermore, since only a small portion of the turbulence has to be considered by the subgrid-scale model, LES results are much less sensitive to turbulence parameterisation assumptions. Thus, development and evaluation of parameterisation schemes for climate- and weather prediction models is increasingly based on large-eddy simulation (Siebesma and Cuijpers, 1995; Ayotte *et al.*, 1996; Brown and Grant, 1997; Kershaw and Gregory, 1997; Nakanishi, 2001).

Although the use of subgrid-scale models for motions below the filter width of LES could lead to some uncertainties in small-scale mixing (Moeng *et al.*, 1996), the simulation results in bulk of the CBL were shown to be insensitive to the treatment of SGS motions and numerical methods (Nieuwstadt *et al.*, 1993; Andr n *et al.*, 1994)

First meteorological applications of LES concerned the convective boundary layer (Deardorff, 1973, 1974; Moeng and Wyngaard, 1986; Schumann *et al.*, 1987; Mason, 1989; Schmidt and Schumann, 1989) providing significant contributions in understanding of turbulent transports of momentum, heat and moisture by coherent buoyant thermals. However, LES is not restricted to pure convective boundary layers. Several large-eddy simulations of the shear-driven boundary layer (Moeng and Sullivan, 1994; Lin *et al.*, 1996; Khanna and Brasseur, 1998; Lohou *et al.*, 2000) found an elongation of turbulent eddies in mean wind direction that could explain observed roll structures in real shear-driven PBLs. Furthermore, based on LES of clear CBLs, various studies provided valuable insights into the behaviour of characteristic turbulence length scales (Mason, 1989; Khanna and Brasseur, 1998; Nakanishi, 2001).

This thesis focuses on the determination of characteristic turbulence length scales from a comprehensive database of artificial three-dimensional CBLs. Based on a LES model (Chlond, 1992, 1999) that considers the water cycle including cloud formation, the aim is to extent previous LES studies by taking into account moisture-containing CBLs. Thus, the LES database includes clear and moisture-containing CBLs of varying atmospheric stability, driven by buoy-

ancy and shear. The high resolution of the simulated CBLs allows to derive the characteristic turbulence length scales over a wide range of stability states. The aim is to use these length scales to develop an adequate stability dependent turbulent mixing length formulation.

The implications of this new mixing length formulation on evolution of the dynamic and thermodynamic state of the atmosphere at regional scale will be investigated. Thus, based on the non-hydrostatic limited area model ("Lokal-Modell"- LM), the simulation of 24 hrs of the most intensive measurement campaign during the LITFASS-98 field experiment (Beyrich, 2001) will be performed. For a comprehensive verification of the simulation results, satellite based observations and a model analysis data resulting from 4D assimilation (Schraff and Hess, 2002; Wergen, 2002) will be used. Accordingly, the interactions between turbulent processes, influenced by the formulation of the turbulent mixing length and processes occurring at regional scale will be examined.

To address the above-mentioned issues, the thesis has been divided into the following chapters: The methods commonly used to consider turbulent processes in atmospheric models of different scale of interest are illustrated in Chapter 2. Furthermore, this Chapter focuses on main properties of the Mellor-Yamada model and formulations of turbulent mixing commonly used in NWP models. Further characteristic scales of turbulent processes are derived by examination of the spectrum of the turbulent kinetic energy. In Chapter 3, the generation of the LES database of artificial CBLs, the determination of turbulent mixing length scales, and the verification of the results will be presented. The verification is based on numerical simulations, atmospheric measurements and laboratory experiments. Furthermore, this Chapter contains the development and verification of a new turbulent mixing length formulation based on LES database results. In Chapter 4, the implications of this turbulent mixing length on results of a model simulation at regional scale is examined. This simulation is based on the LM and considers 24 hrs of the LITFASS measurement campaign. Conclusions and further directions of this thesis are given in Chapter 5.

Treatment of turbulent processes in atmospheric models

The fundamental principles, which constitute the base of atmospheric models considered here are balance equations for momentum, heat, moisture, and mass. These principles lead to a set of governing equations for the flow variables wind velocity, active scalars¹, and passive scalars² in terms of coupled partial differential equations in several dimensions. This set of governing equations has to be solved simultaneously in discrete form by the numerical model (Holton, 1972; Stull, 1997; Beniston, 1998).

To perform representative atmospheric simulations, numerical models based on these governing equations should address as many as possible of physical factors linked to the dynamic and thermodynamic characteristics of the atmosphere. However, as shown in Fig. 2.1 atmospheric processes cover a wide range of spatial and temporal scales. Therefore, these processes are characterised by very large Reynolds numbers Re in the order of $Re \sim 10^{14}$. Although the fundamental equations are the same for all models and independent of scale, the scale of interest strongly determines the type of model simplifications and required physical parameterisation of non-resolved processes. As a result, illustrated in Fig. 2.1, there is no single model that takes into account all these scales explicitly, but a spectrum of atmospheric models with different scale of interest.

The wide spectrum of models is related to the wide range of scales of atmospheric processes reaching from Kolmogorov length scale η (Kolmogorov, 1941), which is in the order of 10^{-3} m, to scales of the specific model-domain size L_D (Reynolds, 1990), which is in the order of 10^5 - 10^8 m for general circulation models (GCM).

It is shown in Fig. 2.1 that models, which resolve all scales by the direct numerical simulation (DNS), are restricted to microscale. Here, the scale of interest is in the order of 10^1 m. However, resolving turbulent eddies in the CBL with characteristic length scales up to 10^3 m and Reynolds numbers of $Re = 10^{10}$ based on DNS would require $N_D \sim 10^7$ gridpoints in one direction ($N_D \sim \eta/L_D \sim Re^{-3/4}$). However, these requirements exceeds the computational power of present-days and also near future supercomputers.

The high computational costs of DNS have motivated a number of different approaches to simulate atmospheric flows with high Reynolds numbers using a given number of modes in

¹Active scalars (e.g., temperature, moisture) have impact on the air density and influence therefore the dynamics of the flow

²Passive scalars (e.g., aerosols) are transferred with the flow, but have no impact on the dynamics of the flow

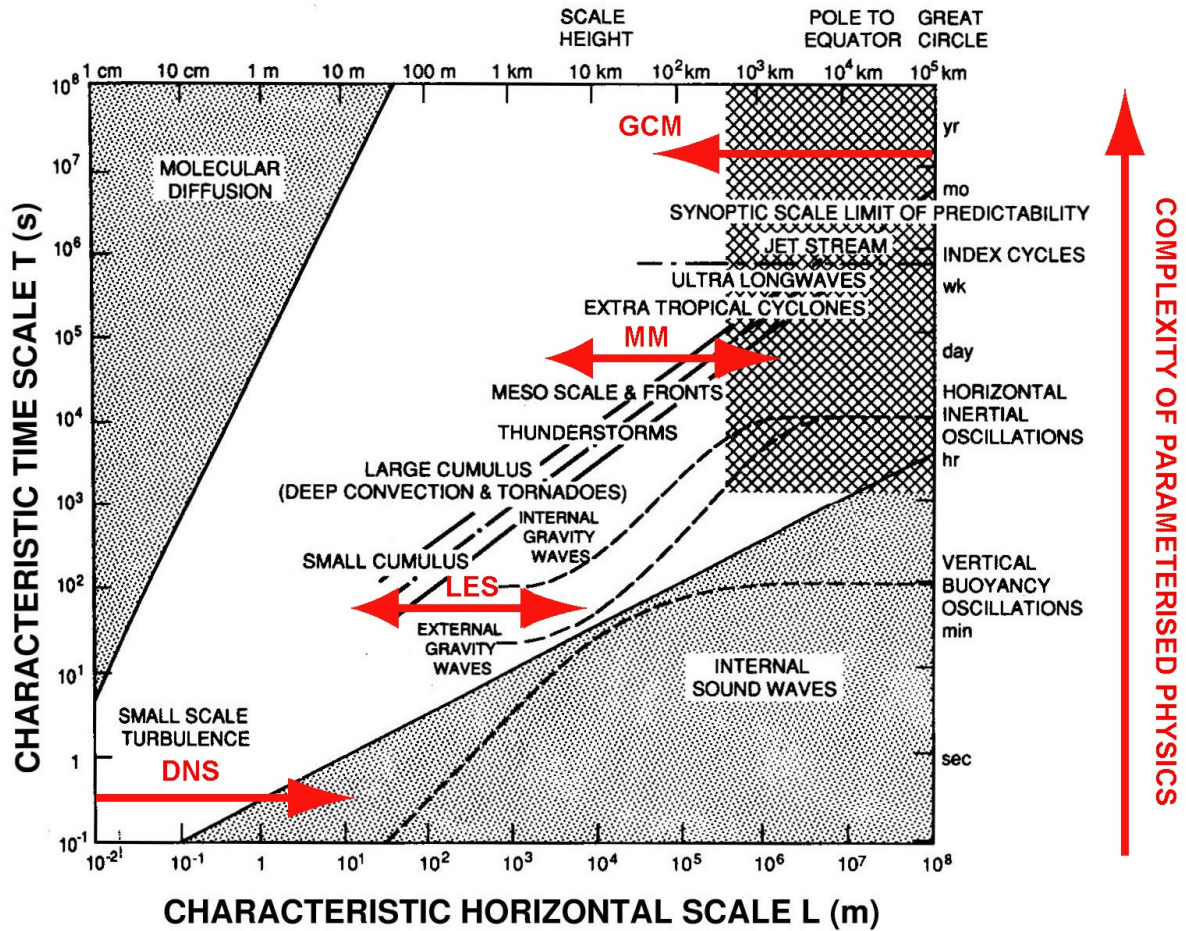


FIGURE 2.1: Characteristic spatial and temporal scales of atmospheric processes and corresponding atmospheric models with varying scale of interest (after Galperin and Orszag (1993) and Stevens and Lenschow (2001)). The acronyms, used in the figure are DNS (direct numerical simulation), LES (large-eddy simulation), MM (mesoscale model) and GCM (general circulation model).

wavenumber space. They are based on incompletely resolving either the low-wavenumber or the high-wavenumber modes (Pope, 2000). One of the most popular approaches for simulations of boundary layer processes with horizontal scales up to about 10^4 m is large-eddy simulation.

In contrast to DNS, where the majority of modes is used to resolve the isotropic, less energy-containing turbulent eddies in the high-wavenumber dissipative range, LES derives benefit from the power law behaviour of the energy spectrum of turbulent motions. It explicitly resolves turbulent eddies in the low-wavenumber range. In the dissipative range, LES reduces the resolution requirements by subgrid-scale modelling of the residual unresolved structures (Galperin and Orszag, 1993; Métais and Ferziger, 1997; Pope, 2000). Thus, LES acts as low-pass filter for the set of governing equations.

The complexity of parameterisations of non-resolved processes increases as the scale of interest of the atmospheric model increases (Fig. 2.1). As a result, models at regional and global scale have to parameterise an increased number of atmospheric processes compared to LES. Therefore, the scale separation approach of flow variables is used in these models to simulate atmospheric flows at regional and global scale. The scale separation approach is based on the assumption that the average of any flow variable at large scale of interest varies much more slowly in time and space than its deviation from average. Thus, the scale separation for velocity components $u_i = (u, v, w)$ and scalars ϕ yields

$$u_i = \bar{u}_i + u'_i, \quad (2.1)$$

$$\phi = \bar{\phi} + \phi', \quad (2.2)$$

where the wind velocity components \bar{u}_i and the scalar variables $\bar{\phi}$ are related to model scale of interest, whereas u'_i and ϕ' are related to the subgrid-scale fluctuations.

Application of scale separation and averaging leads to the so-called Reynolds-averaged governing equations. They contain additional terms related to covariances of the subgrid-scale fluctuations of flow variables u_i and ϕ . Their characteristics and predictability is subject to “turbulence theory” (Batchelor, 1953; Panchev, 1971; Monin and Yaglom, 1975; Lesieur, 1990; McComb, 1990; Frisch, 1995; Pope, 2000).

The non-resolved subgrid-scale terms of u_i can be interpreted as turbulence induced stresses. They are described in terms of the residual stress tensor τ_{ij} given as

$$\tau_{ij} = \overline{u_i u_j} - \bar{u}_i \bar{u}_j, \quad (2.3)$$

where the half trace of τ_{ij} is related to the residual kinetic energy of the non-resolved part of the flow.

$$\bar{e} = \frac{1}{2} \tau_{ii}. \quad (2.4)$$

The decomposition (Eq. (2.1)) allows to write the residual stress tensor as superposition of three different stress tensors (Leonard, 1974)

$$\tau_{ij} = \mathcal{L}_{ij} + \mathcal{C}_{ij} + \mathcal{R}_{ij}, \quad (2.5)$$

where $\mathcal{L}_{ij} = \overline{\bar{u}_i \bar{u}_j} - \bar{u}_i \bar{u}_j$ are Leonard stresses, $\mathcal{C}_{ij} = \overline{\bar{u}_i u'_j} + \overline{u'_i \bar{u}_j}$ are cross stresses, and $\mathcal{R}_{ij} = \overline{u'_i u'_j}$ are Reynolds stresses.

The assumption of $\bar{\bar{u}}_i = \bar{u}_i$ in models at regional and global scale leads to vanishing Leonard and cross stresses. In this case, the residual stress tensor is determined by the Reynolds stress tensor \mathcal{R}_{ij} . However, $\bar{\bar{u}}_i = \bar{u}_i$ is not generally valid in LES resulting in non-vanishing Leonard and cross stresses. However, \mathcal{L}_{ij} and \mathcal{C}_{ij} are considered as small compared to \mathcal{R}_{ij} (Chlond, 1999).

Thus, the Reynolds stress tensor is the most important stress tensor in atmospheric models to describe the influence of non-resolved atmospheric processes on the dynamic and thermodynamic state of the atmosphere. In mathematical sense, \mathcal{R}_{ij} corresponds to a symmetric positive semi-definite tensor. Its diagonal components $\overline{u_i'^2}$ are called normal stresses, whereas its off-diagonal components $\overline{u_i' u_j'}$ are called shear stresses.

2.1 Turbulence parameterisation approaches

The development of approximations for the components of the Reynolds stress tensor leads to the turbulence closure problem (Keller and Friedman, 1924). It arises, if prognostic or diagnostic equations for statistical moments of Reynolds stress tensor components are considered. These equations always include statistical moments of higher order. Thus, for a finite set of equations, the statistical description of the Reynolds stress tensor is not closed.

To get a tractable statistical description of the Reynolds stress tensor components, only a finite number of equations is used, whereas the remaining unknown higher order moments are approximated by known statistical moments of lower order. This approach is often applied in atmospheric models. It is called turbulence closure approximation (Stull, 1997) and named by the highest order of prognostic equations for the statistical moments that are retained.

Two major turbulence closure approximations have appeared in the literature. These are local closure (Sec. 2.1.1) and non-local closure (Sec. 2.1.2). The decision for one type of closure approximation and the level of sophistication depends on model scale of interest, available computational power and complexity of processes under consideration (Holt and Raman, 1988; Stull, 1997).

2.1.1 Local closure approximation

In local closure approximation the components of \mathcal{R}_{ij} related to turbulent fluxes of momentum, heat and humidity at a certain location in the atmosphere are determined from averaged flow variables and their gradients at that location. Thus, local closure of a turbulent flux $\overline{u'_k \chi'}$ of any flow variable χ is based on the small eddy approach that is

$$\overline{u'_k \chi'} = -K_\chi \frac{\partial \bar{\chi}}{\partial x_k}, \quad (2.6)$$

where $\partial \bar{\chi} / \partial x_k$ is the local gradient of $\bar{\chi}$ and K_χ is the eddy diffusivity coefficient of the flow variable χ . In close analogy to molecular viscosity, K_χ describes transport related to turbulent diffusion. This analogy requires positive values for the eddy diffusivity coefficient leading to a down-gradient turbulent transport. Consequently, local closure approximation schemes based on the small eddy approach are often called down-gradient schemes.

In dependence on the model scale of interest (see Fig. 2.1), local closure approximations used in atmospheric models take into account statistical moments of turbulent variables up to the

- order 1 considering prognostic equations for means (e.g., O'Brien (1970); Pielke and Mahrer (1975), and Louis (1979)),
- order 2 considering prognostic equations for means and variances (e.g., Mellor and Yamada (1974) and Abdalla and McFarlane (1997)),
- order 3 considering prognostic equations for means, variances, and third-order moments (e.g., André *et al.* (1978); Moeng and Randall (1984), and Zilitinkevich *et al.* (1999)).

Due to improvements of turbulence measurements (Druihet and Durand, 1997) as well as of computational capabilities (Bonnert, 2003), in last years the development of local closure schemes primarily has focused on higher-order (order 2-3) schemes. However, the numerical requirements of these schemes are still too expensive for application of these schemes in atmospheric models with regional and global scale of interest.

Independent on their order, local closure schemes have been successfully applied in modelling of the evolution of daytime and nocturnal boundary layers (Bélair *et al.*, 1999). However, their local structure lead to difficulties in simulating convective boundary layers (Deardorff, 1972; Ebert *et al.*, 1989; Holtslag and Moeng, 1991; Chrobok *et al.*, 1992). These problems are related to a vanishing of the mean gradients of flow variables in well mixed CBLs (Holtslag and Moeng, 1991). According to Eq. (2.6) this would lead to a vanishing turbulent flux, which is in contrast to observations. Consequently, turbulent transports in CBLs are dominated by turbulent eddies that are not captured in local closure approximations.

2.1.2 Non-local closure approximation

Non-local closure approximations were developed for two decades to take into account the turbulent mixing due to turbulent eddies. They are based on the assumption that the components of \mathcal{R}_{ij} at a certain location in the atmosphere are determined by flow variables at scale of interest from many locations within the CBL.

Some of the approximations that have been appeared in literature are:

- Turbulent transilient theory (Stull, 1984, 1993; Stull and Driedonks, 1987)
- Top-down bottom-up diffusion (e.g., Wyngaard and Brost (1984))
- Spectral diffusivity theory (Berkowicz, 1984)
- Integral turbulence closure (Fiedler and Moeng, 1985).

However, non-local closure approximations show an increased complexity compared to local closure approximations. Therefore, the inclusion of non-local closure approximation into atmospheric models leads to a considerable increase in computing time (Bélair *et al.*, 1999). This limits the application of non-local schemes in atmospheric models with regional and global scale of interest.

2.1.3 Counter-gradient approximation

The counter-gradient approximation, originated with Deardorff (1972) is considered as a trade-off between computational costs and simulation accuracy for convective boundary layers. This approach includes non-local effects in a simpler manner. It uses counter-gradient non-local terms in Eq. (2.6) only for vertical turbulent fluxes of scalars $\overline{w'\phi'}$ (e.g., turbulent sensible heat flux $\overline{w'\theta'}$, turbulent flux of total water content $\overline{w'q'}$) (Mailhot and Benoit, 1982; Therry and Lacarrère,

1983; Troen and Mahrt, 1986; Holtslag and Moeng, 1991; Cuijpers and Holtslag, 1998). This yields

$$\overline{w'\phi'} = -K_\phi \left(\frac{\partial \overline{\phi}}{\partial z} - \gamma_\phi \right), \quad (2.7)$$

where γ_ϕ is an “equilibrium scalar gradient”, incorporated as “counter-gradient”.

Compared to the down-gradient approach, the counter-gradient approximation leads to improved parameterisations of CBL properties (Holtslag and Boville, 1993; Holtslag *et al.*, 1995; Lüpkes and Schlünzen, 1996) since γ_ϕ leads to non-vanishing turbulent fluxes in well mixed conditions ($\partial \overline{\phi} / \partial z \rightarrow 0$). However, the required parameterisation of γ_ϕ , often based on approximations of second order moments increase the computational costs.

2.2 Local closure approximation after Mellor-Yamada

The great importance of computational costs for models with regional and global scale of interest (e.g., mesoscale models and general circulation models), especially for operational weather forecast applications, limits the use of complex non-local closure and counter-gradient approximations in these model applications. Consequently, many models with regional and global scale of interest currently use local closure approximation of order 1 after Louis (1979) or of order 1 1/2 after Mellor and Yamada (1974, 1982) (Ayotte *et al.*, 1996).

Primarily the local closure approximation of order 1 1/2 after Mellor and Yamada (1974, 1982), thereafter referred as MY-model, has become increasingly popular during the last 10 years (Janjić, 2001; Cheng *et al.*, 2002). In replacing prognostic velocity variance equations by a prognostic equation for TKE, it simplifies the local closure approximation of order 2. As a result, this approach associates the accuracy of higher-order closures with efficient computational algorithms of lower-order closures (Janjić, 2001). In the model suite of Mellor and Yamada (1982) including four models of different degree of sophistication this local closure of order 1 1/2 was incorporated as Level 2.5 (MY25). The parameterisation of eddy diffusivity coefficients in MY25 use a master length scale l to relate the eddy diffusivity to the TKE. However, the master length scale approach is considered to be one of the major weaknesses of the MY-model (Mellor and Yamada, 1982; Cheng *et al.*, 2002). Although efforts have been made to evaluate l by a prognostic equation (Mellor and Yamada, 1982), it is very time consuming and uncertain due to the required specification of empirical turbulence parameters. Thus, it is one aim of this work to examine the impact of a new formulation for l on results of the MY-model.

The eddy diffusivity coefficients are given in MY25 as

$$K_M = S_M l E, \quad (2.8)$$

$$K_\phi = S_\phi l E, \quad (2.9)$$

where K_M is the eddy diffusivity coefficients for momentum, K_ϕ is the eddy diffusivity coefficients for scalars³, l is the master length scale, and S_M , S_ϕ are dimensionless stability functions

³Potential temperature θ is used as scalar variable in dry atmosphere, virtual potential temperature θ_v is used as

for momentum and scalars, respectively. Here,

$$\frac{1}{2}E^2 = \frac{1}{2}\overline{u}_i^2 \quad (2.10)$$

is the model TKE.

Based on a set of constants

$$(A_1, B_1, A_2, B_2, C_1) = (0.92, 16.6, 0.74, 10.1, 0.08), \quad (2.11)$$

derived from several atmospheric measurements by Mellor and Yamada (1982), S_M and S_ϕ can be determined in terms of diagnostic equations as

$$S_M = \frac{A_2 F_2 - R_1 F_4}{F_2 F_3 - F_1 F_4}, \quad (2.12)$$

$$S_\phi = \frac{R_1 F_3 - A_2 F_1}{F_2 F_3 - F_1 F_4} \quad (2.13)$$

using the parameters F_1, F_2, F_3, F_4, R_1 (Nakanishi, 2001), given as

$$F_1 = 1 + 6A_1^2 G_M - 9A_1 A_2 G_\phi, \quad (2.14)$$

$$F_2 = -3A_1(4A_1 + 3A_2)G_\phi, \quad (2.15)$$

$$F_3 = 6A_1 A_2 G_M, \quad (2.16)$$

$$F_4 = 1 - (12A_1 A_2 + 3A_2 B_2)G_\phi, \quad (2.17)$$

$$R_1 = A_1(1 - 3C_1). \quad (2.18)$$

Since G_M and G_ϕ are defined as

$$G_M = \frac{l^2}{E} \left\{ \left(\frac{\partial \overline{u}}{\partial z} \right)^2 + \left(\frac{\partial \overline{v}}{\partial z} \right)^2 \right\} \quad (2.19)$$

$$G_\phi = -\frac{l^2}{E} \frac{g}{\overline{\theta}} \frac{\partial \overline{\theta}}{\partial z}, \quad (2.20)$$

the dimensionless stability functions S_M and S_ϕ are functions of the local gradient Richardson number, given as

$$\text{Ri} = \frac{g}{\overline{\theta}} \frac{\frac{\partial \overline{\theta}}{\partial z}}{\left(\frac{\partial \overline{u}}{\partial z} \right)^2 + \left(\frac{\partial \overline{v}}{\partial z} \right)^2} = -\frac{G_\phi}{G_M}. \quad (2.21)$$

The ‘‘ordering of terms’’-approach (Mellor and Yamada, 1974) accompanied by the boundary layer approximation, yields a prognostic equation of the residual kinetic energy, which is given as

$$\frac{\partial}{\partial t} \frac{E^2}{2} + \overline{u}_k \frac{\partial}{\partial x_k} \left(\frac{E^2}{2} \right) - \frac{\partial}{\partial z} \left\{ S_E l E \frac{\partial}{\partial dz} \left(\frac{E^2}{2} \right) \right\} = P_s + P_b - \varepsilon_m, \quad (2.22)$$

scalar variable in moisture-containing atmosphere, liquid water potential temperature θ_l and total water content q are used as conserved scalar variables in moisture-containing atmosphere, when phase changes occur.

where S_E is a stability function, P_s is the shear production of TKE, P_b is the buoyant production of TKE, and ϵ_m is the model dissipation rate, given as

$$P_s = -\overline{w'u'} \frac{\partial \bar{u}}{\partial z} - \overline{w'v'} \frac{\partial \bar{v}}{\partial z}, \quad (2.23)$$

$$P_b = \frac{g}{\theta} \overline{w'\theta'}, \quad \text{and} \quad (2.24)$$

$$\epsilon_m = \frac{E^3}{\Lambda_1}, \quad (2.25)$$

where u, v, w are zonal, meridional, and vertical velocity components, g is the earth acceleration, and Λ_1 is a characteristic length scale of the MY-model.

According to the down-gradient approach used in MY25, the turbulent fluxes of momentum and scalars are parameterised as

$$\overline{u'w'} = -S_M l E \frac{\partial \bar{u}}{\partial z} = -K_M \frac{\partial \bar{u}}{\partial z}, \quad (2.26)$$

$$\overline{v'w'} = -S_M l E \frac{\partial \bar{v}}{\partial z} = -K_M \frac{\partial \bar{v}}{\partial z}, \quad (2.27)$$

$$\overline{w'\phi'} = -S_\phi l E \frac{\partial \bar{\phi}}{\partial z} = -K_\phi \frac{\partial \bar{\phi}}{\partial z}. \quad (2.28)$$

Since MY25 is a local closure scheme of order $1\ 1/2$, diagnostic equations are used to determine the variances of the wind velocity components and of scalars. They are given as

$$\overline{u'^2} = \frac{E^2}{3} + \frac{l_1}{E} \left(-4\overline{u'w'} \frac{\partial \bar{u}}{\partial z} + 2\overline{v'w'} \frac{\partial \bar{v}}{\partial z} - 2P_b \right), \quad (2.29)$$

$$\overline{v'^2} = \frac{E^2}{3} + \frac{l_1}{E} \left(2\overline{u'w'} \frac{\partial \bar{u}}{\partial z} - 4\overline{v'w'} \frac{\partial \bar{v}}{\partial z} - 2P_b \right), \quad (2.30)$$

$$\overline{w'^2} = \frac{E^2}{3} + \frac{l_1}{E} \left(2\overline{u'w'} \frac{\partial \bar{u}}{\partial z} + 2\overline{v'w'} \frac{\partial \bar{v}}{\partial z} + 4P_b \right), \quad (2.31)$$

$$\overline{\phi'^2} = -\frac{\Lambda_2}{q} \overline{w'\phi'} \frac{\partial \bar{\phi}}{\partial z}. \quad (2.32)$$

Obviously, the approximation of the turbulent fluxes and variances in MY25 (Eqs. (2.26)-(2.32)) is influenced by various characteristic model length scales l, l_1 , and Λ_2 . Thus, a turbulent mixing length formulation is required to provide approximations for these length scales.

2.3 Turbulent mixing length formulations

The turbulent mixing length formulation of the MY-model used the master length scale approach (Mellor and Yamada, 1974, 1982). Based on the length scale l , used in Eqs. (2.8)-(2.9), all

characteristic model length scales $(l_1, \Lambda_1, l_2, \Lambda_2)$ are assumed to be everywhere proportional to l as

$$(l_1, \Lambda_1, l_2, \Lambda_2) = (A_1, B_1, A_2, B_2)l, \quad (2.33)$$

where the constants (A_1, B_1, A_2, B_2) refer to Eq. (2.11).

A length scale, proposed by Blackadar (1962) for neutral stability is often used as master length scale (Mellor and Yamada, 1974, 1982). In this formulation l is defined as

$$l = \left(\frac{1}{\kappa z} + \frac{1}{l_0} \right)^{-1}, \quad (2.34)$$

where κ is the von-Karman constant. The asymptotic length scale for $z \rightarrow \infty$ is given by l_0 . Various approximations exist for l_0 (Blackadar, 1962; Mellor and Yamada, 1974; Arritt, 1987; Holtslag and Boville, 1993; Doms and Schättler, 1999). Most of them assume l_0 in the order of 300-500 m.

However, the turbulent mixing length formulation based on the master length scale requires additional assumptions for deviations from neutral stability state, provided by the dimensionless stability functions S_M, S_ϕ . Although attempts have been made to consider deviations from neutral stability state within the diagnostic length scale equation (Arritt, 1987) by

$$l = S_M^{1/2} \left(\frac{1}{\kappa z} + \frac{1}{l_0} \right)^{-1}, \quad (2.35)$$

similar to Eq. (2.34), this formulation requires also the approximation of an additional stability function S_M . Furthermore, using this length scale equation in Eqs. (2.8)-(2.9) leads to a double-counting of stability.

A further formulation of mixing lengths based on several characteristic length scales L_1, L_2 is the stability-dependent dual-choice length scale approach (André *et al.*, 1978; Duynkerke and Driedonks, 1987) given as

$$l = \min(L_1, L_2), \quad (2.36)$$

where

$$L_1 = \left(\frac{\Phi_M}{\kappa z} + \frac{1}{l_0} \right)^{-1}, \quad \text{and} \quad (2.37)$$

$$L_2 = 0.36\bar{e}^{1/2} \left(\frac{g}{\bar{\theta}} \frac{\partial \bar{\theta}}{\partial z} \right)^{-1/2}, \quad \text{for} \quad \frac{\partial \bar{\theta}}{\partial z} \geq 0. \quad (2.38)$$

However, similar to the previous formulation of turbulent mixing length, the dual-choice length scale approach depends on an additional stability function Φ_M . Since dimensionless stability functions S_M, S_ϕ , and Φ_M are based on local Richardson numbers (Eq. (2.21)), they cannot account for the effect of varying vertical stratification throughout the whole depth of the PBL (Bélair *et al.*, 1999). This is primarily a problem within the entrainment zone at the upper CBL, where strong changes in vertical stratification occur.

An alternative dual-choice length scale approach (Bougeault and Lacarrère, 1989; Bélair *et al.*, 1999) is based on potential upward and downward displacements of upward and downward

moving parcels. Here, the stability state is taken into account by the displacements (l_{up} and l_{down}). These displacements can be achieved by parcels with kinetic energy equal to the mean TKE at the level, where they started before they are stopped by buoyancy effects (Bélair *et al.*, 1999). In this formulation, l_{up} and l_{down} are given as

$$e(z) = \int_z^{z+l_{\text{up}}} \frac{g}{\theta_{v,s}} \{ \theta(z') - \theta(z) \} dz' \quad (2.39)$$

$$e(z) = \int_{z-l_{\text{down}}}^z \frac{g}{\theta_{v,s}} \{ \theta(z) - \theta(z') \} dz', \quad \text{and} \quad l_{\text{down}} < z, \quad (2.40)$$

where z is the height of the initial level, $e(z)$ is the local TKE, and $\theta_{v,s}$ is the virtual potential temperature of near surface air. The turbulent mixing length scale ℓ_k , related to the most energy-containing turbulent structures and dissipation length scale ℓ_ε , responsible for dissipative structures are determined from l_{up} and l_{down} as

$$\ell_k = \min(l_{\text{up}}, l_{\text{down}}), \quad (2.41)$$

and

$$\ell_\varepsilon = (l_{\text{up}} \cdot l_{\text{down}})^{1/2}. \quad (2.42)$$

However, the required averaging of l_{up} and l_{down} is considered as a difficult aspect of this method (Bélair *et al.*, 1999).

2.4 Characteristic turbulence length scales

An alternative approach, used in this work is based on the examination of characteristic turbulence length scales. These length scales are related to the scale-dependent distribution of turbulent kinetic energy of turbulent eddies. Turbulent motions in terms of turbulent eddies refer to vortices, where an eddy is considered as localised within a region of size ℓ (Pope, 2000). In general, the region occupied by a large eddy can also contain smaller eddies.

According to Richardson (1922) turbulent flows with large Reynolds numbers contain eddies of different sizes. The eddies representative of the largest size range ℓ_0 are characterised by the turbulence length scale, which is comparable to the length scale L of the flow. In this range they are anisotropic and affected by the boundary conditions of the flow (Pope, 2000). This size range is called energy-containing range, because it contains the bulk of the turbulent energy due to buoyancy and shear (Kaimal and Finnigan, 1994).

The instability of the large eddies leads to a transfer of their energy to eddies of smaller length scale $\ell < \ell_0$. This process is repeated to smaller and smaller scales in the inertial subrange. During this conversion process, TKE is neither produced nor dissipated but handed down to smaller scales, whereas all information about the geometry of the large eddies is lost. Thus, the statistics of the small-scale motions, which contain less TKE is universal for every high-Reynolds number turbulent flows (First Similarity-Hypothesis of Kolmogorov (1941)) and is

uniquely determined by dissipation ε but independent of fluid viscosity ν (Second Similarity-Hypothesis of Kolmogorov (1941)).

This is an important finding for the parameterisation of sub-filter scale processes in LES models, where the universal properties of the less energy-containing eddies allows the application of simple turbulence closure approximations. The characteristic turbulence length scale, representative of eddies in the inertial subrange is the dissipation length scale ℓ_ε (Durand *et al.*, 2000).

If the eddies are small enough that eddy Reynolds number $\text{Re}(\ell) = 1$, their kinetic energy dissipates in internal energy (heat) due to molecular viscosity. At this point, the eddies enter the dissipation range. The characteristic turbulence length scale of the dissipation range is the Kolmogorov length scale η depending on dissipation ε and viscosity ν by $\eta = (\nu^3/\varepsilon)^{1/4}$.

Information about the spatial structure of the turbulent field, required to derive characteristic length scales is provided by several statistical parameters.

The covariance between two flow variables χ_i and χ_j is given as

$$R_{\chi_i\chi_j}(\mathbf{r}) = \int_{-\infty}^{\infty} \chi_i(\mathbf{x})\chi_j(\mathbf{x} + \mathbf{r})d\mathbf{x}, \quad (2.43)$$

where \mathbf{x} is the position vector and \mathbf{r} is the displacement vector. The auto-covariance yields, if χ_i and χ_j are identical ($i = j$)

$$R_{\chi_i\chi_i}(\mathbf{r}) = \int_{-\infty}^{\infty} \chi_i(\mathbf{x})\chi_i(\mathbf{x} + \mathbf{r})d\mathbf{x}. \quad (2.44)$$

The spatial structure in wavenumber space of a flow variable χ_i is given by the Fourier transform

$$\Phi_{\chi_i}(\mathbf{k}) = \frac{1}{(2\pi)^3} \int_{-\infty}^{\infty} e^{-i\mathbf{k}\cdot\mathbf{r}} \chi_i(\mathbf{r})d\mathbf{r}, \quad (2.45)$$

where $\Phi_{\chi_i}(\mathbf{k})$ is the spectrum of χ_i and \mathbf{k} is the wavenumber vector.

Based on the Correlation Theorem and the Wiener-Khinchin Theorem (Press *et al.*, 1996), the Fourier transform can be used to determine $R_{\chi_i\chi_j}(\mathbf{r})$ and $R_{\chi_i\chi_i}(\mathbf{r})$ by

$$R_{\chi_i\chi_j}(\mathbf{r}) = \int_{-\infty}^{\infty} e^{-i\mathbf{k}\cdot\mathbf{r}} \left\{ \Phi_{\chi_i}(\mathbf{k})\Phi_{\chi_j}^*(\mathbf{k}) \right\} d\mathbf{k}, \quad (2.46)$$

$$R_{\chi_i\chi_i}(\mathbf{r}) = \int_{-\infty}^{\infty} e^{-i\mathbf{k}\cdot\mathbf{r}} \left\{ \left| \Phi_{\chi_i}(\mathbf{k}) \right|^2 \right\} d\mathbf{k}, \quad (2.47)$$

where $\Phi_{\chi_j}^*(\mathbf{k})$ is the complex conjugate of $\Phi_{\chi_j}(\mathbf{k})$.

Using Eq. (2.46) with $\chi_i = u_i$, $\chi_j = u_j$, and $\mathbf{r} = 0$ yields the velocity covariances $\overline{u'_i u'_j}$ of the Reynolds stress tensor \mathcal{R}_{ij} by

$$R_{u_i u_j}(0) = \overline{u'_i u'_j} = \int_{-\infty}^{\infty} \Phi_{u_i}(\mathbf{k}) \Phi_{u_j}^*(\mathbf{k}) d\mathbf{k}, \quad (2.48)$$

where $\Phi_{u_i}(\mathbf{k}) \Phi_{u_j}^*(\mathbf{k})$ represents the contribution of velocity modes with wavenumber \mathbf{k} to the covariance $\overline{u'_i u'_j}$ and, therefore, the contribution to the Reynolds-stress density in wavenumber space.

Integration of the half of the trace of $\Phi_{\chi_i}(\mathbf{k}) \Phi_{\chi_j}^*(\mathbf{k})$ yields the energy spectrum E_χ of the flow variable χ

$$E_\chi(k) = \int_{-\infty}^{\infty} \frac{1}{2} \left\{ \Phi_{\chi_i}(\mathbf{k}) \Phi_{\chi_i}^*(\mathbf{k}) \right\} \delta(|\mathbf{k}| - k) d\mathbf{k}, \quad (2.49)$$

that is the turbulent energy of the eddies depending on their wavenumber. Integration of $E_\chi(k)$ over all $k = |\mathbf{k}|$ yields an expression for the turbulent energy of the flow, given as

$$e_\chi = \frac{1}{2} \overline{\chi_i \chi_i} = \frac{1}{2} R_{\chi_i \chi_i}(0) = \int_0^{\infty} E_\chi(k) dk. \quad (2.50)$$

Similar, an expression can be obtained for the dissipation by

$$\varepsilon_\chi = \int_0^{\infty} 2\nu k^2 E_\chi(k) dk. \quad (2.51)$$

From the Second Similarity-Hypothesis of Kolmogorov follows that, in the inertial range the energy spectrum is an universal function of ε and can expressed as

$$E_\chi(k) = C_\chi \varepsilon^{-1/3} \varepsilon_\chi k^{-5/3}, \quad (2.52)$$

where C_χ is the Kolmogorov constant of flow variable χ . For the spectrum of velocity components $\chi = u_i$, the Kolmogorov constant depends on direction and it is $\varepsilon_{u_i} = \varepsilon$. For the energy spectrum of scalars (temperature, moisture), C_χ corresponds to the Corrsin constant (Kaimal and Finnigan, 1994).

Based on Eq. (2.52) various characteristic turbulence length scales can be derived (Kaimal and Finnigan, 1994; Durand *et al.*, 2000). Since they are strong associated with the local TKE of the flow, their use in parameterisations of eddy diffusivity (Eqs. (2.8)-(2.9)) could improve the consideration of vertical stratification in local closure schemes, compared to the stability functions approach.

2.4.1 Peak wavelength of the wavenumber weighted energy spectrum

Using measurements during the Minnesota and Ashchurch experiments, Caughey and Palmer (1979) proposed an approximation for the peak wavelength $(\lambda_m)_w$ of the vertical velocity energy spectrum in terms of CBL depth z_i , which can be used as turbulent mixing length in eddy diffusivity parameterisations (Sun and Chang, 1986; Degrazia *et al.*, 1997). The approximation is given as

$$(\lambda_m)_w = \begin{cases} c_0 z & \text{for } -L_{\text{MO}} \leq z \leq 0.1z_i \\ c_1 z_i (1 - e^{-c_2 z/z_i} - c_3 e^{c_4 z/z_i}) & \text{for } 0.1z_i \leq z \leq z_i, \end{cases} \quad (2.53)$$

where $(c_0, c_1, c_2, c_3, c_4) = (5.9, 1.8, 4.0, 0.0003, 8.0)$ are constants and L_{MO} is the Monin-Obukhov length scale.

Generally, the peak wavelength $(\lambda_m)_\chi$ of a turbulent flow variable χ can be derived from the peak wavenumber $(k_m)_\chi$ of the wavenumber weighted energy spectrum $kE_\chi(k)$ by

$$(\lambda_m)_\chi = 2\pi / (k_m)_\chi. \quad (2.54)$$

However, this approach is often restricted to the vertical velocity w , since only w systematically shows a well-defined peak in the energy spectrum (Kaimal *et al.*, 1976; Højstrup, 1982; Durand *et al.*, 2000). Therefore, as far as known, there is no approximation for the peak wavelength of temperature or moisture spectrum in terms of CBL depth. This might be due to the complicated superposition of surface-generated and entrainment-induced eddies (Kaimal and Finnigan, 1994) and to the impact of the diurnal cycle on scalar spectra (Durand *et al.*, 2000).

2.4.2 Integral length scale

A further characteristic turbulence length scale, related to the turbulent mixing of a quantity χ is given by the integral length scale Λ_χ . This length scale is related to the low-frequency part of the energy spectrum (Kaimal and Finnigan, 1994) by

$$\Lambda_\chi = \frac{\pi E_\chi(0)}{\overline{\chi'^2}}, \quad (2.55)$$

where $\overline{\chi'^2}$ is the variance of χ . Since $E_\chi(0)$ is difficult to determine (Kaimal and Finnigan, 1994), the definition of Λ_χ as

$$\Lambda_\chi = \frac{1}{R_{\chi_i \chi_i}(0)} \int_0^\infty R_{\chi_i \chi_i}(r) dr \quad (2.56)$$

is used in measurements (Lenschow and Stankov, 1986; Durand *et al.*, 2000) and numerical simulations (e.g., Khanna and Brasseur (1998)).

Furthermore, Λ_χ is the key quantity to determine the error variance σ_χ^2 between estimated average and the ensemble average of the measured or simulated turbulence statistics (Lumley and Panofsky, 1964; Lenschow and Stankov, 1986; Lenschow *et al.*, 1994; Schröter *et al.*, 2000).

To obtain reliable statistics, measurements and numerical simulations of turbulent flow variables, the averaging length $l_{\sigma_\chi^2}$ have to fulfil the condition

$$l_{\sigma_\chi^2} = \frac{2\overline{\chi^2}\Lambda_\chi}{\overline{\chi}^2\left(\frac{\sigma_\chi}{\overline{\chi}}\right)^2}, \quad (2.57)$$

where $\sigma_\chi/\overline{\chi}$ is the relative error of χ .

However, large $l_{\sigma_\chi^2}$ required for higher-order statistical moments (variance, skewness, kurtosis) leads in some cases to observed differences between measurements and LES (Lenschow *et al.*, 1994; Bösenberg, 1998; Wulfmeyer, 1999; Lenschow *et al.*, 2000). Thus, the design of large-eddy simulations need careful consideration of possibilities to decrease σ_χ^2 (Chlond, 1999). In this work, time-averaging of turbulent flow variables as well as averaging over horizontal model levels were used.

An approximation for integral length scale of vertical velocity was suggested by Lenschow and Stankov (1986) based on different aircraft measurement campaigns in continental and marine CBLs. They found best agreement with their measurements for

$$\Lambda_w/z_i = C(z/z_i)^{1/2}, \quad \text{where } C = (0.24 \pm 0.04). \quad (2.58)$$

This approximation of Λ_w will be compared against LES results in Sec. 3.3.

2.4.3 Dissipation length scale

Local closure schemes based on a prognostic equation of TKE (e.g., MY25 in Sec. 2.2) require a characteristic model length scale for parameterisation of eddy dissipation (e.g. Λ_1 in MY25 or ℓ_ε in the dual-choice length scale formulation of Bougeault and Lacarrère (1989)). Various definitions have been proposed in literature (see, e.g., Durand *et al.* (2000) for an overview) to approximate the dissipation length scale in terms of the energy spectrum (Eq. (2.52)). Since all these definitions are based on approximations of the inertial subrange, they are proportional to each other (Durand *et al.*, 2000). One of the simplest definition of the dissipation length scale ℓ_{ε_χ} for a flow variable χ is based on dimensional arguments and given as

$$\ell_{\varepsilon_\chi} = \left(\frac{\overline{\chi'^2}}{A_\chi^2}\right)^{3/2}, \quad (2.59)$$

with

$$A_\chi^2 = \frac{3}{2}\Gamma\left(\frac{1}{3}\right)C_\chi\varepsilon^{-1/3}, \quad (2.60)$$

where Γ denotes the Gamma function and C_χ is the Kolmogorov constant (Eq. (2.52))

2.4.4 Relations between characteristic turbulence length scales

Although all characteristic turbulence length scales are defined in terms of energy spectrum, there is no a priori relation between these three scales (Durand *et al.*, 2000). However, based on a relationship for the peak wavenumbers $(k_m)_w$ of vertical velocity spectrum proposed by Kaimal *et al.* (1972) as

$$\frac{kE_w(k)}{w'^2} = \frac{B \left\{ \frac{k}{(k_m)_w} \right\}}{1 + B \left\{ \frac{k}{(k_m)_w} \right\}^{5/3}}, \quad (2.61)$$

relations between peak wavelength $(\lambda_m)_w$, integral length scale Λ_w , and dissipation length scale ℓ_ε can be derived (Durand *et al.*, 2000). Using the constant B , determined from measurements to $B = 0.164$ (Durand *et al.*, 2000) the ratio between these characteristic turbulence length scales is given as

$$\frac{(\lambda_m)_w}{\Lambda_w} = 4 \left(\frac{2}{3} \right)^{3/5} B^{-2/5} \approx 6.4 \quad (2.62)$$

$$\frac{\Lambda_w}{\ell_\varepsilon} = \frac{\pi B}{2} \left\{ \frac{3\Gamma\left(\frac{1}{3}\right)}{2} \right\}^{3/2} \approx 2.1 \quad (2.63)$$

$$\frac{(\lambda_m)_w}{\ell_\varepsilon} = 2\pi \left(\frac{3}{2} \right)^{9/10} B^{3/5} \left\{ \Gamma\left(\frac{1}{3}\right) \right\}^{3/2} \approx 13.3. \quad (2.64)$$

Assuming an analytical relationship (Eq. (2.62)) the constant relations between $(\lambda_m)_w$, Λ_w , and ℓ_ε suggest their use in turbulent mixing length formulations, where the various characteristic model length scales are assumed to be proportional to each other (e.g., Mellor-Yamada model). Thus, characteristic turbulence length scales could be applied in local closure schemes as a replacement for the master length scale approach. Due to the inherent stability dependence of the characteristic turbulence length scales (Gossard, 1960; Busch and Larsen, 1972; Dubrulle and Niino, 1992), in this approach, dimensionless stability functions are no longer required.

Large-eddy simulation of convective boundary layers

3.1 Modelling system and setup

3.1.1 The MPI 3D large-eddy simulation model

The MPI 3D large-eddy simulation model (hereafter referred as LES model), developed by Chlond (1992) was used to generate a database containing artificial CBLs of varying stability state. This LES model considers the water cycle including cloud formation and takes into account effects of radiation and SGS condensation/evaporation. LES studies using this model provided valuable contributions in investigations of cloud development during arctic cold air outbreaks (Chlond, 1992; Müller and Chlond, 1996), of developing stratocumulus topped PBLs (Moeng *et al.*, 1996), and of shallow cumulus convection (Brown *et al.*, 2002).

Since a comprehensive description of the LES model is provided in Chlond (1992, 1999) only a brief summary of the main model properties will be given here. The model solves the set of filtered Boussinesq-approximated prognostic equations for wind velocity components u, v, w and active scalars (liquid water potential temperature θ_l and total water content q). The use of the liquid water potential temperature rather than the potential temperature as prognostic variables avoids the explicit consideration of condensation and evaporation processes in the governing equations (Chlond, 1999, pg. 17).

A second-order accurate central differences scheme for the momentum (Williams, 1969; Piacsek and Williams, 1970) and a modified Bott-scheme for scalars (Bott, 1989a,b; Chlond, 1994) were used for the discretisation of model variables, distributed on an Arakawa-C/Lorenz grid. Furthermore, the Adams-Bashforth scheme and an Euler time differencing were applied for time integration of prognostic variables. To ensure incompressibility, the pressure was determined diagnostically using the solution of a Poisson-equation. This approach is based on the Fast-Fourier-transformation method in horizontal direction and a finite-differencing method in vertical direction (Chlond and Wolkau, 2000).

The effects of the unresolved sub-filter structures were modelled based on a local closure approximation of order $1\frac{1}{2}$ after Deardorff (1980) and Sykes *et al.* (1988). The subgrid-scale model solved a prognostic equation for SGS residual kinetic energy $\bar{\epsilon}$ and considered thermal stratification. Although the Deardorff $1\frac{1}{2}$ -order scheme was designed for SGS turbulence, its basic equations are very similar to those of the Level 2.5 Mellor-Yamada local closure approx-

imation scheme. The main difference is related to the definition of the turbulent mixing length formulation (Xue *et al.*, 1996). Whereas the mixing length in the Deardorff scheme is closely related to the model grid spacing, those in the MY-model is supposed to reflect the intrinsic characteristic model length scales, irrespective of the grid spacing.

To simulate cloud formation, the liquid water content was diagnostically determined using an approach developed by Sommeria and Deardorff (1977) including a subgrid-scale condensation scheme. This approach allowed for the dependence of partial cloud cover on SGS variances and covariances of temperature and moisture field (Chlond, 1992; Moeng *et al.*, 1996). Absorption and emission of infrared radiation by cloud droplets were taken into account, whereas net shortwave solar radiative heating and the influence of gaseous absorbers were neglected.

3.1.2 Initial and boundary conditions

The simulations were performed on a model domain of size $L_x \times L_y \times L_z$ with $L_x = L_y = 6.4$ km and $L_z = 4.4$ km using an uniform grid spacing of $\Delta x = \Delta y = 2.5 \cdot \Delta z = 100$ m. The domain size corresponded to a multiple of four to six the boundary layer height in the horizontal, and three to four in the vertical direction. This condition ensured that all convective thermals occurring in the simulated CBLs were captured.

Periodic boundaries were used in both horizontal directions. The domain was assumed to be horizontally homogeneous. The upper boundary condition led to vanishing vertical velocity w at domain top and fixed the gradients of q and θ_l at their initial values. Associated with applying of a Rayleigh friction term this condition avoided the transmission of gravity waves, which can be generated in stable layers (Chlond, 1992).

The influence of mesoscale meteorological processes was neglected except for a horizontally homogeneous subsidence applied at domain top. At lower boundary, a horizontal homogeneous sensible surface heat flux fixed at a constant value was specified for all simulations to drive the CBL. In consistency with a roughness length of $z_0 = 0.035$ m, a Bowen ratio β of sensible to latent surface heat flux with $\beta = 0.5$ was assumed to determine the latent surface heat flux for simulations of moisture-containing boundary layers.

A Coriolis parameter of $f = 8.5 \cdot 10^{-5} \text{ s}^{-1}$ and an initial pressure of $p_0 = 970$ hPa were used. Further details on initial parameters of the LES database are given in Table 3.1.

The simulations were initialised by one-dimensional profiles of geostrophic wind, liquid water potential temperature, and total water content. Whereas the shape of initial profiles of \bar{u}_g, \bar{v}_g and \bar{q} was the same for all simulations, two different types of initial temperature profiles representing different boundary layer states were applied. Runs A, B, G, H, K, and N were initialised by a temperature profile of a well mixed atmosphere. They used an uniform initial temperature profile of $\bar{\theta}_l = 300$ K below the initial boundary layer height $z_{i,0} = 1000$ m and a constant lapse rate of $\Gamma_{\theta_l} = 5.0 \cdot 10^{-3} \text{ K m}^{-1}$ above. To prevent a rapid growth of the simulated PBL, a strong temperature jump of $\Delta \bar{\theta}_l = 8$ K was applied at $z_{i,0}$ corresponding to a rigid lid condition often used in LES (Moeng *et al.*, 1996; Sullivan *et al.*, 1998; Khanna and Brasseur, 1998). The second type of initial temperature profile, used for runs with vanishing temperature jump at $z_{i,0}$, was related to a stably stratified atmosphere with a lapse rate of $\Gamma_{\theta_l} = 5.0 \cdot 10^{-3} \text{ K m}^{-1}$ below $z_{i,0}$

TABLE 3.1: Initial parameters of the large-eddy simulations, where $\overline{(w'\theta')_s}$ is the sensible surface heat flux, $\overline{(w'q')_s}$ is the latent surface heat flux, \bar{u}_g and \bar{v}_g are geostrophic wind components, z_{i_0} is the initial boundary layer height, $\Delta\bar{\theta}_l$ is the temperature jump at $z = z_{i_0}$, $\bar{q}^<$ is the total water content for $z < z_{i_0}$ and $\bar{q}^>$ is the total water content for $z > z_{i_0}$.

Case	$\overline{(w'\theta')_s}$ (K m s ⁻¹)	$\overline{(w'q')_s}$ (m s ⁻¹ g kg ⁻¹)	\bar{u}_g (m s ⁻¹)	\bar{v}_g (m s ⁻¹)	z_{i_0} (m)	$\Delta\bar{\theta}_l$ (K)	$\bar{q}^<$ (g kg ⁻¹)	$\bar{q}^>$ (g kg ⁻¹)
A	0.05	0.04	20	0	1000	8	24	3
B	0.05	0.04	10	0	1000	8	24	3
C	0.2	0.16	20	0	1500	0	12	3
D	0.2	0	15	0	1500	0	0	0
E	0.2	0.16	15	0	1500	0	12	3
F	0.2	0.16	15	0	1500	0	15	3
G	0.1	0.08	10	0	1000	8	24	3
H	0.15	0.12	10	0	1000	8	24	3
I	0.2	0	10	0	1500	0	0	0
J	0.2	0.16	10	0	1500	0	6	3
K	0.2	0.16	10	0	1000	8	24	3
L	0.2	0.16	10	0	1500	0	12	3
M	0.2	0.16	10	0	1500	0	18	3
N	0.2	0.16	10	0	1000	8	24	3

and a capping inversion with $\Gamma_{\theta_l} = 8.0 \cdot 10^{-3} \text{ K m}^{-1}$ above.

Convective boundary layers of different moisture content (including clear CBLs of cases D and I) were simulated using different values of the latent surface heat flux. Furthermore, various initial profiles of the total water content, which differed in magnitude of q below z_{i_0} were applied. Above z_{i_0} , except for cases D and I the initial total water content was set to a constant value of $\bar{q} = 3 \text{ g kg}^{-1}$.

An uniform initial horizontal wind profile with varying magnitude of zonal component \bar{u} and vanishing meridional component \bar{v} was used to impose shear in the simulated CBLs. The impact of a non-uniform initial wind profile on the turbulence structure was investigated in case N, where a constant wind of $\bar{u} = 5 \text{ m s}^{-1}$ below z_{i_0} and $\bar{u}_g = 10 \text{ m s}^{-1}$ above was used.

The large-scale subsidence applied at domain top was set to $\bar{w}_{LS} = -5.0 \cdot 10^{-2} \text{ m s}^{-1}$ with a linear decrease to the surface. LES intercomparison studies have been shown that complete removal of large-scale subsidence has only a minor impact on simulation results (Brown *et al.*, 2002) Therefore, a test case (case A) with vanishing \bar{w}_{LS} was performed. The initial sub-grid TKE, required by the prognostic equation for subgrid-scale TKE was set to $0.15 \cdot (1.0 -$

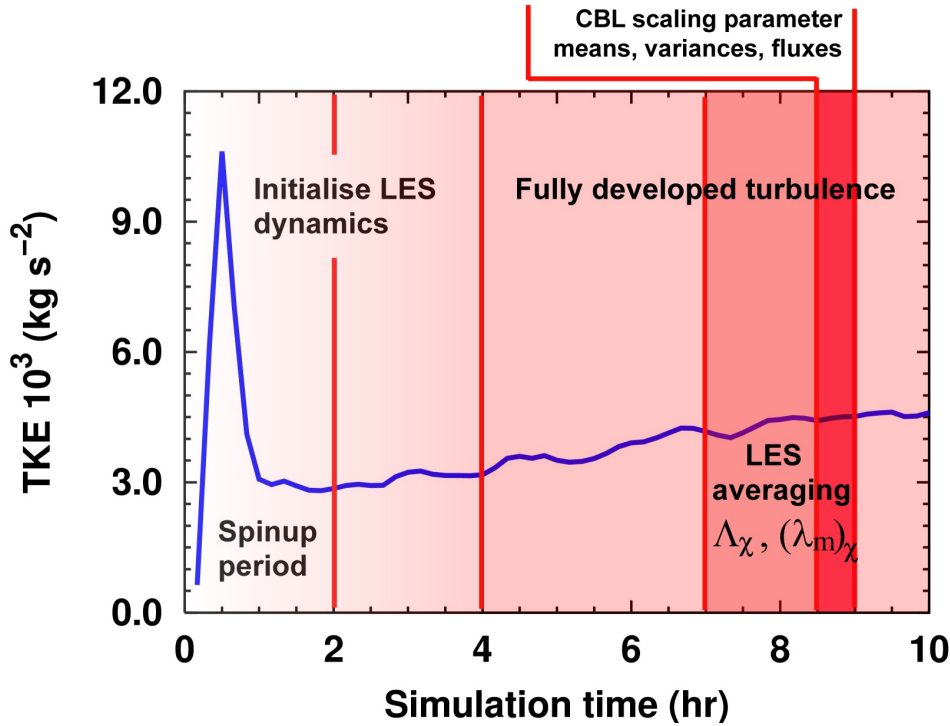


FIGURE 3.1: Time evolution of vertically integrated total (resolved+subgrid) TKE (case K).

$z/150$) $\text{kg m}^{-1}\text{s}^{-2}$ for $z < 150$ m, and to zero for $z \geq 150$ m. Since at initial time no resolved-scale turbulence existed, small random temperature perturbations of 0.1 K were imposed at each grid point in the lowest model level decreasing linearly to zero at $z = 200$ m.

Using a time step of $\Delta t = 2$ s, the computation of each database run covering 10 hrs integration time required about 40 hrs computation time on 2 GHz Intel[®]-Xeon[™] workstations or IBM[®] Power4[™] systems.

The example integration sequence of LES as shown in Fig. 3.1 used the vertically integrated TKE to illustrate the different simulation stages. During the first 2 hrs, the simulation was in a spin-up period, where the integrated TKE showed a pronounced peak. After 2 hrs integration time, the integrated TKE increased linearly indicating that turbulence reached a quasi-steady state. The initialisation of the LES dynamics was finished at latest after 4 hrs integration time. The following range of fully developed turbulence was used to derive time-averaged turbulent mixing length scales of the LES flow variables. An averaging interval of 2 hrs was considered to be sufficient to obtain a reliable statistics of peak wavelength and integral length scale, derived from LES. The CBL scaling parameter, means, variances, and fluxes were determined from a half hour average of the LES flow variables at final simulation state after 9 hrs integration time.

3.2 Properties of the large-eddy simulation database

Based on various CBL scaling variables (Deardorff, 1970a), the properties of the simulated CBLs were examined. The friction velocity u_* was used to describe shear induced turbulence in the simulated CBLs. Based on the Monin-Obukhov similarity theory approach, u_* was iteratively calculated in the LES model. Thus, the difference of mean horizontal wind velocity between the surface value and its value at the first computational grid point above the surface was taken into account (Chlond, 1992).

The Monin-Obukhov length scale L_{MO} was used as a measure for the thermal stratification of the lower boundary layer. This length scale is defined as

$$L_{MO} = -\frac{\bar{\theta}_v}{\kappa g} \frac{u_*^3}{\overline{(w'\theta'_v)}_s}, \quad (3.1)$$

where $\bar{\theta}_v$ is the virtual potential temperature and $\overline{(w'\theta'_v)}_s$ is the surface buoyancy flux. Thus, L_{MO} is strongly influenced by the friction velocity u_* .

To describe convection induced turbulence in the simulated CBLs, the convective velocity scale w_* was used. The convective velocity scale is related to the magnitude of vertical velocity fluctuations in convective thermals and defined as

$$w_* = \left\{ \frac{g}{\bar{\theta}_v} z_i \overline{(w'\theta'_v)}_s \right\}^{1/3}, \quad (3.2)$$

where the CBL depth z_i is a non-steady state scaling parameter for turbulent processes in convective situations (Stull, 1997). The normalised height in the CBL is defined as

$$z_* = \frac{z}{z_i}. \quad (3.3)$$

Here, z_i is the height of the buoyancy flux minimum (Sullivan *et al.*, 1998; Helmert, 1999). However, some other approaches to determine z_i exist in the literature (Sullivan *et al.*, 1998; Hellmuth, 2000).

The mixed layer convective temperature scale θ_* , defined as

$$\theta_* = \frac{\overline{(w'\theta'_v)}_s}{w_*} \quad (3.4)$$

and the mixed layer convective humidity scale q_* , defined as

$$q_* = \frac{\overline{(w'q')}_s}{w_*} \quad (3.5)$$

were used as further scaling parameter to describe the properties of the simulated CBLs.

To determine the stability state of simulated CBLs, the ratio of shear to convective induced turbulence, expressed by u_*/w_* (Stull, 1997) was used. This ratio yields in terms of z_i and L_{MO}

$$\frac{u_*}{w_*} = - \left(\frac{\kappa L_{MO}}{z_i} \right)^{1/3}. \quad (3.6)$$

TABLE 3.2: LES boundary layer properties, where $-z_i/L_{\text{MO}}$ is the stability parameter, u_* is the surface friction velocity, w_* is the convective velocity scale, θ_* is the mixed layer convective temperature scale, q_* is the mixed layer convective humidity scale, $t_* = z_i/w_*$ is the convective time scale, z_i is the boundary layer depth, L_{MO} is the Monin-Obukhov length scale and $\overline{(w'\theta'_v)}_s$ is the surface heat flux. The coloured lines denote a closer examined subset of representative simulations.

Case	$-z_i/L_{\text{MO}}$	u_* (m s ⁻¹)	w_* (m s ⁻¹)	θ_* (K)	q_* (g kg ⁻¹)	t_* (s)	z_i (m)	$-L_{\text{MO}}$ (m)	$\overline{(w'\theta'_v)}_s$ (K m s ⁻¹)
A	2.12	0.82	1.43	0.040	0.028	1114	1593.30	751.00	0.058
B	5.91	0.50	1.23	0.047	0.032	834	1026.00	173.60	0.058
C	7.09	0.86	2.73	0.084	0.059	586	1600.00	225.80	0.231
D	9.16	0.73	2.06	0.097	0.000	680	1400.00	152.80	0.200
E	10.94	0.75	2.25	0.102	0.071	704	1586.70	145.00	0.231
F	11.41	0.74	2.27	0.102	0.071	714	1620.00	142.00	0.231
G	11.78	0.53	1.65	0.070	0.048	756	1246.70	105.80	0.115
H	17.29	0.56	1.98	0.087	0.061	721	1426.70	82.50	0.173
I	18.69	0.57	2.07	0.097	0.000	676	1400.00	74.90	0.200
J	23.22	0.57	2.21	0.104	0.072	682	1506.70	64.90	0.231
K	23.65	0.58	2.25	0.102	0.071	705	1586.70	67.10	0.231
L	24.89	0.57	2.24	0.103	0.071	702	1573.30	63.20	0.231
M	25.29	0.58	2.30	0.100	0.070	733	1686.70	66.70	0.231
N	48.25	0.46	2.26	0.102	0.071	711	1606.70	33.30	0.231

As seen from Tab. 3.2, the LES derived scaling parameters covered a wide range of different stability states. They reached from $-z_i/L_{\text{MO}} = 2 - 48$ and reflect real CBL conditions. Simulations with $-z_i/L_{\text{MO}} < 10$ correspond to CBLs with small buoyancy and strong shear. The impact of shear production in simulations of strong buoyant flows with $-z_i/L_{\text{MO}} > 10$ can be neglected (Holtslag and Nieuwstadt, 1986). Comparing the CBL scaling parameter of case D with E and I with J showed the impact of latent heat flux and total water content on properties of a moisture-containing CBLs (Tab. 3.2). Whereas moisture had only minor effect on u_* , it led to an increase of w_* ($\sim +10\%$), θ_* ($\sim +7\%$), and z_i ($\sim +10\%$), but to a decrease of $-L_{\text{MO}}$ ($\sim -10\%$). Accordingly, the moisture impact led to increased instability of cases E and J $-z_i/L_{\text{MO}}$ ($\sim +20\%$), compared to the corresponding clear-air cases D and I.

3.2.1 Flow statistics

The LES flow statistics includes statistical moments of the LES flow variables, obtained after 9 hrs integration time. Although their statistical moments approximate the ensemble averages only for homogeneous and steady-state flows, it was shown by Chlond (1999) that spatial and time averaging of LES flow variables can improve statistical significance of LES results. However, the characteristic time scale of the process under consideration has to be smaller than the time interval of time averaging. The typical convective time scale t_* of LES, shown in Tab. 3.2, was in the order of 10-20 min. Therefore, time averaging over 900 time steps (30 min) and spatial averaging over the horizontal domain were used to determine the statistical moments of the LES flow variables.

Since the number of simulations exceeds what could be presented here, only results from a representative subset of simulations will be shown. This subset of LES was denoted by different colours in Tab. 3.2. These colours were hereafter used to identify the subset simulations in figures. The subset of LES includes the following simulations:

- Case B: Moisture-containing CBL of weak instability with weak surface heat flux and moderate geostrophic wind using an initial well mixed temperature profile. This case represents a CBL with moderate friction velocity, small convective velocity scale, small mixed layer convective temperature and moisture scale, and large negative Monin-Obukhov length scale.
- Case G: Moisture-containing CBL of intermediate instability with intermediate surface heat flux and moderate geostrophic wind using an initial well mixed temperature profile. This case represents a CBL with moderate friction velocity, intermediate convective velocity scale, intermediate mixed layer convective temperature, and moisture scale as well as intermediate negative Monin-Obukhov length scale.
- Case J: Moisture-containing CBL of large instability with low total water content (Tab. 3.1) but strong surface heat flux and moderate geostrophic wind using an initial stable stratified temperature profile. This case represents a CBL with moderate friction velocity, large convective velocity scale, large mixed layer convective temperature, and moisture scale as well as small negative Monin-Obukhov length scale.
- Case K: Same initial and boundary conditions as case J, except for a larger magnitude of the total water content in the CBL (Tab. 3.1) and an initial well mixed temperature profile. Compared to case J, this resulted in an increase of u_* , w_* , $-L_{MO}$ ($\sim +2\%$), and z_i ($\sim +5\%$), but in a decrease of θ_* and q_* ($\sim -2\%$).

Mean values

Spatial and time averaged mean values of subset LES flow variables are shown in Fig. 3.2. They are denoted by brackets (e.g., $\langle \bar{\chi} \rangle$), to distinguish these variables from filtered LES flow variables (e.g., $\bar{\chi}$). The mean values of $\langle \bar{u} \rangle$, $\langle \bar{v} \rangle$, $\langle \bar{\theta} \rangle$, $\langle \bar{q} \rangle$ and $\langle \bar{q}_l \rangle$ give insights into the structure of the simulated CBLs at initial and final state.

Due to the same initial wind profile, the shape of the final mean wind profile (Fig. 3.2(a)) agreed well among the subset of database simulations. The magnitude of horizontal wind components grew from surface to $z \sim 100$ m and remained constant in the well mixed layer with only small differences between the various simulations. However, $\langle \bar{u} \rangle$ showed an increase at CBL top, where an decrease occurred for $\langle \bar{v} \rangle$. Above z_i , the wind became geostrophic. Due to the different CBL depths, the corresponding wind jump to geostrophic wind conditions occurred for the various subset simulations at different altitudes. This wind jump can be associated with divergence of lateral momentum transport, related to subgrid-scale eddies and convective rolls (Chlond, 1999).

The final mean potential temperature profiles (Fig. 3.2(b)) clearly showed a near surface super-adiabatic layer, topped by a well mixed layer. Near CBL top, an entrainment zone has been developed, indicated by a sharpening of the inversion strength. This sharpening was related to an entrainment of warm dry air from the free troposphere into the CBL as observed in LES studies (Sullivan *et al.*, 1998; Schmidt and Schumann, 1989) as well as in laboratory experiments of Perera *et al.* (1994). Despite of their different initial profiles, the LES cases J and K showed only small differences in the well mixed layer. However, the stronger temperature lapse rate of the initial stable stratified case J remained to final state and led to a somewhat smaller CBL depth compared to case K. Although cases B and G used the same initial well mixed temperature profile, the lower CBL depth and mean bulk temperature of case B was due to the lower surface heat flux applied in this case. Compared to case G, $(\overline{w'\theta'_v})_s$ of case B was a half.

The final mean profiles of total water content (TWC) (Fig. 3.2(c)) showed a small decrease of $\langle \bar{q} \rangle$ from surface to the CBL top. This effect was related to evaporation of water vapour from the ground and entrainment of dry air from the free troposphere. Above the CBL top, the total water content showed a pronounced decrease to $\langle \bar{q} \rangle = 3 \text{ g kg}^{-1}$. Although subset simulations B, G and K used the same initial total water content, their final TWC within the mixed layer decreased due to entrainment processes. Compared to cases G and K, the smaller surface heat flux of B led to higher final total water content within the mixed layer. However, in case J the final well mixed layer total water content was increased, compared to its initial value.

Compared to K, the smaller TWC of case J led to a smaller liquid water content (LWC) as shown in Fig. 3.2(d). However, the dependence of $\langle \bar{q}_l \rangle$ on surface heat flux showed no consistent behaviour. A large TWC in the bulk of the CBL associated with low surface heat flux (case B) led to a LWC in the same order of magnitude as a high surface heat flux, associated with smaller total water content within the CBL (case K).

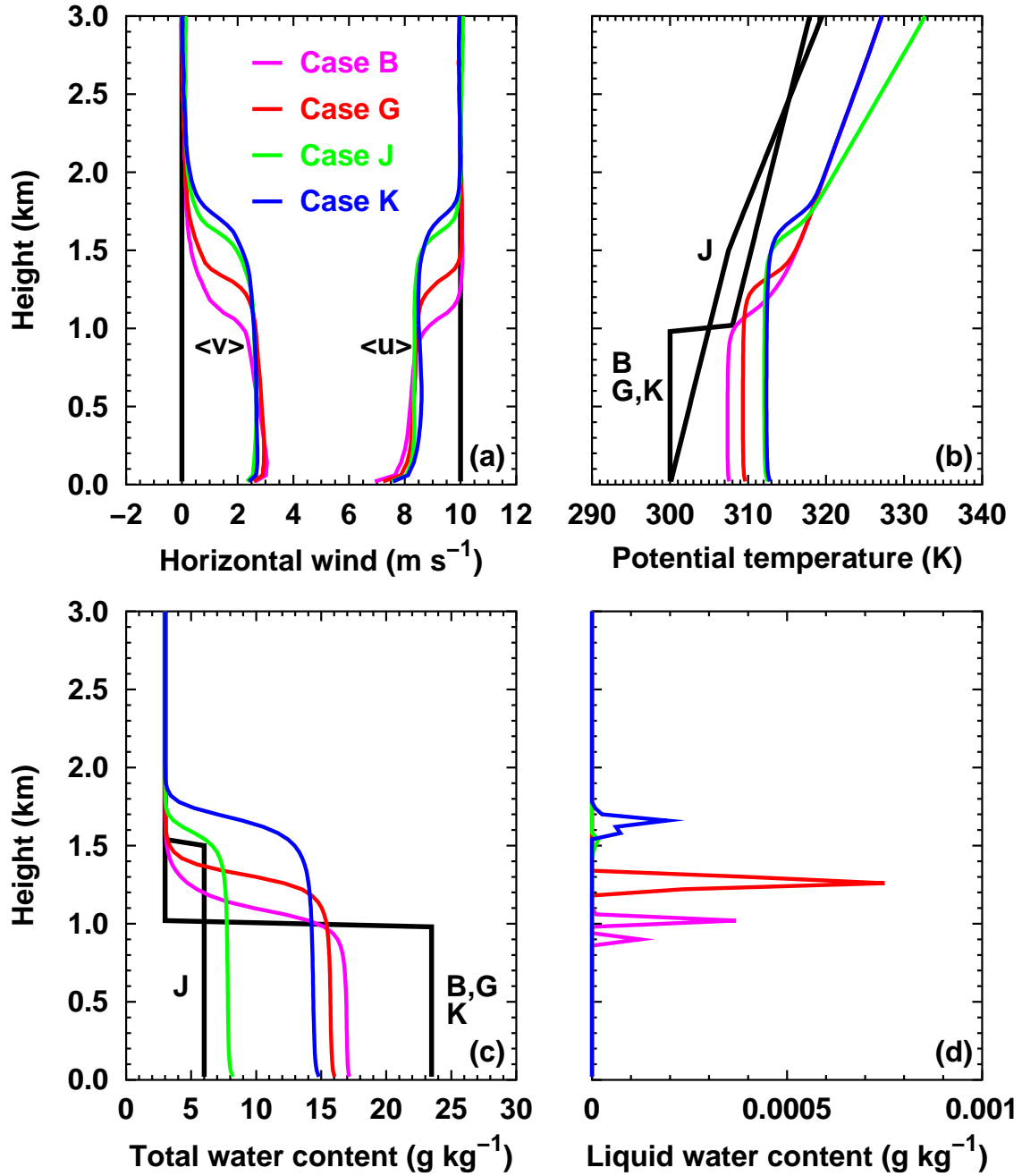


FIGURE 3.2: Vertical profiles of mean LES flow variables of the subset simulation cases B, G, J, and K, where (a) shows the horizontal wind components $\langle \bar{u} \rangle, \langle \bar{v} \rangle$, (b) shows the potential temperature $\langle \bar{\theta} \rangle$, (c) shows the total water content $\langle \bar{q} \rangle$ and (d) shows the liquid water content $\langle \bar{q}_l \rangle$. The black solid lines indicate the initial soundings.

Variations

Final vertical profiles of normalised total and subgrid-scale variances of subset LES flow variables as shown in Fig. 3.3, illustrate that except for the near surface range, the non-resolved subgrid-scale parts of the flow are much smaller than the resolved parts. This indicates a high validity of LES results in bulk of the CBL. Variances of the velocity components, (Fig. 3.3(a,b,c)) illustrate the variation of the turbulent kinetic energy in the vertical and horizontal components of the flow.

The profiles of $\langle \overline{u'^2} \rangle$ and $\langle \overline{v'^2} \rangle$ generally agreed in shape indicating a maximum near the surface due to wind shear. They decreased to a constant value in the well mixed layer and showed a maximum within the entrainment zone just below CBL top. This maximum was due to a transfer of vertical motion of the thermals into horizontal motions (Sullivan *et al.*, 1998). Observed differences of the variance maxima within the entrainment zone for different subset simulations were related to differences in the inversion strength.

The vertical velocity variances (Fig. 3.3(c)) of subset simulations showed a pronounced peak in the well mixed layer, where convection induced mixing was strongest. There, $\langle \overline{w'^2} \rangle$ contributed the main part to the TKE. However, in subset cases J and K this peak occurred in a lower CBL range compared to simulations G and B.

The resolved potential temperature variance, shown in Fig. 3.3(d) decreased from the surface value, remained constant in the well mixed layer, and showed a sharp maximum within the entrainment zone. The magnitude of this peak can be related to the sharpening of the inversion strength (Sullivan *et al.*, 1998). Subset simulations with low surface heat flux (cases B and G) showed a larger peak magnitude of the potential temperature variance than simulations with large surface heat flux (cases J and K). However, a low total water content led to a decrease of the peak magnitude of $\langle \overline{\theta'^2} \rangle$.

Turbulent fluxes

Similar to the variances, the turbulent fluxes of momentum, heat and total water content, shown in Fig. 3.4 indicated a significance of the non-resolved turbulent fluxes only near the surface. However, their impact vanishes in bulk of the CBL.

The zonal momentum flux (Fig. 3.4(a)) showed a linear increase from negative values at the surface to zero above the CBL top. Since all subset simulations used the same uniform initial wind profile, smaller negative values of the zonal momentum flux of cases B and G were mainly related to a CBL forcing with lower surface heat flux. However, the agreement of zonal momentum flux for cases J and K indicated a rather small impact of differences in total water content on $\langle \overline{u'w'} \rangle$.

Due to the initial wind profile using $\bar{v} = 0$ the initial meridional momentum flux vanished. Thus, the non-vanishing final meridional momentum flux $\langle \overline{v'w'} \rangle$ (Fig. 3.4(b)) was a result of the Coriolis force. At final simulation state, $\langle \overline{v'w'} \rangle$ increased from negative values at the surface to positive values in the upper CBL, but showed a decrease to zero above. Simulations with low surface heat flux agreed in their $\langle \overline{v'w'} \rangle$, whereas cases J and K agreed only in $\langle \overline{v'w'} \rangle$ at surface and CBL top, but showed different values in bulk of the CBL.

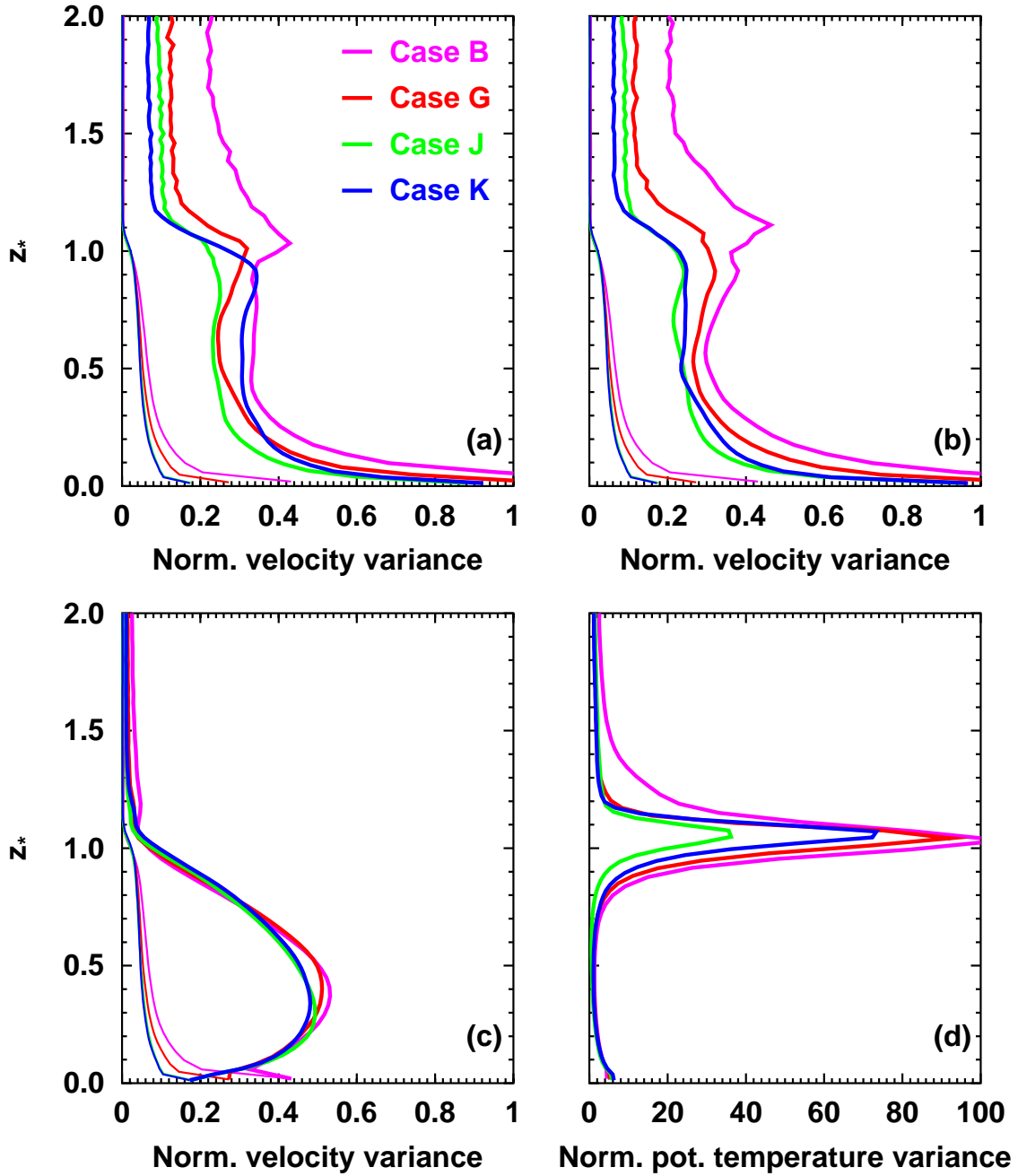


FIGURE 3.3: Vertical profiles of averaged normalised LES variances of the subset simulation cases, where (a) shows the variance of zonal wind velocity $\langle \overline{u'^2} \rangle / w_*^2$, (b) shows the variance of meridional wind velocity $\langle \overline{v'^2} \rangle / w_*^2$, (c) shows the variance of vertical wind velocity $\langle \overline{w'^2} \rangle / w_*^2$, and (d) shows the resolved part of potential temperature variance $\langle \overline{\theta'^2} \rangle / \theta_*^2$. Thick coloured solid lines denote total variances (resolved+subgrid) and thin coloured solid lines denote subgrid scale variances.

The liquid water potential temperature heat flux showed positive values at surface (Fig. 3.4(c)). Above, $\langle \overline{w'\theta'_l} \rangle$ decreased linearly with height reflecting a quasi steady-state behaviour of the turbulence in the well-mixed layer. The minimum of $\langle \overline{w'\theta'_l} \rangle$ was assumed just below CBL top for all subset simulations.

Based on the sensible heat flux $\langle \overline{w'\theta'} \rangle$ and the liquid water flux $\langle \overline{w'q'_l} \rangle$ the liquid water potential temperature heat flux $\langle \overline{w'\theta'_l} \rangle$ is given as

$$\langle \overline{w'\theta'_l} \rangle = \langle \overline{w'\theta'} \rangle - \frac{1}{\pi_E} \frac{L_v}{c_p} \langle \overline{w'q'_l} \rangle, \quad \text{where} \quad \pi_E = (T/\theta)^{R_d/c_p} \quad (3.7)$$

denotes the Exner function. In this formulation, the minimum of $\langle \overline{w'\theta'_l} \rangle$ is related to the point where net condensation changes sign indicating that evaporation becomes larger than condensation (Siebesma *et al.*, 2002). Above z_i , $\langle \overline{w'\theta'_l} \rangle$ increased to small negative values. Differences in $\langle \overline{w'\theta'_l} \rangle$ among the various subset simulations were related to different surface values of $\langle \overline{w'\theta'_l} \rangle$, the slope of the linear decrease, and the minimum value of the $\langle \overline{w'\theta'_l} \rangle$.

Due to evaporation of moisture from surface into the CBL, the total water flux (Fig. 3.4(d)) showed positive surface values. Simulations B, G and K showed a linear increase of $\langle \overline{w'q'_l} \rangle$ indicating entrainment induced net drying of the CBL. However, the linear decrease of $\langle \overline{w'q'_l} \rangle$ of case J indicated a net moistening of the CBL, compared to the initial state (see Fig. 3.2(c)).

3.2.2 Examination of coherent structures

An example of the three-dimensional turbulence patterns of a strong buoyancy-driven CBL is given in Fig. 3.5 showing the time-averaged turbulence structure of subset simulation K at final simulation state.

Iso-surfaces of positive vertical velocity ($w = 0.9 \text{ m s}^{-1}$) were used to highlight the buoyancy-induced convective thermals of the CBL. Driven by the strong positive surface heat flux, these structures originated as small structures near the ground. With increasing height, they grew in diameter to the mid-CBL, whereas a decrease of the thermal diameter was observed near the CBL top (Khanna and Brasseur, 1998; Helmert, 1999).

The upward moving thermals (updraughts) corresponding to regions of positive vertical velocity are associated with compensating regions of negative vertical velocity (downdraughts). These coherent structures dominated the vertical fluxes of momentum, heat and moisture in the simulated CBLs (Lohou *et al.*, 2000). Updraughts and downdraughts were indicated in the horizontal cross section of Fig. 3.5 by coherent green and blue areas, respectively. An examination of the spatial variability of updraughts and downdraughts is given in Fig. 3.6(a,d,g). The organisation of the coherent structures in cellular patterns persisting throughout the CBL is clearly visible (Khanna and Brasseur, 1998). Magnitude and horizontal scale of updraughts and downdraughts showed a maximum at $z_* = 0.5$, but significant smaller values at CBL top. Furthermore, fluctuations of virtual potential temperature and total water content (Fig. 3.6(b, e, h) and (c, f, i)) were examined. Similar to vertical velocity fluctuations, they showed coherent structures, organised in cellular patterns. The magnitude and horizontal scale of these patterns remained nearly constant at $z_* = 0.25$ and $z_* = 0.5$.

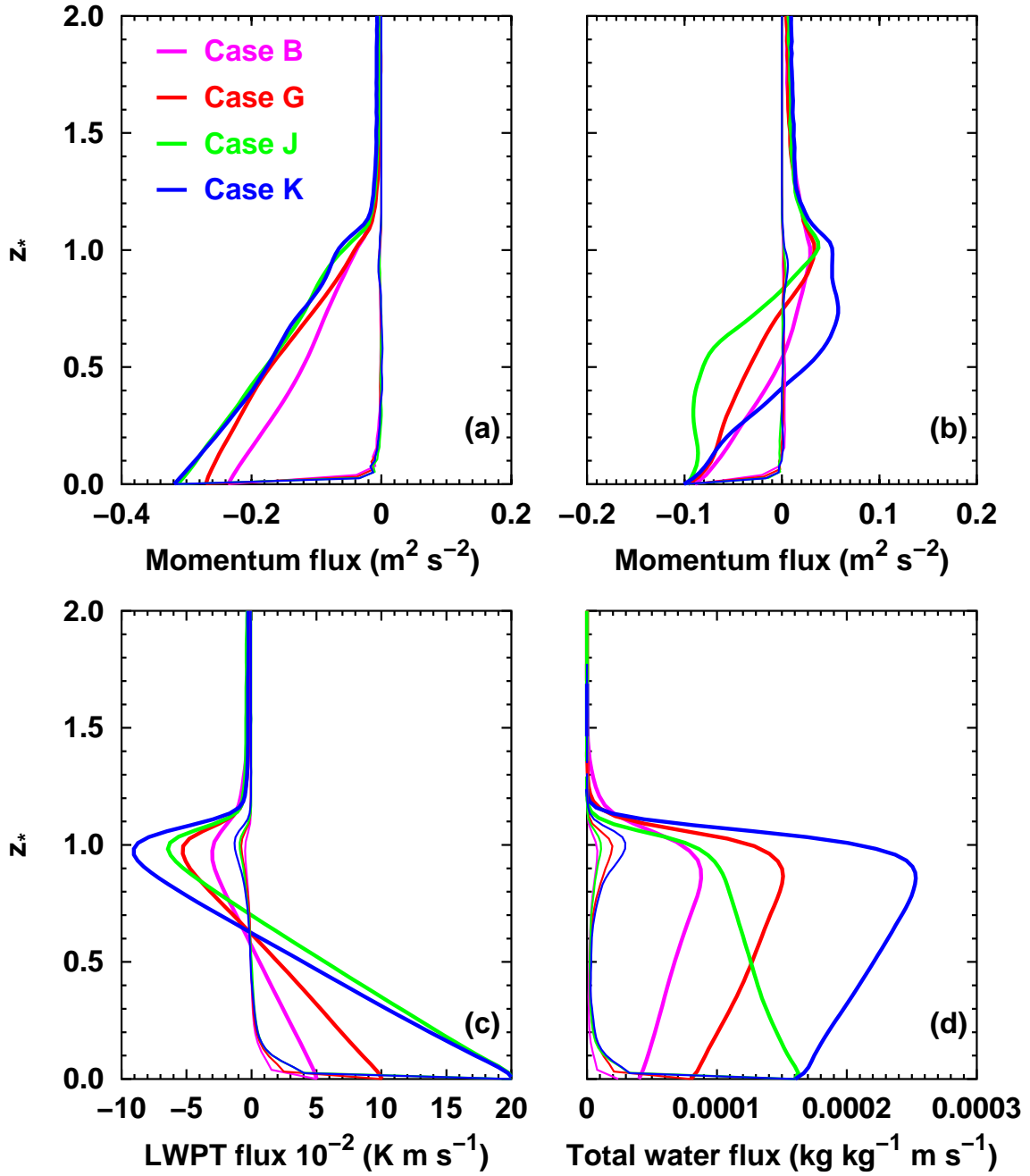


FIGURE 3.4: Vertical profiles of averaged turbulent fluxes of the subset simulation cases, where (a) shows the zonal momentum flux $\langle u'w' \rangle$, (b) shows the meridional momentum flux $\langle v'w' \rangle$, (c) shows the liquid water potential temperature heat flux $\langle w'\theta_l' \rangle$ and (d) shows the total water flux $\langle w'q' \rangle$. Thick coloured solid lines denote total turbulent fluxes (resolved+subgrid) and thin coloured solid lines denote subgrid scale turbulent fluxes.

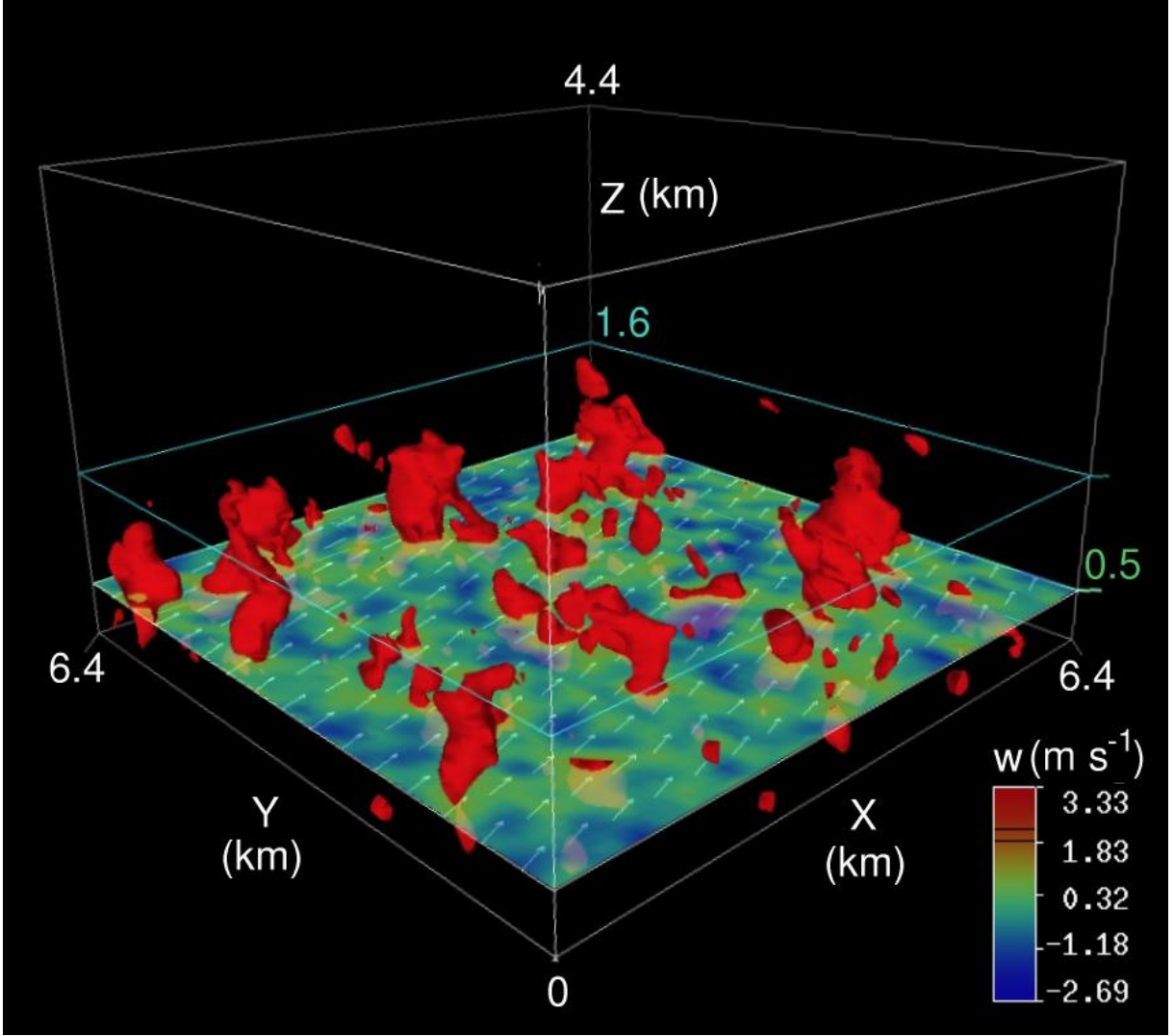


FIGURE 3.5: LES domain of case K, where red-shaded iso-surfaces of vertical velocity ($w = 0.9 \text{ m s}^{-1}$) are used to indicate buoyant thermals. The horizontal cross-section at $z = 0.5 \text{ km}$ shows the horizontal distribution of vertical velocity fluctuations (right legend). The vector field at $z = 0.5 \text{ km}$ indicate the horizontal wind. The blue solid line at $z = 1.6 \text{ km}$ denotes the CBL top.

However, in contrast to updraughts and downdraughts an increase of temperature and moisture fluctuations were observed at CBL top. Based on normalised 2D auto-covariances

$$\tilde{R}_{\chi\chi} = R_{\chi_i\chi_i}(r_x, r_y) / R_{\chi_i\chi_i}(0, 0) \quad \text{using} \quad \chi = (w', \theta'_v, q') \quad (3.8)$$

updraughts and downdraughts as well as coherent structures of temperature and TWC at the CBL levels of Fig. 3.6 were examined.

A pronounced maximum at zero displacement ($r_x = r_y = 0$), followed by a sharp decrease

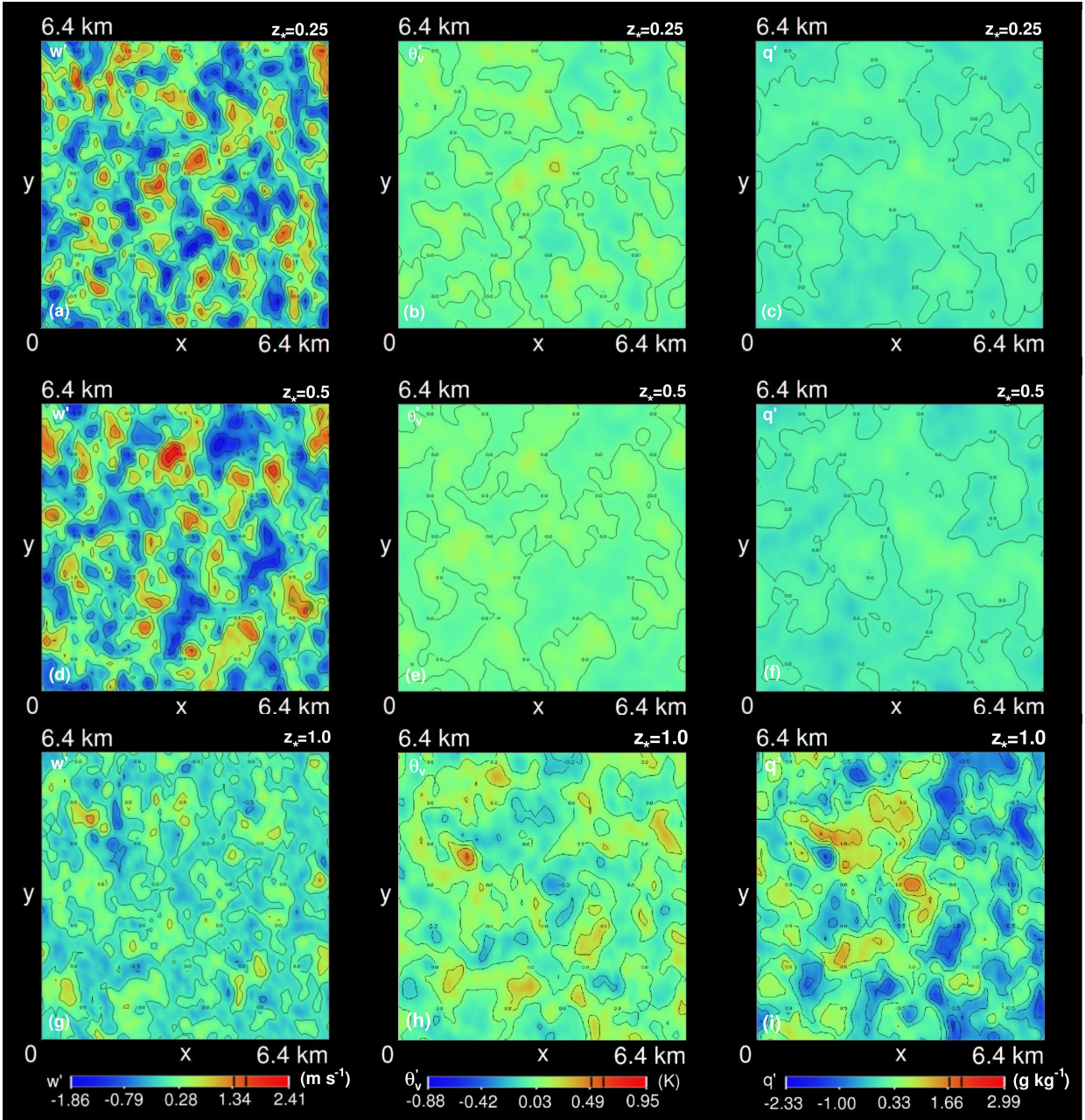


FIGURE 3.6: Horizontal cross sections of fluctuations of LES flow variables (case K) for (a,d,g) vertical velocity w , (b, e, h) virtual potential temperature θ_v , and (c, f, i) total water content q at various CBL levels: top $z_* = 0.25$, centre $z_* = 0.5$, and bottom $z_* = 1.0$.

to zero for $|r_x| = |r_y| > 0$ was observed for all coherent structures and CBL levels (Fig. 3.7). Periodic structures of $\tilde{R}_{\chi\chi}$ indicated the occurrence of role structures within the CBL, as observed in LES studies (Lohou *et al.*, 2000), aircraft measurements (Lohou *et al.*, 1998), and laboratory experiments (Kaiser, 1996). Based on the examination of the distance between two maxima of

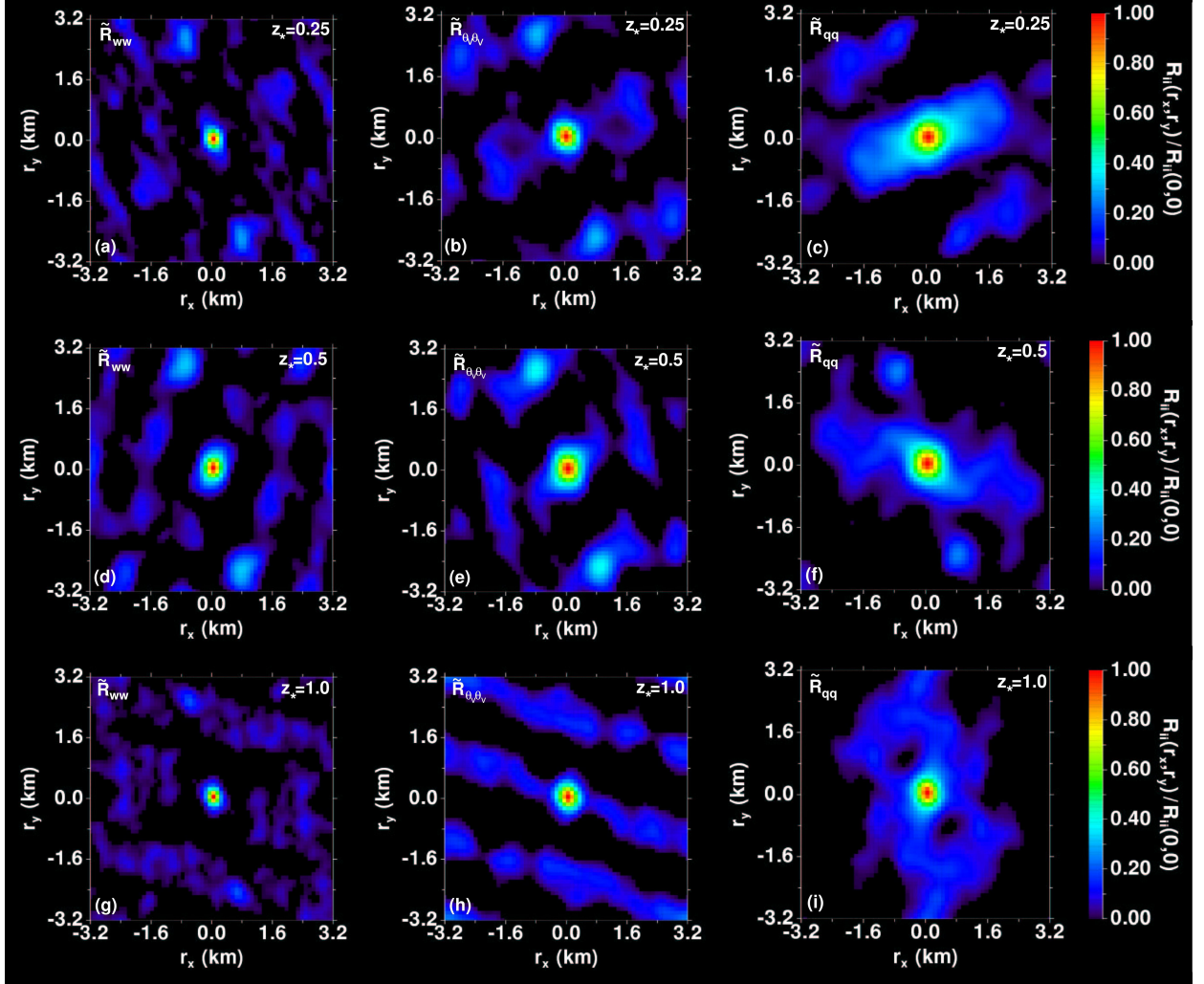


FIGURE 3.7: Two-dimensional normalised auto-covariances based on turbulent fluctuations of LES flow variables, shown in Fig. 3.6.

$\tilde{R}_{\chi\chi}$, the wavelength L_s of these role structures at $z_* = 0.5$ was determined. A wavelength of $L_s = 2$ km was determined for vertical velocity, whereas virtual potential temperature showed $L_s = 2.6$ km. These values agreed in order of magnitude with findings from Kaiser (1996); Lohou *et al.* (1998), and Lohou *et al.* (2000).

3.2.3 Examination of characteristic turbulence length scales

One-dimensional energy spectra $E_\chi(k)$ and auto-covariances $R_{\chi_i\chi_i}(r) = R_\chi(r)$ were used to determine the characteristic turbulence length scales, representative of the simulated CBLs. Since LES explicitly resolves the turbulent structures of the energy-containing range (see Sec. 2.4), the peak wavelength $(\lambda_m)_\chi$ and the integral length scale Λ_χ were considered in this work.

The Fourier transform approach was used to determine $E_\chi(k)$ and $R_\chi(r)$ from turbulent fluctuations of the LES flow variables. Thus, a Fast-Fourier transform (FFT) algorithm after Press *et al.* (1996) was applied on Bartlett filtered one-dimensional samples of $\chi = (w', \theta'_v, q')$. The fluctuations of the flow variables at two-dimensional horizontal LES model levels were sampled in x - and y -pathways. Thus, $N_y = L_y/\Delta y$ samples in x -direction and $N_x = L_x/\Delta x$ samples in y -direction of $\chi = (w', \theta'_v, q')$ were taken into account by the FFT. Based on this method, 1D energy spectra $E_\chi^{y_j}$, representative of x -direction and $E_\chi^{x_j}$ for y -direction, respectively were determined. Furthermore, 1D auto-covariances $R_\chi^{y_j}$ of x -direction and $R_\chi^{x_j}$ of y -direction were derived from $E_\chi^{y_j}$ and $E_\chi^{x_j}$ using the discrete correlation theorem (Press *et al.*, 1996).

Averaged energy spectra and auto-covariances for the different sampling pathways were determined as

$$\langle E_\chi \rangle^x = \frac{1}{N_y} \sum_{j=0}^{N_y-1} E_\chi^{y_j}, \quad \langle E_\chi \rangle^y = \frac{1}{N_x} \sum_{j=0}^{N_x-1} E_\chi^{x_j}, \quad (3.9)$$

$$\langle R_\chi \rangle^x = \frac{1}{N_y} \sum_{j=0}^{N_y-1} R_\chi^{y_j}, \quad \langle R_\chi \rangle^y = \frac{1}{N_x} \sum_{j=0}^{N_x-1} R_\chi^{x_j}. \quad (3.10)$$

Mean 1D energy spectra and auto-covariances, representative of the corresponding horizontal LES model level are given as

$$\langle E_\chi \rangle = \frac{1}{2} (\langle E_\chi \rangle^x + \langle E_\chi \rangle^y), \quad (3.11)$$

$$\langle R_\chi \rangle = \frac{1}{2} (\langle R_\chi \rangle^x + \langle R_\chi \rangle^y). \quad (3.12)$$

Energy spectra

The wavenumber weighted mean 1D energy spectra $k\langle E_\chi(k) \rangle$ of the various LES flow variables χ (Fig. 3.8) showed a pronounced peak at low wavenumbers, related to the energy-containing range. A power-law behaviour (Kolmogorov, 1941) of $k\langle E_\chi(k) \rangle$ was observed toward higher wavenumbers. In agreement with various LES studies (Mason, 1989; Mason and Brown, 1999) the energy spectrum of vertical velocity fluctuations indicated $k\langle E_w(k) \rangle \sim k^{-2/3}$ in a small inertial subrange. Due to the impact of the LES subgrid-scale model, a k^{-2} power law occurred at high wavenumbers.

Similar to vertical velocity, the spectra of temperature and moisture fluctuations indicated a small inertial subrange showing $k\langle E_{\theta_v}(k) \rangle \sim k^{-2/3}$ and $k\langle E_q(k) \rangle \sim k^{-2/3}$ (Corrsin, 1951; Kaimal and Finnigan, 1994). However, they showed a k^{-4} power law in the high-wavenumber range (Moeng and Wyngaard, 1988; Mason, 1989; Muschinski, 1996).

As seen from Fig. 3.8, the magnitude of the spectral peak $k\langle E_\chi((k_m)_\chi) \rangle$ showed a dependence on LES model level. For vertical velocity, a strong decrease of $k\langle E_w((k_m)_w) \rangle$ at CBL top was observed, compared to $k\langle E_w((k_m)_w) \rangle$ in lower and mid-CBL. However, for temperature and moisture, $k\langle E_{\theta_v}((k_m)_{\theta_v}) \rangle$ and $k\langle E_q((k_m)_q) \rangle$ at CBL top were one order of magnitude larger, compared to their value at $z_* = 0.25$ and $z_* = 0.5$.

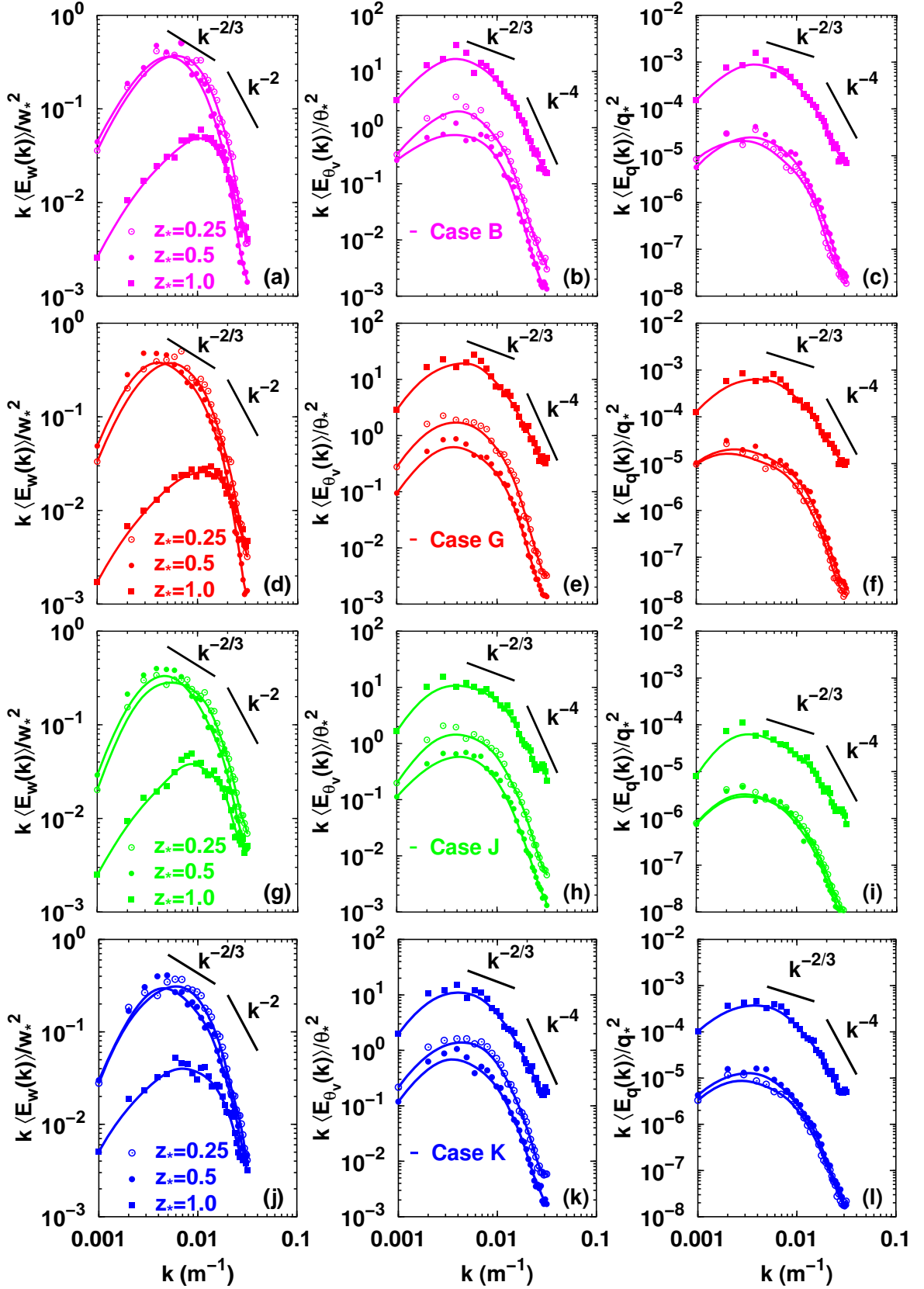


FIGURE 3.8: Wavenumber weighted averaged normalised 1D energy spectra $k\langle E_w(k)\rangle/w_*^2$, $k\langle E_{\theta_v}(k)\rangle/\theta_*^2$, and $k\langle E_q(k)\rangle/q_*^2$ in various LES model levels for (a-c) cases B, (d-f) G, (g-i) J, and (j-l) K, where black solid lines denote theoretically expected $k^{-2/3}$, k^{-2} , and k^{-4} decreases and coloured solid lines indicate Bezier approximation.

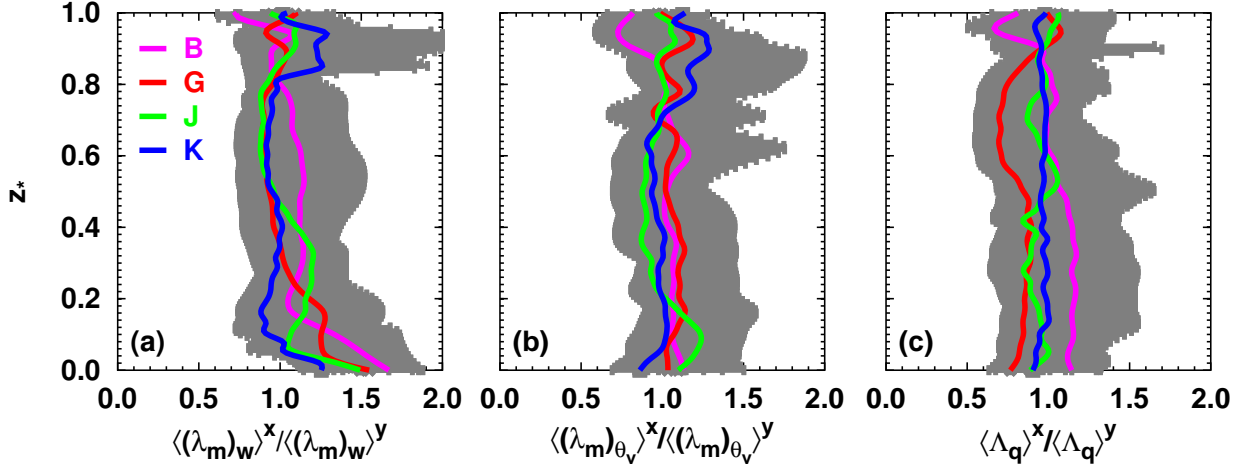


FIGURE 3.9: Ratio of peak wavelengths related to different sampling pathways $\langle(\lambda_m)_\chi\rangle^x/\langle(\lambda_m)_\chi\rangle^y$ for (a) $\chi = w$, (b) $\chi = \theta_v$, and (c) $\chi = q$ using LES cases B, G, J, and K, where grey shaded areas denote the minimum-maximum range using the corresponding standard deviations.

An examination of the spectral peak wavenumber $(k_m)_\chi$ at various LES model levels showed for vertical velocity an increase of $(k_m)_w$ to higher wavenumbers at CBL top, compared to $(k_m)_w$ at lower and mid-CBL. This behaviour indicated a decrease of size for the most-energy containing coherent structures of vertical velocity at CBL top. For virtual potential temperature and TWC, the spectral peak wavenumber $(k_m)_{\theta_v}$ and $(k_m)_q$ remained nearly constant at the various LES model levels.

Furthermore, the dependence of the spectral peak wavenumber $(k_m)_\chi$ on stability state of the simulated CBL was examined. Largest differences were observed for vertical velocity indicating primarily at CBL top a decrease of $(k_m)_w$ to lower wavenumbers with increasing instability from case B to K. For virtual potential temperature and TWC, a somewhat smaller decrease of $(k_m)_{\theta_v}$ and $(k_m)_q$ with increasing instability of the simulated CBL was observed.

Peak wavelengths

The flatness of the energy spectra, due to low number of data points around the spectral peak, led to difficulties in determining the peak wavenumber $(k_m)_\chi$ in bulk of the CBL (Kaiser and Fedorovich, 1998). Thus, Bezier approximations of $k\langle E_\chi(k)\rangle^x$ and $k\langle E_\chi(k)\rangle^y$ based on natural cubic splines (Williams and Kelly, 1995) were used to determine maxima of the energy spectra. The peak wavenumbers $\langle(k_m)_\chi\rangle^x$ and $\langle(k_m)_\chi\rangle^y$ for the x - and y -direction resulted from

$$\langle(k_m)_\chi\rangle^x = \max \left[k\langle E_\chi^B(k)\rangle^x \right] \quad \text{and} \quad \langle(k_m)_\chi\rangle^y = \max \left[k\langle E_\chi^B(k)\rangle^y \right], \quad (3.13)$$

where $k\langle E_\chi^B(k)\rangle^x$ and $k\langle E_\chi^B(k)\rangle^y$ are Bezier approximated energy spectra.

The averaged peak wavelengths $\langle(\lambda_m)_\chi\rangle^x$ and $\langle(\lambda_m)_\chi\rangle^y$ related to x - and y -pathways were determined from $\langle(k_m)_\chi\rangle^x$ and $\langle(k_m)_\chi\rangle^y$ using Eq. (2.54).

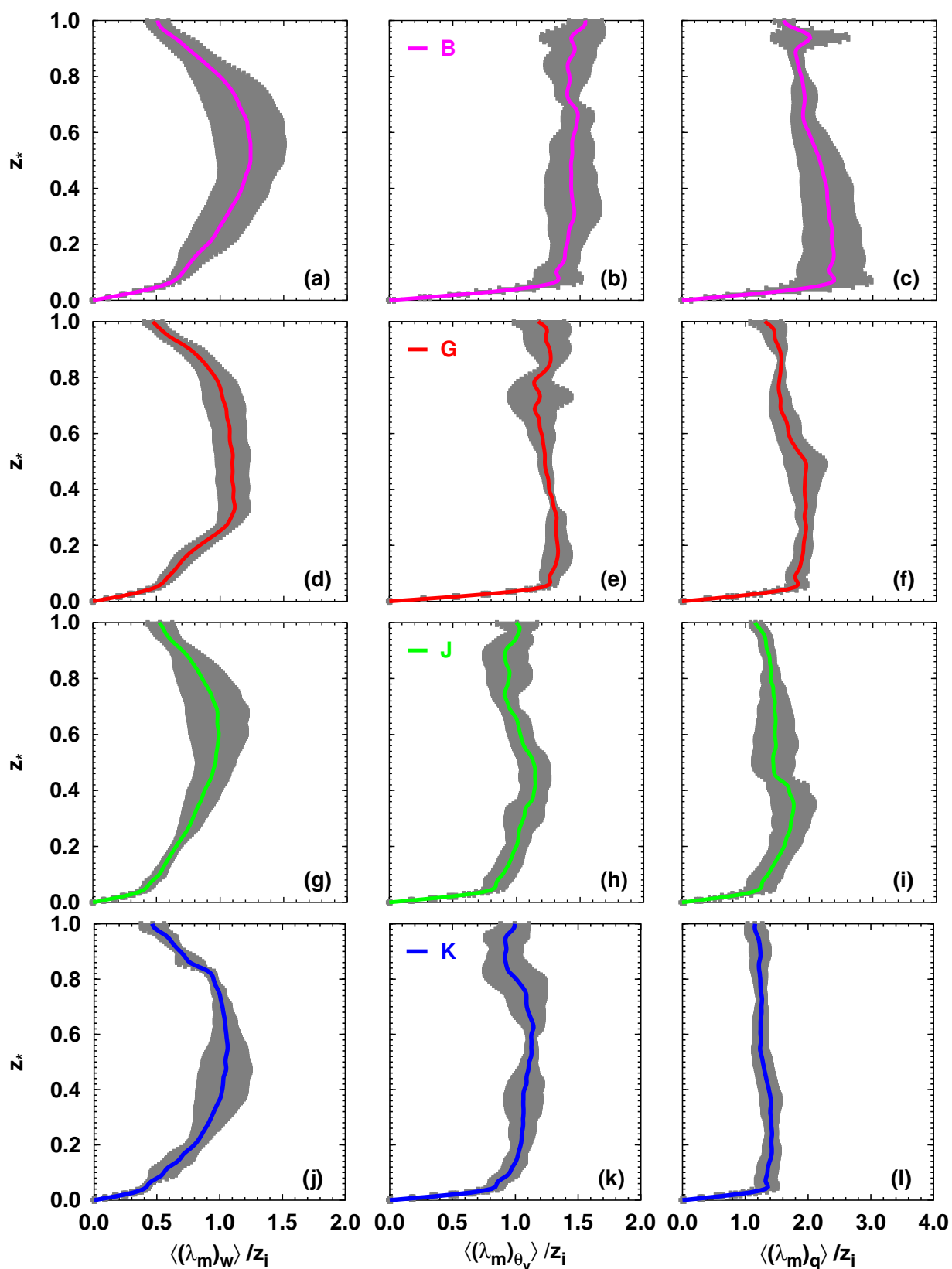


FIGURE 3.10: Horizontally averaged peak wavelengths $\langle(\lambda_m)_w\rangle$, $\langle(\lambda_m)_{\theta_v}\rangle$, and $\langle(\lambda_m)_q\rangle$ (coloured solid lines) for (a-c) cases B, (d-f) G, (g-i) J and (j-l) K. Grey shaded areas denote the standard deviations $\sigma_{(\lambda_m)_w}$, $\sigma_{(\lambda_m)_{\theta_v}}$, and $\sigma_{(\lambda_m)_q}$.

Their standard deviation is given as

$$\sigma_{(\lambda_m)_\chi}^x = \left[\frac{1}{t_{\text{av}}} \sum_{t_{\text{min}}}^{t_{\text{max}}} \left\{ (\lambda_m)_\chi^x - \langle (\lambda_m)_\chi \rangle^x \right\}^2 \right]^{1/2}, \quad (3.14)$$

$$\sigma_{(\lambda_m)_\chi}^y = \left[\frac{1}{t_{\text{av}}} \sum_{t_{\text{min}}}^{t_{\text{max}}} \left\{ (\lambda_m)_\chi^y - \langle (\lambda_m)_\chi \rangle^y \right\}^2 \right]^{1/2}, \quad (3.15)$$

where the averaging time interval t_{av} was 2 hrs (see Fig. 3.1) starting from $t_{\text{min}} = 7$ hrs to $t_{\text{max}} = 9$ hrs integration time.

As illustrated in Fig. 3.9, the ratio of $\langle (\lambda_m)_\chi \rangle^x$ and $\langle (\lambda_m)_\chi \rangle^y$ was approximately unity in the bulk of the CBL, except for the near surface range. Using the averaged sampling peak wavelengths, the mean peak wavelengths of the LES flow variables are given as

$$\langle (\lambda_m)_\chi \rangle = \frac{1}{2} \left(\langle (\lambda_m)_\chi \rangle^x + \langle (\lambda_m)_\chi \rangle^y \right), \quad (3.16)$$

and their standard deviation is

$$\sigma_{(\lambda_m)_\chi} = \left[\frac{1}{t_{\text{av}}} \sum_{t_{\text{min}}}^{t_{\text{max}}} \left\{ (\lambda_m)_\chi - \langle (\lambda_m)_\chi \rangle \right\}^2 \right]^{1/2}. \quad (3.17)$$

The vertical profiles of $\langle (\lambda_m)_w \rangle$, $\langle (\lambda_m)_{\theta_v} \rangle$, and $\langle (\lambda_m)_q \rangle$ (Fig. 3.10) showed a linearly increase from surface to $z_* \sim 0.1$. Above this level, $\langle (\lambda_m)_w \rangle$ showed a maximum in the mid-CBL indicating that the mean diameter of the most energy-containing updraughts and downdraughts assumes a value close to the CBL depth (Helmert and Hellmuth, 2000).

Since the CBLs were capped by an inversion, vertical fluctuations were prevented at CBL top. This led to the observed decrease of $\langle (\lambda_m)_w \rangle$ at CBL top (see Fig. 3.8). Due to the observed large fluctuations of temperature and moisture, even at CBL top (see Sec. 3.2.2), $\langle (\lambda_m)_{\theta_v} \rangle$ and $\langle (\lambda_m)_q \rangle$ indicated no decrease in the upper CBL, but remained nearly constant from $z_* \sim 0.1$ -1.

As seen from Fig. 3.10 the peak wavelengths $\langle (\lambda_m)_w \rangle$, $\langle (\lambda_m)_{\theta_v} \rangle$, and $\langle (\lambda_m)_q \rangle$ indicated a dependence on stability state of the considered CBL. Largest values of peak wavelengths were observed for cases with small values of $-z_i/L_{\text{MO}}$ (e.g., case B). However, an increase of CBL instability led to a decrease of $\langle (\lambda_m)_w \rangle$, $\langle (\lambda_m)_{\theta_v} \rangle$, and $\langle (\lambda_m)_q \rangle$.

Auto-covariances

The normalised mean 1D auto-covariances (auto-correlations) $\langle \tilde{R}_\chi \rangle$, determined from fluctuations of LES flow variables $\chi = (w', \theta'_v, q')$ (Fig. 3.11) showed with increasing displacement r an exponential like decrease to small values. This behaviour agreed with findings from the 2D auto-covariances of LES flow variables (see Sec. 3.2.2, Fig. 3.7). Non-vanishing auto-correlations of $\langle \tilde{R}_\chi \rangle \geq 0.3$ were related to the occurrence of organised coherent structures within the CBL.

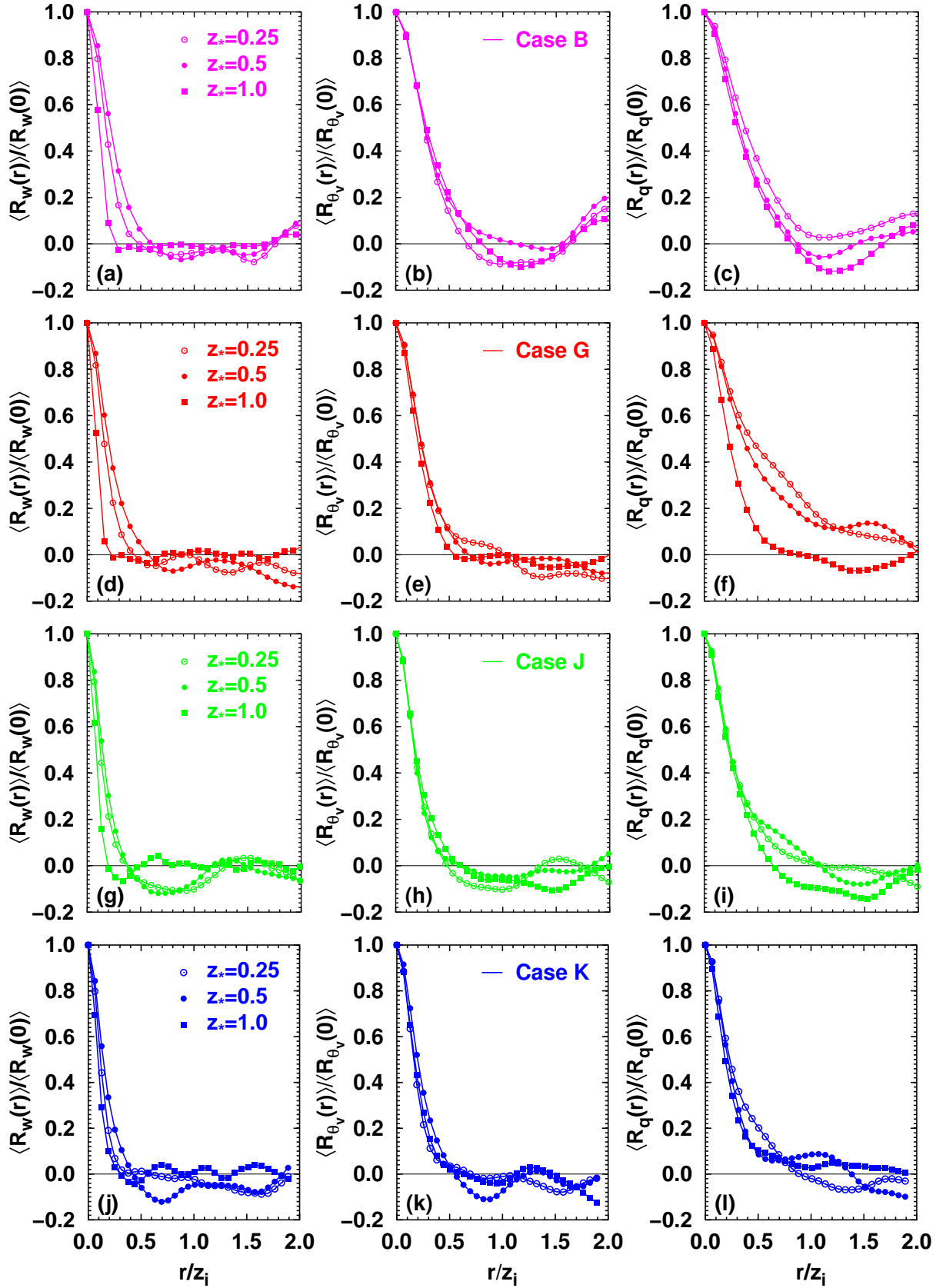


FIGURE 3.11: Averaged normalised 1D auto-covariances $\langle R_w(r) \rangle / \langle R_w(0) \rangle$, $\langle R_{\theta_v}(r) \rangle / \langle R_{\theta_v}(0) \rangle$, $\langle R_q(r) \rangle / \langle R_q(0) \rangle$ in various LES model levels for (a-c) cases B, (d-f) G, (g-i) J and (j-l) K.

An examination of the decrease of $\langle \tilde{R}_\chi \rangle$ for the various LES flow variables indicated a fast reduction of correlation between vertical velocity fluctuations, compared to temperature and moisture fluctuations. Furthermore, depending on stability state $\langle \tilde{R}_w \rangle$ showed a faster decrease in lower and upper CBL than in the mid-CBL (Mason, 1989).

Compared to $\langle \tilde{R}_w \rangle$, the decrease of $\langle \tilde{R}_{\theta_v} \rangle$ and $\langle \tilde{R}_q \rangle$ was weaker indicating a correlation of temperature and moisture fluctuations over larger horizontal distances. This emphasised the results of Sec. 3.2.2 showing larger coherent structures of temperature and moisture in comparison to vertical velocity updraughts and downdraughts.

Integral length scales

Based on auto-covariances $\langle R_\chi(r_x) \rangle^x$ and $\langle R_\chi(r_y) \rangle^y$ of the x - and y pathways, the integral length scales $\langle \Lambda_\chi \rangle^x$ and $\langle \Lambda_\chi \rangle^y$, representative of x - and y pathways are defined as

$$\langle \Lambda_\chi \rangle^x = \frac{1}{\langle R_\chi(0) \rangle^x} \int_0^\infty \langle R_\chi(r_x) \rangle^x dr_x \quad \text{and} \quad \langle \Lambda_\chi \rangle^y = \frac{1}{\langle R_\chi(0) \rangle^y} \int_0^\infty \langle R_\chi(r_y) \rangle^y dr_y, \quad (3.18)$$

where r_x and r_y are displacements in x - and y direction, respectively. The computation of $\langle \Lambda_\chi \rangle^x$ and $\langle \Lambda_\chi \rangle^y$ was based on an approximation of $\langle R_\chi \rangle^x$ and $\langle R_\chi \rangle^y$ by third-order polynomials (Simpson's rule), required for a numerical integration scheme (Press *et al.*, 1996). Due to the convergence behaviour of the integral (Durand *et al.*, 2000), the first zero crossing of $\langle R_\chi \rangle^x$ and $\langle R_\chi \rangle^y$ was used as upper integration limit (Lenschow and Stankov, 1986; Schröter *et al.*, 2000; Durand *et al.*, 2000). The standard deviation of $\langle \Lambda_\chi \rangle^x$ and $\langle \Lambda_\chi \rangle^y$ is given as

$$\sigma_{\Lambda_\chi}^x = \left[\frac{1}{t_{\text{av}}} \sum_{t_{\text{min}}}^{t_{\text{max}}} \left\{ \Lambda_\chi^x - \langle \Lambda_\chi \rangle^x \right\}^2 \right]^{1/2}, \quad (3.19)$$

$$\sigma_{\Lambda_\chi}^y = \left[\frac{1}{t_{\text{av}}} \sum_{t_{\text{min}}}^{t_{\text{max}}} \left\{ \Lambda_\chi^y - \langle \Lambda_\chi \rangle^y \right\}^2 \right]^{1/2}, \quad (3.20)$$

where similar to the peak wavelengths, the averaging time interval t_{av} was 2 hrs starting from $t_{\text{min}} = 7$ hrs to $t_{\text{max}} = 9$ hrs integration time.

The integral length scales $\langle \Lambda_\chi \rangle^x$ and $\langle \Lambda_\chi \rangle^y$ related to different sampling pathways (Fig. 3.13) were of the same order of magnitude for vertical velocity and temperature. However, for total water content, $\langle \Lambda_q \rangle^x$ showed larger values, compared to $\langle \Lambda_q \rangle^y$. Furthermore, Fig. 3.13(a) indicated for $\langle \Lambda_w \rangle^x / \langle \Lambda_w \rangle^y$ a sensitivity on atmospheric stability. The larger difference between $\langle \Lambda_w \rangle^x$ and $\langle \Lambda_w \rangle^y$ for cases with higher stability (e.g., case B) was related to larger shear (Khanna and Brasseur, 1998)).

Based on $\langle \Lambda_\chi \rangle^x$ and $\langle \Lambda_\chi \rangle^y$, the mean integral length scale for the LES flow variables is given as

$$\langle \Lambda_\chi \rangle = \frac{1}{2} (\langle \Lambda_\chi \rangle^x + \langle \Lambda_\chi \rangle^y). \quad (3.21)$$

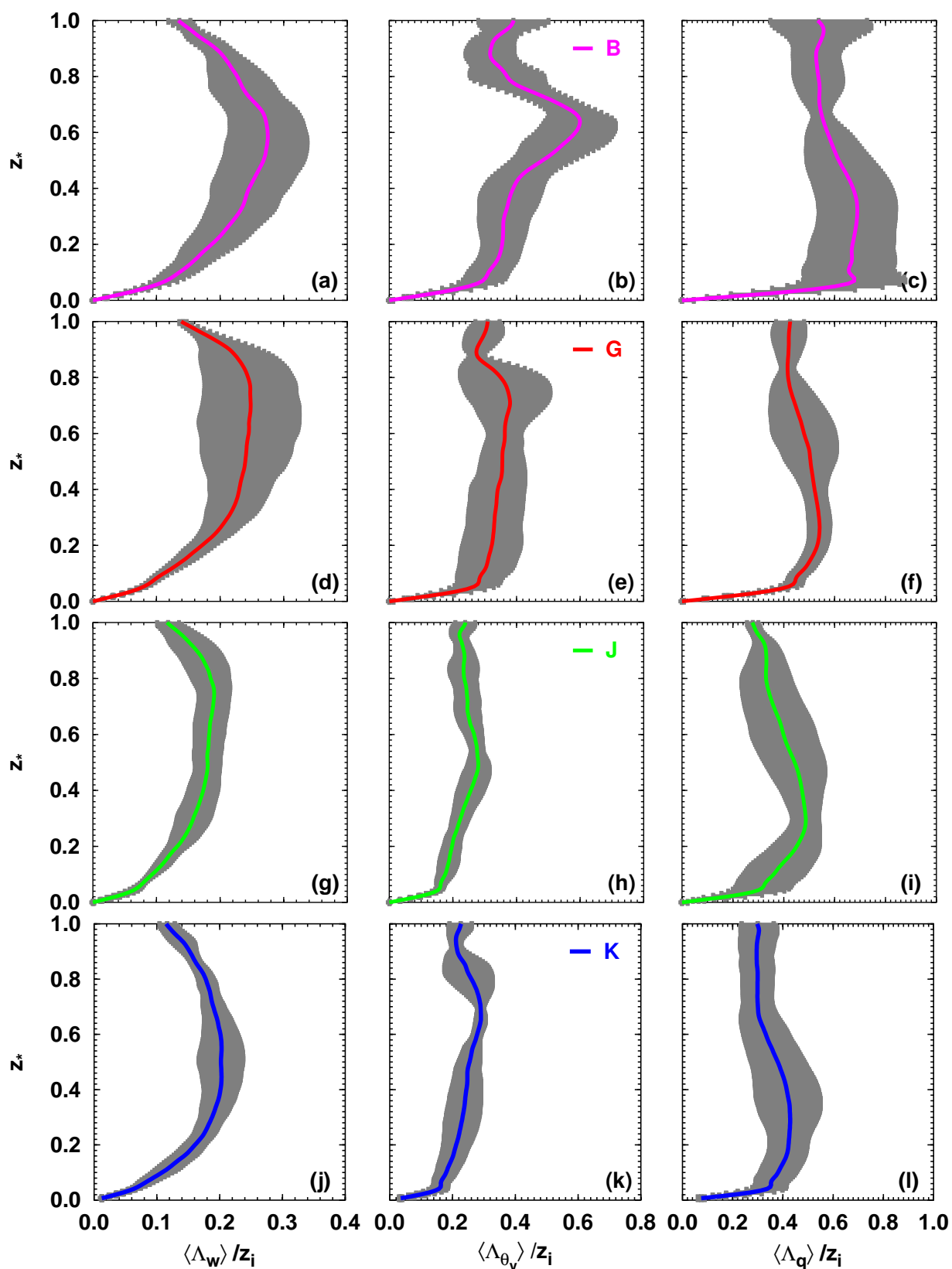


FIGURE 3.12: Horizontally averaged integral length scales $\langle \Lambda_w \rangle$, $\langle \Lambda_{\theta_v} \rangle$, and $\langle \Lambda_q \rangle$ (coloured solid lines) for (a-c) cases B, (d-f) G, (g-i) J, and (j-l) K. Grey shaded areas denote the standard deviations σ_{Λ_w} , $\sigma_{\Lambda_{\theta_v}}$, and σ_{Λ_q} .

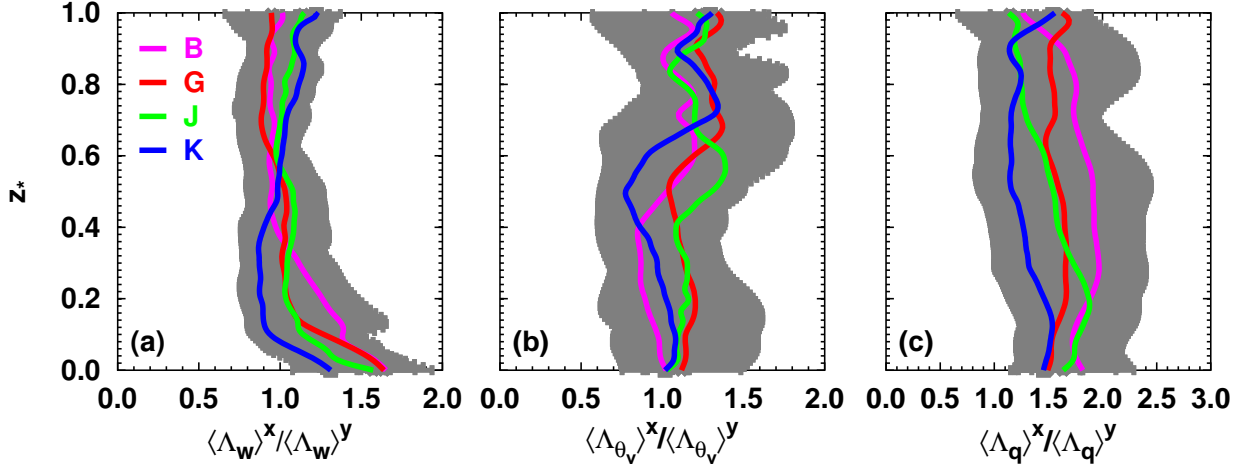


FIGURE 3.13: Ratio of integral length scales related to different sampling pathways $\langle \Lambda_\chi \rangle^x / \langle \Lambda_\chi \rangle^y$ for (a) $\chi = w$, (b) $\chi = \theta_v$, and (c) $\chi = q$ using LES cases B, G, J, and K, where grey shaded areas denote the minimum-maximum range using the corresponding standard deviations.

The standard deviation of $\langle \Lambda_\chi \rangle$ is defined as

$$\sigma_{\Lambda_\chi} = \left[\frac{1}{t_{\text{av}}} \sum_{t_{\text{min}}}^{t_{\text{max}}} \{ \Lambda_\chi - \langle \Lambda_\chi \rangle \}^2 \right]^{1/2}. \quad (3.22)$$

The vertical profiles of $\langle \Lambda_w \rangle$, $\langle \Lambda_{\theta_v} \rangle$ and $\langle \Lambda_q \rangle$ (Fig. 3.12) showed a similar shape and behaviour as the corresponding peak wavelengths (Fig. 3.10). The magnitude of the most important vertical velocity integral length scale $\langle \Lambda_w \rangle$ was approximately 1/3 of $\langle (\lambda_m)_w \rangle$ (Helmert and Hellmuth, 2000). Thus, the mean horizontal diameter of the most energy-containing updraughts and downdraughts, indicated by $\langle (\lambda_m)_w \rangle$ was in the order of the CBL depth. However, the horizontal coherence length of vertical velocity fluctuations was much smaller than the CBL depth.

Relations between characteristic turbulence length scales

The similarity between vertical profiles of peak wavelengths and integral length scales gave evidence for a relationship between both characteristic turbulence length scales, as assumed in Sec. 2.4. The ratio of $\langle (\lambda_m)_\chi \rangle$ to $\langle \Lambda_\chi \rangle$ (Fig. 3.14) remained nearly constant in bulk of the CBL. The ratio of characteristic turbulence length scales of vertical velocity indicated a decrease from surface to $z_* \sim 0.1$. Above, $\langle (\lambda_m)_w \rangle / \langle \Lambda_w \rangle$ showed values of about 5. Very unstable cases indicated somewhat larger values of $\langle (\lambda_m)_w \rangle / \langle \Lambda_w \rangle$. This behaviour was also observed for $\langle (\lambda_m)_{\theta_v} \rangle / \langle \Lambda_{\theta_v} \rangle$ showing values from about 3 to 5 depending on stability state. A dependence on atmospheric stability was not observed for $\langle (\lambda_m)_q \rangle / \langle \Lambda_q \rangle$ showing values of about 4.

The resulting relations between characteristic turbulence length scales of the energy-containing range agreed well with theoretical considerations suggesting $\langle (\lambda_m)_\chi \rangle / \langle \Lambda_\chi \rangle = 6.4$ (Kaimal and Finnigan, 1994) as well as atmospheric measurements (Lenschow and Stankov, 1986; Durand *et al.*, 2000) showing values from $\langle (\lambda_m)_\chi \rangle / \langle \Lambda_\chi \rangle \sim 3-9$.

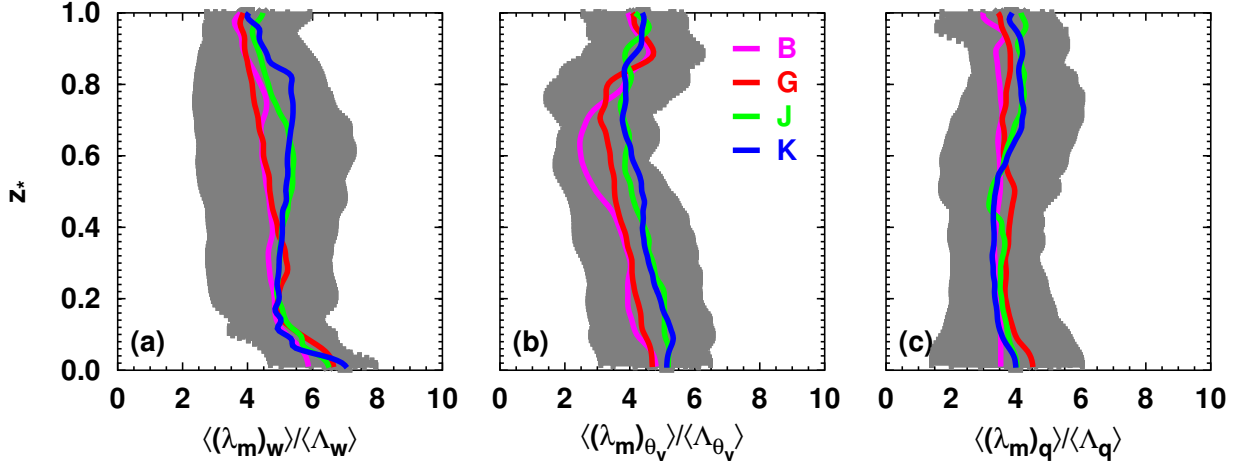


FIGURE 3.14: Ratio of mean peak wavelength to integral length scale $\langle(\lambda_m)_\chi\rangle/\langle\Lambda_\chi\rangle$ for (a) $\chi = w$, (b) $\chi = \theta_v$, and (c) $\chi = q$ using LES cases B, G, J, and K, where grey shaded areas denote the minimum-maximum range using the corresponding standard deviations.

3.3 Verification of large-eddy simulation results

LES derived integral length scales and peak wavelengths were compared with results from numerical simulations of clear-convective boundary layers with shear, performed by Khanna and Brasseur (1998) based on the LES model of Moeng (1984) as well as with LES results from Graf and Schumann (1991) based on the LES model of Schmidt and Schumann (1989). Furthermore, comparisons of $\langle\Lambda_w\rangle$ and $\langle(\lambda_m)_w\rangle$ with results from atmospheric measurements of marine and continental CBLs (Lenschow and Stankov, 1986; Lambert and Durand, 1999; Durand *et al.*, 2000; Caughey and Palmer, 1979) as well as from laboratory experiments of horizontally evolving CBLs with shear (Kaiser, 1996; Kaiser and Fedorovich, 1998) were performed.

3.3.1 Verification against numerical simulations

The comparison of the LES derived turbulent mixing length scales with results from numerical simulations, reported in the literature is based on five cases of the verification database (see Tab. 3.3). Results of Khanna and Brasseur (1998), obtained for clear-air CBL with $-z_i/L_{MO} \sim 8$ were compared with simulation cases I to III, comparable in domain size, surface heat flux, and geostrophic wind. Furthermore, a comparison with results of case D, similar in atmospheric stability state, but different in initial and boundary conditions was performed.

The simulation case B was used for comparison with results from Graf and Schumann (1991). Furthermore, the sensitivity of $\langle\Lambda_w\rangle$ against changes in horizontal grid resolution using case III as well as against changes in inversion strength above z_i using case II was examined.

Compared to results from Khanna and Brasseur (1998), the CBL scaling parameter of cases I to III and case D showed a good agreement for u_* , w_* , θ_* . However, z_i and L_{MO} of case D showed somewhat larger values (Tab. 3.3) due to a different initial temperature profile (see Tab. 3.1).

TABLE 3.3: Boundary layer properties based on LES data of Graf and Schumann (1991) (GS91), Khanna and Brasseur (1998) (KB98), and LES cases I to III, D and B using varying domain size L_x, L_y, L_z , grid resolutions $\Delta x, \Delta y, \Delta z$, and potential temperature lapse rate in the entrainment zone range above CBL top $\Gamma_\theta^> = \Delta\theta/\Delta z$.

Parameter	GS91	KB98	I	II	III	D	B
$-z_i/L_{\text{MO}}$		7.91	8.91	8.20	9.13	9.16	
L_x (km)	10	5	5	5	5	6.4	6.4
L_y (km)	10	5	5	5	5	6.4	6.4
L_z (km)	2.5	2	2	2	2	4.4	4.4
Δx (m)	100	39	78	78	156	100	100
Δy (m)	100	39	78	78	156	100	100
Δz (m)	100	16	18	18	18	40	40
$\overline{(w'\theta')}_s$ (K m s ⁻¹)	0.08	0.24	0.24	0.24	0.24	0.2	0.05
\bar{u}_g (m s ⁻¹)	2.8	15	15	15	15	15	10
\bar{v}_g (m s ⁻¹)	-0.5	0	0	0	0	0	0
u_* (m s ⁻¹)		0.74	0.71	0.71	0.70	0.73	
w_* (m s ⁻¹)	1.28	2.0	2.0	1.94	2.0	2.1	1.23
θ_* (K)	0.06	0.12	0.12	0.12	0.12	0.10	0.047
t_* (s)	700	510	535	508	530	680	834
z_i (m)	900	1020	1070	985	1060	1400	1026
$-L_{\text{MO}}$ (m)		129	120	120	116	153	
$\Gamma_\theta^>$ (K m ⁻¹)			0.0234	0.0300	0.0231	0.0168	

Compared to cases I, III, and case D, the larger inversion strength of case II led to an increased lapse rate of θ in the entrainment zone range. LES of larger domain size resolves also mesoscale fluctuations affecting entrainment processes and reducing $\Gamma_\theta^>$ (Jonker *et al.*, 1997, 1999). Thus, the smaller $\Gamma_\theta^>$ of cases III and D, compared to case I was related to lower spatial resolution and larger domain size, respectively (Stevens *et al.*, 2002). Compared to Graf and Schumann (1991) the determined CBL scaling parameter of case B indicated a good agreement.

As illustrated in Fig. 3.15, $\langle\Lambda_w\rangle$ of cases I to III, and case D showed a similar behaviour as $\langle\Lambda_w\rangle$ of Khanna and Brasseur (1998). They agreed in their linear increase of $\langle\Lambda_w\rangle$ below $z_* = 0.1$, showed their maximum in mid-CBL and a similar decrease above $z_* = 0.7$. The very strong capping inversion in the LES of Khanna and Brasseur (1998) accounted for the differences of $\langle\Lambda_w\rangle$ to the LES cases in the upper CBL. The lower horizontal grid resolution of case III, compared to case I resulted in somewhat larger $\langle\Lambda_w\rangle$ (Fig. 3.15(c)). Small differences in Γ_θ had only minor impact on $\langle\Lambda_w\rangle$.

The peak wavelength determined by Graf and Schumann (1991) at various CBL heights was

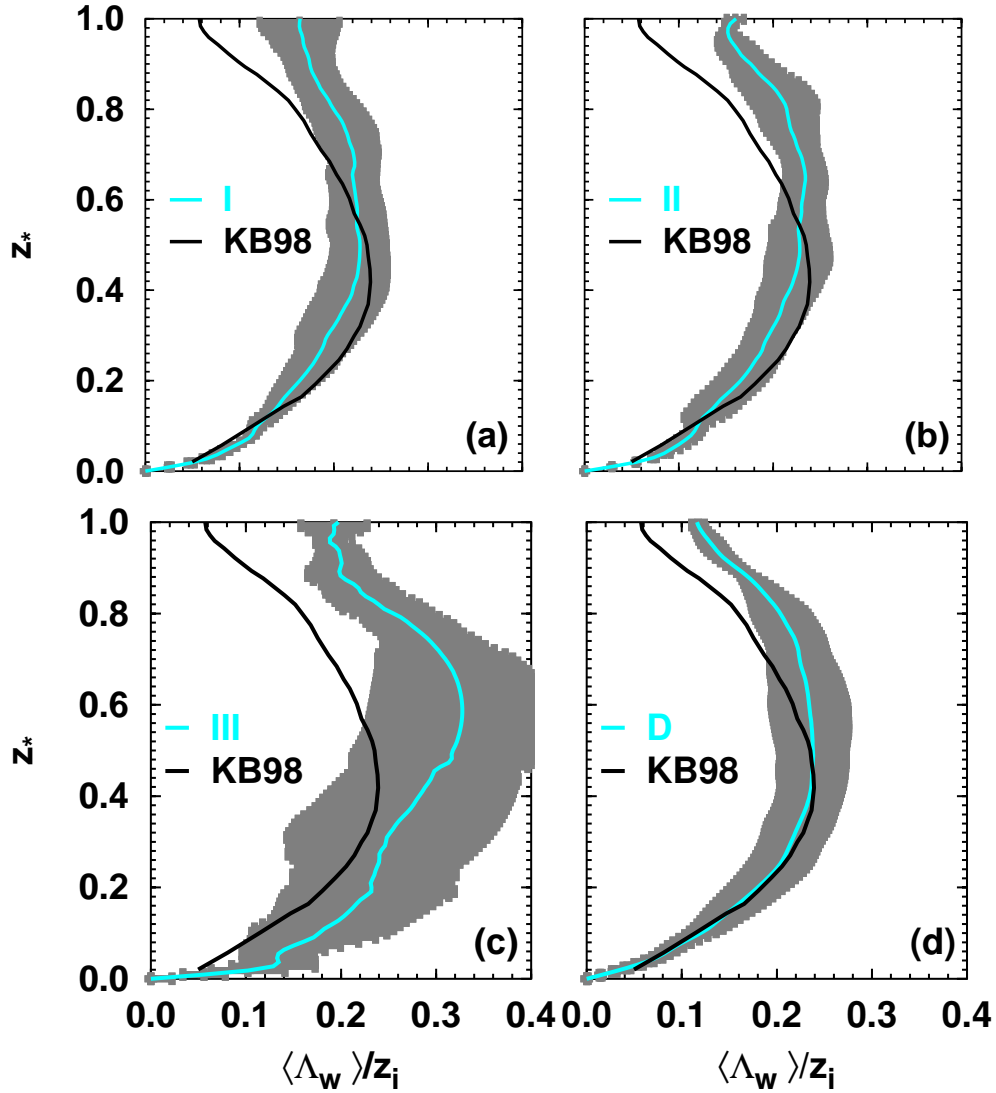


FIGURE 3.15: Integral length scales based on LES data of Khanna and Brasseur (1998) (KB98) and LES cases (a) I, (b) II, (c) III, and (d) case D.

in good agreement with $\langle (\lambda_m)_w \rangle$ of case B (Fig. 3.16) assuming a maximum in the mid-CBL and decreasing above $z_* = 0.7$. Differences of $\langle (\lambda_m)_w \rangle$ between case B and Graf and Schumann (1991) occurring in the lower and upper CBL were related to different atmospheric stability states of the simulated CBLs.

3.3.2 Verification against atmospheric measurements

LES derived peak wavelengths and integral length scales of case IV were compared with aircraft measurements in marine CBLs (MCBL), obtained during the SEMAPHORE campaign (Lambert and Durand, 1999; Lambert *et al.*, 1999; Durand *et al.*, 2000). Mean flow variables and CBL

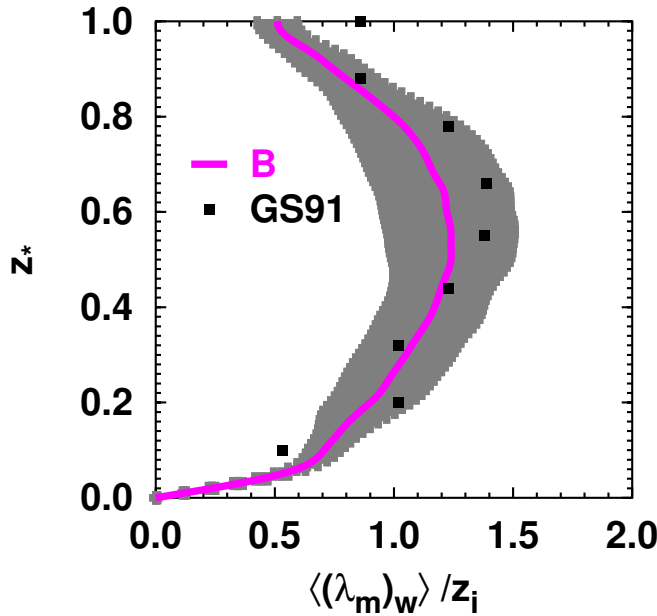


FIGURE 3.16: Peak wavelength based on LES of Graf and Schumann (1991) (GS91) and LES case B.

scaling parameter, derived from case IV after 9 hrs integration time (Tab. 3.4) agreed well with measurement data of two representative days (05.11.1993 (OBS I) and the 06.11.1993 (OBS II)) of the SEMAPHORE campaign (Lambert and Durand, 1999). The marine boundary layer of these observation days was related to a strato-cumulus topped CBL. Since buoyancy in the MCBL was primarily driven by a strong latent heat flux, only weak entrainment was observed (Lambert and Durand, 1999).

The measurements of OBS I and OBS II were carried out from 15:54 to 18:26 UTC and from 16:12 to 18:13 UTC, respectively (Lambert and Durand, 1999). The measurement data of OBS II (Tab. 3.4) were used to initialise the LES case IV. The measurement site was in a subregion of the open ocean with homogeneous conditions over a horizontal distance of some hundred kilometres. Thus, the chosen boundary conditions of MCBLs were in good agreement with periodic boundary conditions and horizontal homogeneity, assumed in LES.

The structure of the observed MCBL was well captured by the simulation (Fig. 3.17). In agreement with the observation, case IV clearly showed a mixed layer with $z_i \sim 1000$ m, an entrainment layer with $\Delta z_i \sim 300$ m as well as a cloud layer. The measured and simulated final mean potential temperature profiles (Fig. 3.17(a)) were in good agreement within the mixed layer, where the difference between observation and simulation was in the order of 2 K (Fig. 3.17(a)). However, the temperature jump at the inversion $z_T \sim 1800$ m was somewhat overpredicted by the LES compared to the measurements. The overall agreement between LES and measurements of total water content (Fig. 3.17(b)) was very good (difference $\Delta q \sim 1 \text{ g kg}^{-1}$ within the mixed layer). The final mean LES profile of q showed, compared to the initial profile a mixed layer drying. The measured sharp decrease of q above z_i was well reproduced by the simulation.

TABLE 3.4: Marine boundary layer properties based on observations during the SEMAPHORE campaign (Lambert and Durand, 1999; Lambert *et al.*, 1999; Durand *et al.*, 2000) and LES case IV, where U is the wind speed, α is the wind direction, p is the pressure, and z_T is the height of the inversion above cloud top.

Parameter	OBS I	OBS II	IV
U (m s ⁻¹)	7.75	8	7.23
α (°)	28	38	33
θ (K)	288.36	288.56	286.52
q (g kg ⁻¹)	6.1	6.73	5.40
p (hPa)	1028	1027	1027
$\overline{(w'\theta')}_s$ (K m s ⁻¹)	0.012	0.017	0.017
$\overline{(w'q')}_s$ (m s ⁻¹ g kg ⁻¹)	0.057	0.038	0.038
z_i (m)	861	965	980
z_T (m)	1766	1633	1760
u_* (m s ⁻¹)	0.26	0.30	0.28
$-L_{MO}$ (m)	58	77	67.7
w_* (m s ⁻¹)	0.87	0.92	0.92
θ_* (K)	0.014	0.019	0.026
q_* (g kg ⁻¹)	0.066	0.042	0.041

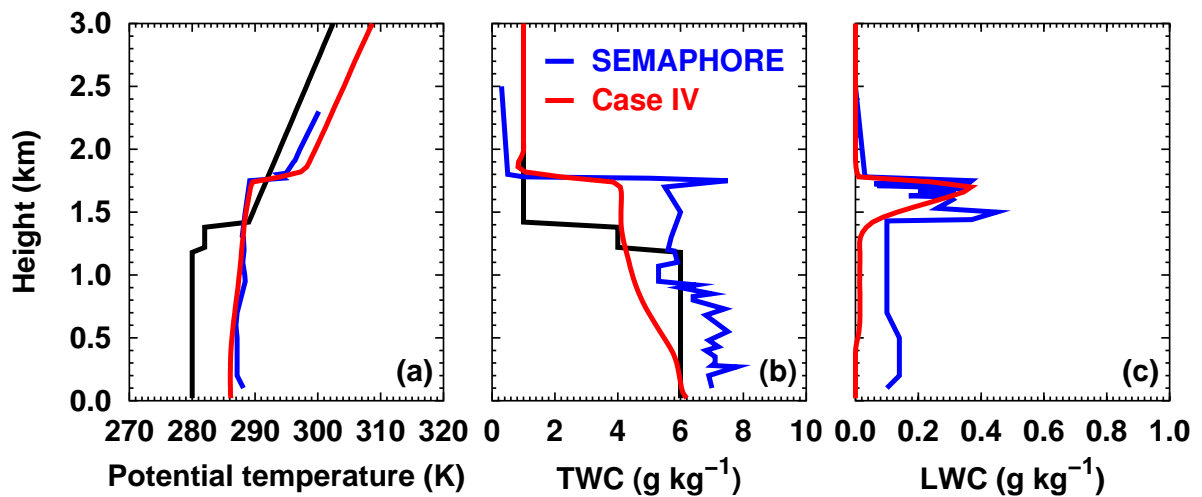


FIGURE 3.17: Mean flow variables of SEMAPHORE and LES case IV, where (a) shows the potential temperature $\langle\theta\rangle$, (b) shows the total water content (TWC) $\langle\bar{q}\rangle$, and (c) shows the liquid water content (LWC) $\langle\bar{q}_l\rangle$. Initial soundings of LES are denoted by black solid lines.

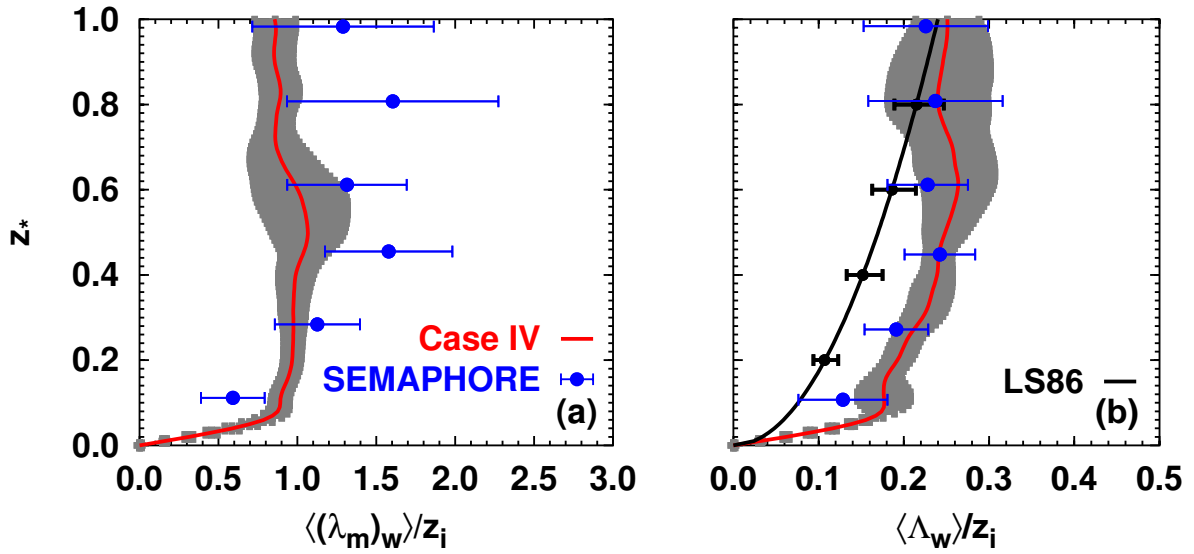


FIGURE 3.18: Comparison of (a) peak wavelength and (b) integral length scale based on observations (OBS) during SEMAPHORE (Durand *et al.*, 2000), integral length scale approximation after Lenschow and Stankov (1986) (LS86), and LES case IV.

The liquid water content, derived from measurements showed somewhat larger values below $z \sim 1400$ m than the results from case IV (Fig. 3.17(c)). However, the agreement between measured and simulated cloud base ($z \sim 1400$ m), cloud top ($z \sim 1800$ m), and q_l within the cloud layer was very good.

Averaged measured peak wavelengths and integral length scales of vertical velocity from the SEMAPHORE campaign (Durand *et al.*, 2000) were in acceptable agreement with $\langle(\lambda_m)_w\rangle$ and in good agreement with $\langle\Lambda_w\rangle$ of case IV (Fig. 3.18). Due to weak entrainment processes in the MCBL, $\langle(\lambda_m)_w\rangle$ and $\langle\Lambda_w\rangle$ indicated only a weak decrease to the CBL top.

Whereas the LES derived $\langle(\lambda_m)_w\rangle$ showed a maximum of standard deviation in the mid-MCBL, the standard deviations of the measured $\langle(\lambda_m)_w\rangle$ as well as of measured and LES derived $\langle\Lambda_w\rangle$ were in similar order of magnitude. The measurements indicated an increased scatter in the upper MCBL, since turbulence originated at MCBL top is much more inhomogeneous (Lambert and Durand, 1999). This behaviour was also observed for the approximation of $\langle\Lambda_w\rangle$ (Eq. (2.58)), which is based on aircraft measurements in marine and continental CBLs (Lenschow and Stankov, 1986). Above $z_* = 0.6$, this approximation of $\langle\Lambda_w\rangle$ (Lenschow and Stankov, 1986) indicated a good agreement with results from case IV and measurements of Durand *et al.* (2000).

The peak wavelengths of vertical velocity (Caughey and Palmer, 1979), measured in continental CBL showed a much more pronounced maximum at mid-CBL than in the marine CBL. However, the largest scatter of measurement data occurred also in the mid-CBL (Fig. 3.19). A good agreement of the measured peak wavelength with $\langle(\lambda_m)_w\rangle$, derived from LES case B was observed. The measurement data indicated only just below CBL top somewhat smaller values for $\langle(\lambda_m)_w\rangle$, compared to case B and LES data of Graf and Schumann (1991). This difference was related to a very strong capping inversion (Kaiser and Fedorovich, 1998).

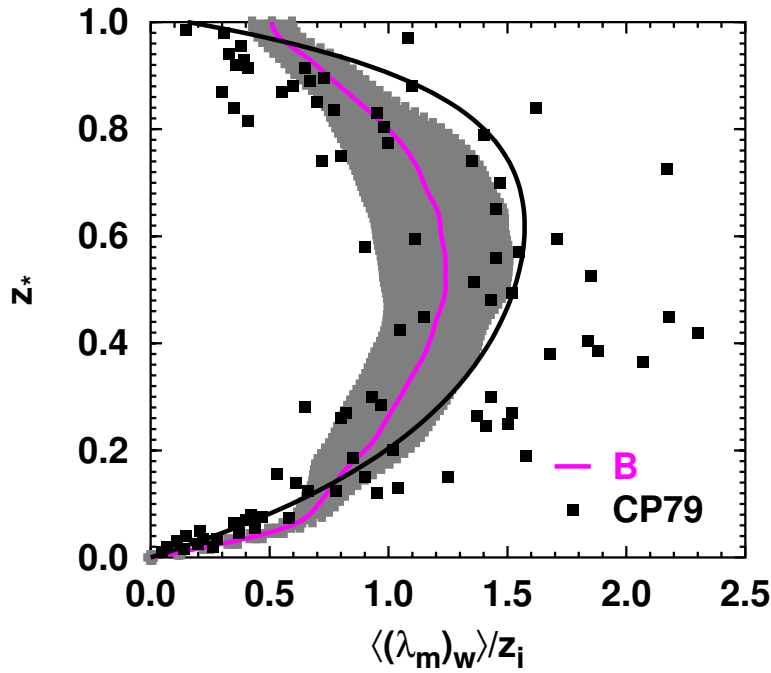


FIGURE 3.19: Peak wavelengths based on measurements of Caughey and Palmer (1979) and LES case B. The black solid line is a fit approximation of the measurement data (Caughey and Palmer, 1979).

TABLE 3.5: Boundary layer properties based on wind tunnel measurements (Kaiser, 1996; Kaiser and Fedorovich, 1998) for sections x_3 to x_5 of varying distance x from the intake of the wind tunnel and LES cases B, C, and D.

Parameter	x_3	B	x_4	C	x_5	D
$-z_i/L_{MO}$	5.0	5.9	7.3	7.1	9.3	9.2
x (m)	3.98		5.63		7.28	
$\overline{(w'\theta')_s}$ (K m s $^{-1}$)	0.63	0.05	0.8	0.2	0.88	0.2
z_i (m)	0.300	1026.0	0.350	1600.0	0.400	1400.0
u_* (m s $^{-1}$)	0.0701	0.50	0.0703	0.86	0.0693	0.73
w_* (m s $^{-1}$)	0.163	1.23	0.185	2.73	0.198	2.06
θ_* (K)	3.86	0.047	4.32	0.084	4.45	0.097

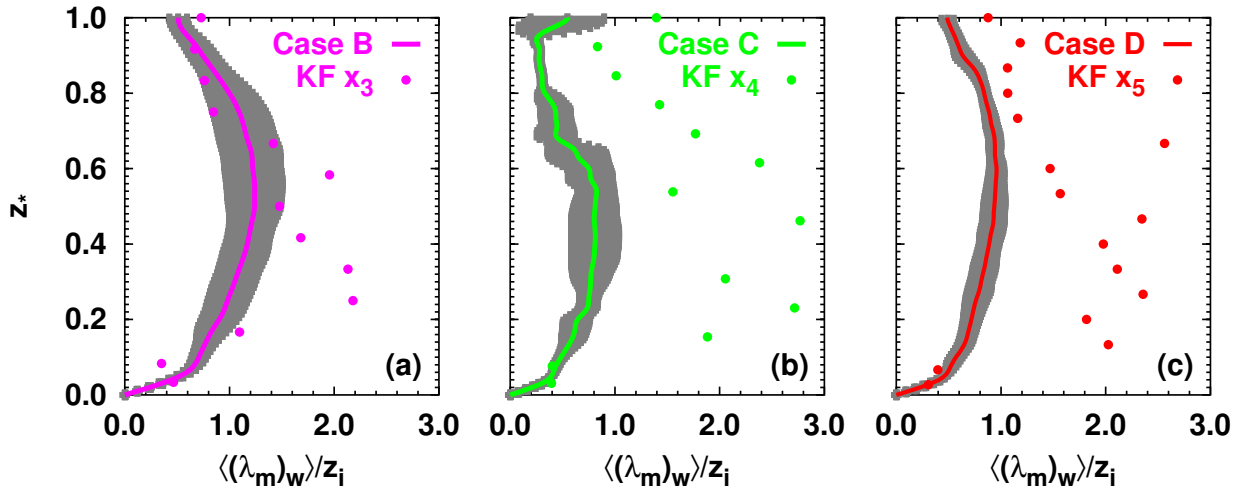


FIGURE 3.20: Peak wavelengths based on wind tunnel measurements (KF) (Kaiser, 1996; Kaiser and Fedorovich, 1998) in sections x_3 to x_5 and LES cases B, C, and D.

3.3.3 Verification against laboratory experiments

Vertical velocity peak wavelength, derived from LES cases B, C, and D (Tab. 3.5) were compared with wind tunnel measurements of $\langle(\lambda_m)_w\rangle$ in horizontally evolving CBLs (Kaiser, 1996; Kaiser and Fedorovich, 1998). In these laboratory experiments, CBLs of similar stability state were examined.

As seen from Fig. 3.20, in dependence on stability state of the simulated CBLs, $\langle(\lambda_m)_w\rangle$ derived from LES showed different values. The measured peak wavelength showed a dependence on the measurement distance x . Since the wind tunnel measurements are related to horizontal evolving CBLs, different measurement distances from the intake of the wind tunnel are related to different stability states.

Near the surface, the simulations agreed with the measurements. However, at mid-CBL the measurements indicated larger $\langle(\lambda_m)_w\rangle$ compared to the LES. These differences were more pronounced with increasing distance x from the intake of the wind tunnel, related to developing role structures within the wind tunnel CBL (Kaiser, 1996). These role structures with wavelengths of ~ 2 km were also observed in LES (see Sec. 3.2.2). However, in contrast to the wind tunnel measurements, role structures within the simulated CBLs were not associated with the most energy-containing motions. In the upper CBL, $\langle(\lambda_m)_w\rangle$ derived from LES cases B and D were in good agreement with the wind tunnel measurements at x_3 and x_5 , respectively. However, large deviations in the upper CBL were found between $\langle(\lambda_m)_w\rangle$ derived from LES case C and wind tunnel measurements at x_4 . These differences were related to differences in entrainment strength between case C and the wind tunnel CBL, due the strong bottom-up forcing in the wind tunnel (Kaiser and Fedorovich, 1998).

3.4 Turbulent mixing length formulation based on characteristic turbulence length scales

3.4.1 Approximation of peak wavelength and integral length scale

Based on the LES database, approximations of peak wavelength and integral length scale were developed and tested using a statistical analysis.

According to Caughey and Palmer (1979) (see Eq. (2.53) and Fig. 3.19), the LES derived peak wavelength $\langle(\lambda_m)_w\rangle$ was approximated as

$$\langle(\lambda_m)_w\rangle = \begin{cases} a_0 z_*, & \text{for } z_* < z_{*0} \\ a_1 z_i (1 - e^{-a_2 z_*} - a_3 e^{a_4 z_*}), & \text{for } z_{*0} \leq z_* \leq 1, \end{cases} \quad (3.23)$$

where $z_* = z/z_i$ is the normalised altitude, $z_{*0} \sim 0.1$, and $a_i = (a_0, a_1, a_2, a_3, a_4)$ are stability dependent parameters.

Existing integral length scale approximations (Lenschow and Stankov, 1986) were used to develop a new approximation of $\langle\Lambda_w\rangle$ (Helmert and Hellmuth, 2003) taking into account the decrease of $\langle\Lambda_w\rangle$ in the upper CBL. In this new formulation, $\langle\Lambda_w\rangle$ is given as

$$\langle\Lambda_w\rangle = \begin{cases} a_0 z_*, & \text{for } z_* < z_{*0} \\ a_1 (z_*)^{1/2} (1 - a_2 z_*) (1 + a_3 z_*)^2, & \text{for } z_{*0} \leq z_* \leq 1 \end{cases} \quad (3.24)$$

using stability dependent parameters $a_i = (a_0, a_1, a_2, a_3)$.

The peak wavelength and integral length scale of scalars ϕ using $\phi = (\theta_v, q)$ were approximated as

$$\langle(\lambda_m)_\phi\rangle = \begin{cases} a_0 z_*, & \text{for } z_* < z_{*0} \\ a_1, & \text{for } z_{*0} \leq z_* \leq 1 \end{cases} \quad (3.25)$$

$$\langle\Lambda_\phi\rangle = \begin{cases} a_0 z_*, & \text{for } z_* < z_{*0} \\ a_1, & \text{for } z_{*0} \leq z_* \leq 1, \end{cases} \quad (3.26)$$

where a_0 and a_1 are stability dependent parameters.

The parameters a_i in the approximations of $\langle(\lambda_m)_w\rangle$ and $\langle\Lambda_w\rangle$ (Eqs. (3.23)-(3.26)) were derived from the the LES database using non-linear least square fitting (Marquardt, 1963). This method use an adjusting of the parameters $a_i, i = 0, \dots, M-1$ (Williams and Kelly, 1995) to minimise the parameter χ_r^2 , given as

$$\chi_r^2 = \frac{1}{n_D} \sum_{i=1}^N \left(\frac{\ell_{k_i} - \ell_k(z_{*i}; a_0 \dots a_{M-1})}{\sigma_{\ell_{k_i}}} \right)^2, \quad (3.27)$$

where $n_D = N - N_a$ is the number of degrees of freedom, $\ell_k = (\langle(\lambda_m)_w\rangle, \langle\Lambda_w\rangle)$ is the characteristic turbulence length scale under consideration, N is the number of data points, $N_a = M-1$ is the number of parameters a_i , and σ_{ℓ_k} is the standard deviation of ℓ_k .

The probability distribution for different values of χ_r^2 at its minimum is given by the chi-square distribution for n_D degrees of freedom (Press *et al.*, 1996). The probability Q that the chi-square exceeds a particular value χ_r^2 is given as

$$Q(c, x) = \frac{1}{\Gamma(c)} \int_x^{\infty} e^{-t} t^{c-1} dt, \quad (3.28)$$

where $x = 0.5\chi_r^2$ and $\Gamma(c)$ is the gamma function of $c = 0.5n_D$. In this work, the probability $Q(c, x)$ was used as a quantitative measure of the goodness-of-fit (Press *et al.*, 1996).

The look-up tables of parameters a_i , $i = 0, \dots, N_a$, for peak wavelengths and integral length scales of the LES flow variables are given in Tab A.1-A.6. The different values of a_i for the various simulations reflected the inherent dependence of characteristic turbulence length scales on atmospheric stability. Although a fit parameter $Q \sim 1$ was found for the bulk of the simulations, in some cases Q is remarkable low. Whereas a large standard deviation of $\langle(\lambda_m)_\chi\rangle$ and $\langle\Lambda_\chi\rangle$ is responsible for the large values of Q , the low values of Q could be due to a non-normal distribution of the standard deviation σ_{ℓ_k} (Press *et al.*, 1996). However, compared to the approximation of $\langle(\lambda_m)_w\rangle$, the approximation of $\langle\Lambda_w\rangle$ showed larger values for Q indicating a higher statistical significance of Eq. (3.24).

The general behaviour of the LES derived $\langle(\lambda_m)_\chi\rangle$ and $\langle\Lambda_\chi\rangle$ was well captured by the approximations (Eqs. (3.23)-(3.26)) (see Fig. B.1 and Fig. B.2 in the appendix). Whereas the assumption of constant $\langle(\lambda_m)_\phi\rangle$ and $\langle\Lambda_\phi\rangle$ seemed not in all cases to be the best approximation, the new approximation for $\langle\Lambda_w\rangle$ (Eq. (3.24)) yielded a very good agreement with the LES results, compared to previous approximations (Lenschow and Stankov, 1986) (Fig. 3.18).

3.4.2 Verification of the new turbulent mixing length formulation

To improve the approximation of the turbulent mixing length primarily at CBL top, which is essential for obtaining proper entrainment fluxes (Abdalla and McFarlane, 1997; Cuijpers and Holtslag, 1998) a new formulation for the turbulent mixing length in unstable conditions was developed (Helmert and Hellmuth, 2002). In this formulation, the turbulent mixing length was related to the LES derived approximation of vertical velocity integral length scale $\langle\Lambda_w\rangle$ (Eq. (3.24)) as a characteristic turbulence length scale of the energy-containing range. Here, the dependence on atmospheric stability was provided by the look-up table of parameters a_i (Tab. A.2), derived from the non-linear least square fitting (Sec. 3.4.1).

After implementation of this approach in a present model, the application of this model as an replacement for the master length scale (Blackadar, 1962) in the Mellor-Yamada scheme Level 2.5 (see Sec. 2.2) was examined. The consequences of this modification of the turbulent mixing length formulation for the parameterisation of turbulent diffusion are illustrated by a comparison,

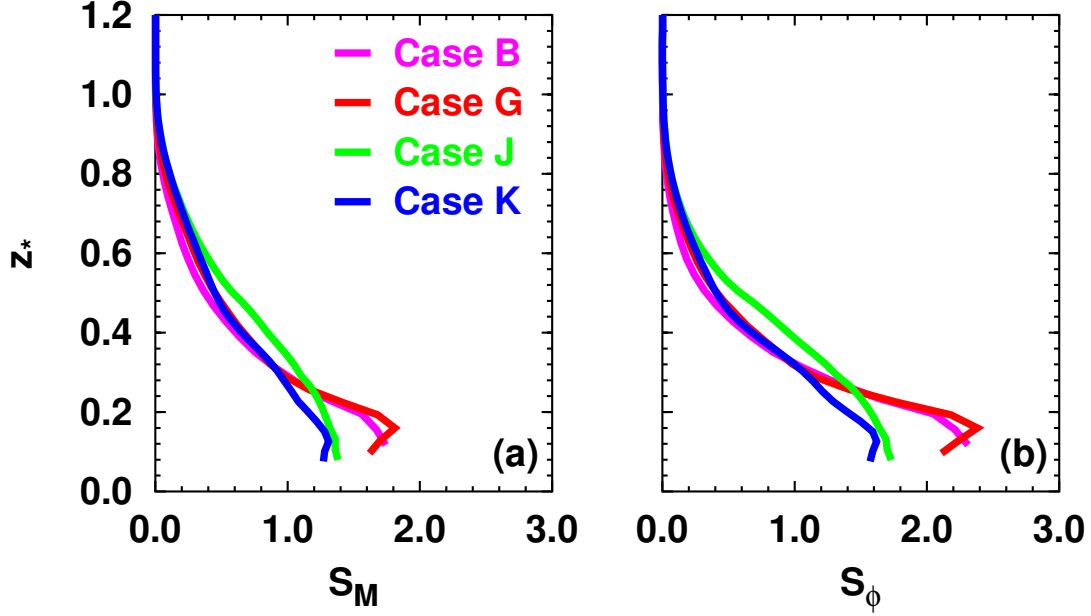


FIGURE 3.21: Vertical profiles of the stability functions of (a) momentum and (b) of scalars

given as

Mellor-Yamada	↔	Present Model
$K_M = S_M l E, \quad K_\phi = S_\phi l E$	↔	$K_M = K_\phi = \ell_k E,$
$S_M l, \quad S_\phi l$	↔	$\ell_k(-z_i/L_{MO}) = 0.1 \cdot \langle \Lambda_w \rangle,$
$l = \left(\frac{1}{\kappa z} + \frac{1}{l_0} \right)^{-1}$	↔	$\langle \Lambda_w \rangle : \text{Eq. (3.24)}$

The resulting implications on parameterisation of eddy diffusivity, turbulent fluxes, and variances in MY25 (see Sec. 2.2) were examined. Thus, LES derived turbulent fluxes and variances of the simulated CBLs of various stability state (cases B, G, J, and K) were used as reference data in a verification of the present model against results of MY25 with master length scale. To focus on the impact of the turbulent mixing length, both models used the same LES derived turbulent kinetic energy and mean vertical profiles of horizontal wind components and liquid water potential temperature.

These mean vertical profiles were used to determine the stability functions S_M , S_ϕ of momentum and scalars, respectively (Eqs. (2.12)-(2.20)), required in the master length scale approach of MY25 (Fig. 3.21). The observed decrease of S_M and S_ϕ from surface to the CBL top (Nakanishi, 2001) indicated a varying vertical stratification throughout the CBL. As seen from Fig. 3.21, both stability functions vanished in the entrainment zone range ($0.8 \leq z_* \leq 1.2$). However, this leads to vanishing eddy diffusivities (Eqs. (2.8)-(2.9)) in this range. Thus, the observed behaviour of S_M and S_ϕ emphasised the deficiencies of the master length scale approach in the entrainment

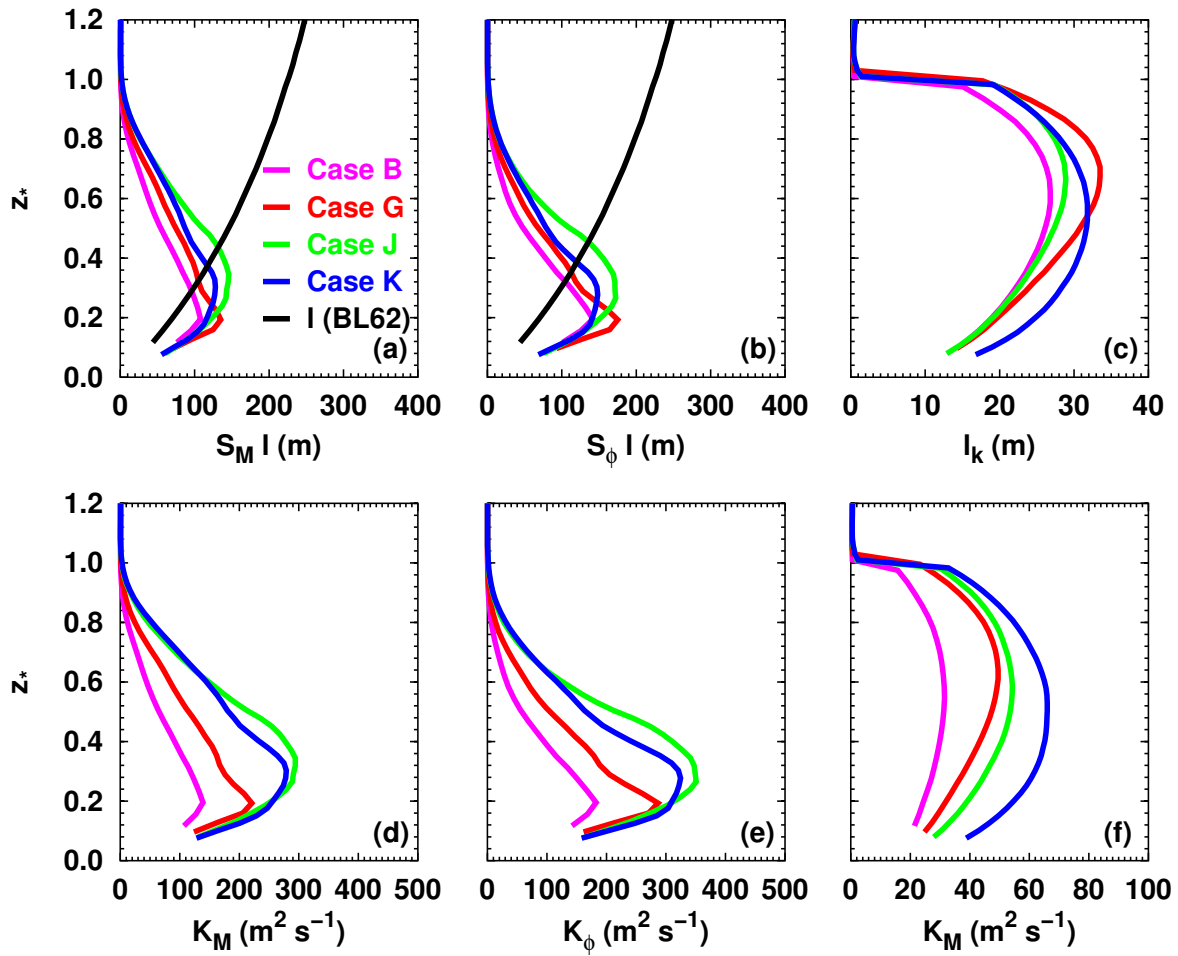


FIGURE 3.22: Vertical profiles of turbulent mixing length based on MY25 (a) for momentum and (b) for scalars, where the black solid line denotes the master length scale approximation of Blackadar (1962), (c) turbulent mixing length derived from the present model, (d) eddy diffusivity coefficients based on MY25 for momentum and (e) for scalars, (f) eddy diffusivity coefficient based on the present model of turbulent mixing length.

zone of CBLs. Furthermore, a pronounced dependence of S_M and S_ϕ on the different stability state of the LES was only visible in the lower CBL.

Consequently, the resulting turbulent mixing lengths $S_M l$ and $S_\phi l$ of the master length scale approach showed a maximum in the lower and mid-CBL but decreased below CBL top (Fig. 3.22(a, b)). However, this decrease indicated a vanishing turbulent mixing in the entrainment zone, in contrast to atmospheric measurements and theoretical considerations. Compared to the master length scale approach, the approximation of the turbulent mixing length based on stability dependent integral length scales showed non-vanishing values throughout the whole CBL (Fig. 3.22(c)). A maximum of the turbulent mixing length in the upper CBL was indicated by l_k of the present model. Above z_i both models were identical.

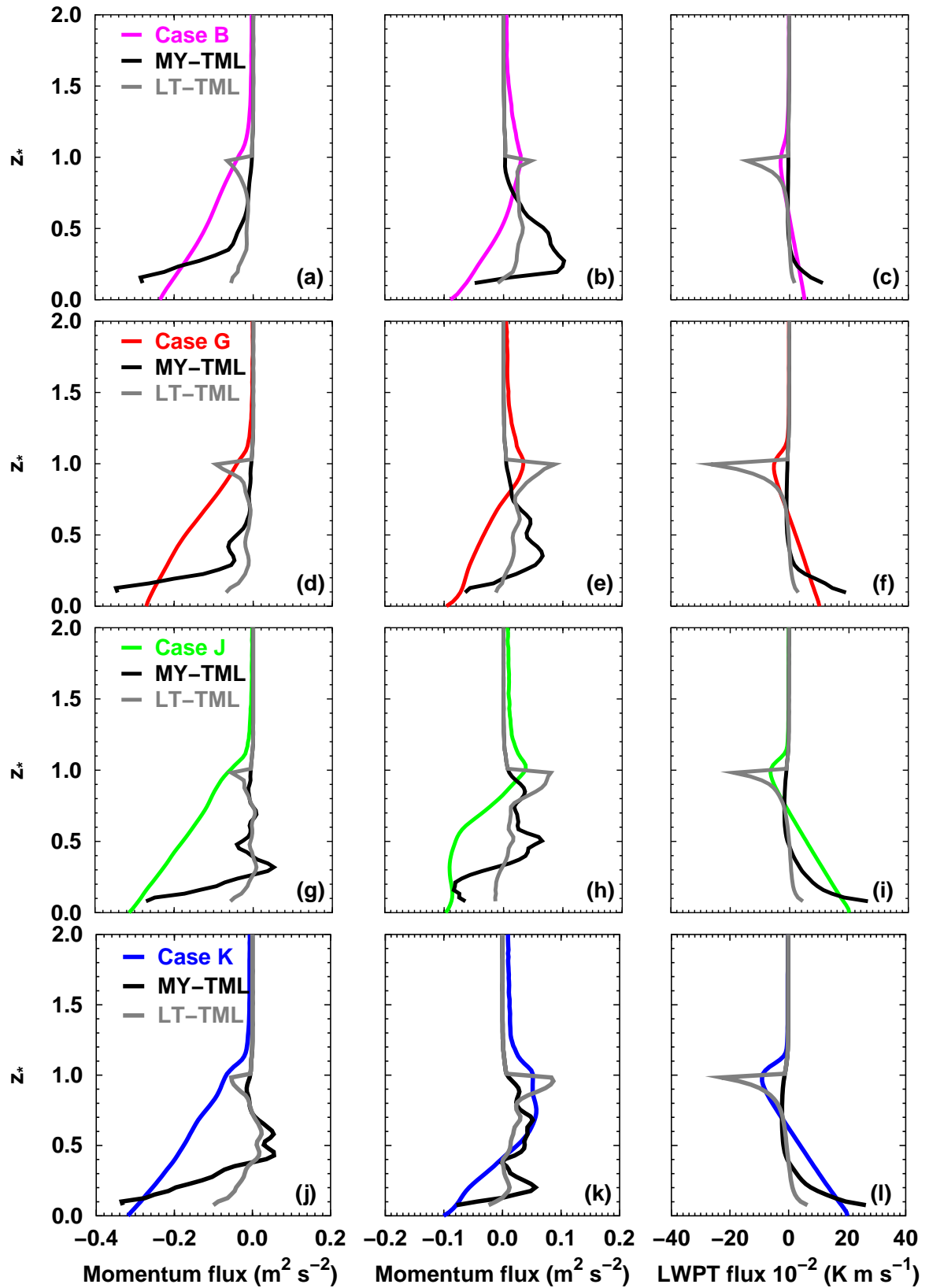


FIGURE 3.23: Turbulent fluxes, derived from LES cases, based on Mellor-Yamada model (MY-TML), and based on present model containing LES-derived look-up table of turbulent mixing length (LT-TML). (a, d, g, j) zonal momentum flux $\langle u'w' \rangle$, (b, e, h, k) meridional momentum flux $\langle v'w' \rangle$, and (c, f, i, l) liquid water potential temperature heat flux $\langle w'\theta_l' \rangle$.

As seen from Fig. 3.22, the magnitude of eddy diffusivity increased with decreasing stability from case B to case K in both models. However, due to the observed deficiencies of the master length scale approach, the eddy diffusivity coefficients of MY25 (Fig. 3.22(d,e)) indicated only in the lower and mid-CBL a strong turbulent diffusion. Above, K_M and K_ϕ of MY25 showed a strong decrease to zero indicating a decrease of turbulent diffusion in the entrainment zone. The eddy diffusivity, derived from the present model of turbulent mixing length indicated a maximum of turbulent mixing at mid-CBL and only a small decrease just below CBL top (Fig. 3.22(f)).

The parameterised turbulent fluxes and variances based on the down-gradient approach but different models of turbulent mixing length scale (MY25, present model) were compared with simulated turbulent fluxes and variances from the LES (Figs. 3.23-3.24). Both models showed deviations to the zonal momentum flux $\langle u'w' \rangle$, derived from LES (Fig. 3.23(a, d, g, j)). Although with decreasing of stability, the MY25 showed a somewhat better agreement with LES in the near surface range, it indicated a vanishing of $\langle u'w' \rangle$ below CBL top. Here, $\langle u'w' \rangle$, derived from the present model indicated a good agreement with the LES results.

A similar behaviour was found for the meridional momentum flux $\langle v'w' \rangle$ (Fig. 3.23(b, e, h, k)). MY25 showed a good agreement with LES results in the near surface range but failed to predict the maximum of $\langle v'w' \rangle$ at CBL top. The present model showed an improved approximation of this maximum and indicated smaller deviations than MY25 to the LES results in mid-CBL.

The LES results showed negative liquid water potential temperature heat flux $\langle w'\theta'_l \rangle$ above $z_* \geq 0.8$ with a minimum at CBL top indicating strong entrainment processes (Fig. 3.23(c, f, i, l)). MY25 showed a good agreement with the LES results in the lower CBL. However, it failed to reproduce strong negative values of $\langle w'\theta'_l \rangle$ as well as the minimum of $\langle w'\theta'_l \rangle$ at CBL top. Compared to MY25, the present model allowed a better agreement of $\langle w'\theta'_l \rangle$ with LES results, even in the entrainment zone. However, the entrainment temperature flux, parameterised by the present model showed an overestimation of the negative $\langle w'\theta'_l \rangle$ at CBL top.

To examine the impact of different approximations of turbulent mixing length on the parameterisation of turbulent fluctuations, a verification of the parameterised variances against LES results of various stability states was performed (Fig. 3.24). For the zonal velocity variance, only small differences of both models to the LES results were observed in bulk of the CBL (Fig. 3.24(a, d, g, j)). However, for LES cases with strong shear (cases B and G) showing a maximum of $\langle u'^2 \rangle$ at CBL top, the present model indicated a somewhat better agreement with LES results, compared to MY25.

Both models showed large deviations to the LES results of vertical velocity variance throughout the whole CBL (Fig. 3.24(b, e, h, k)). Primarily the maximum of the LES derived $\langle w'^2 \rangle$ was not reproduced in both models. However, the deviations between MY25 and the present models were rather low. Thus, the differences of $\langle w'^2 \rangle$ between LES results and parameterisation of vertical velocity variance were related to the down-gradient approach, used in both models. As seen from (Fig. 3.24(c, f, i, l)), LES derived variance of potential temperature was in good agreement with results of both models. This result indicated a low impact of turbulent mixing length formulation on the parameterisation of potential temperature fluctuations.

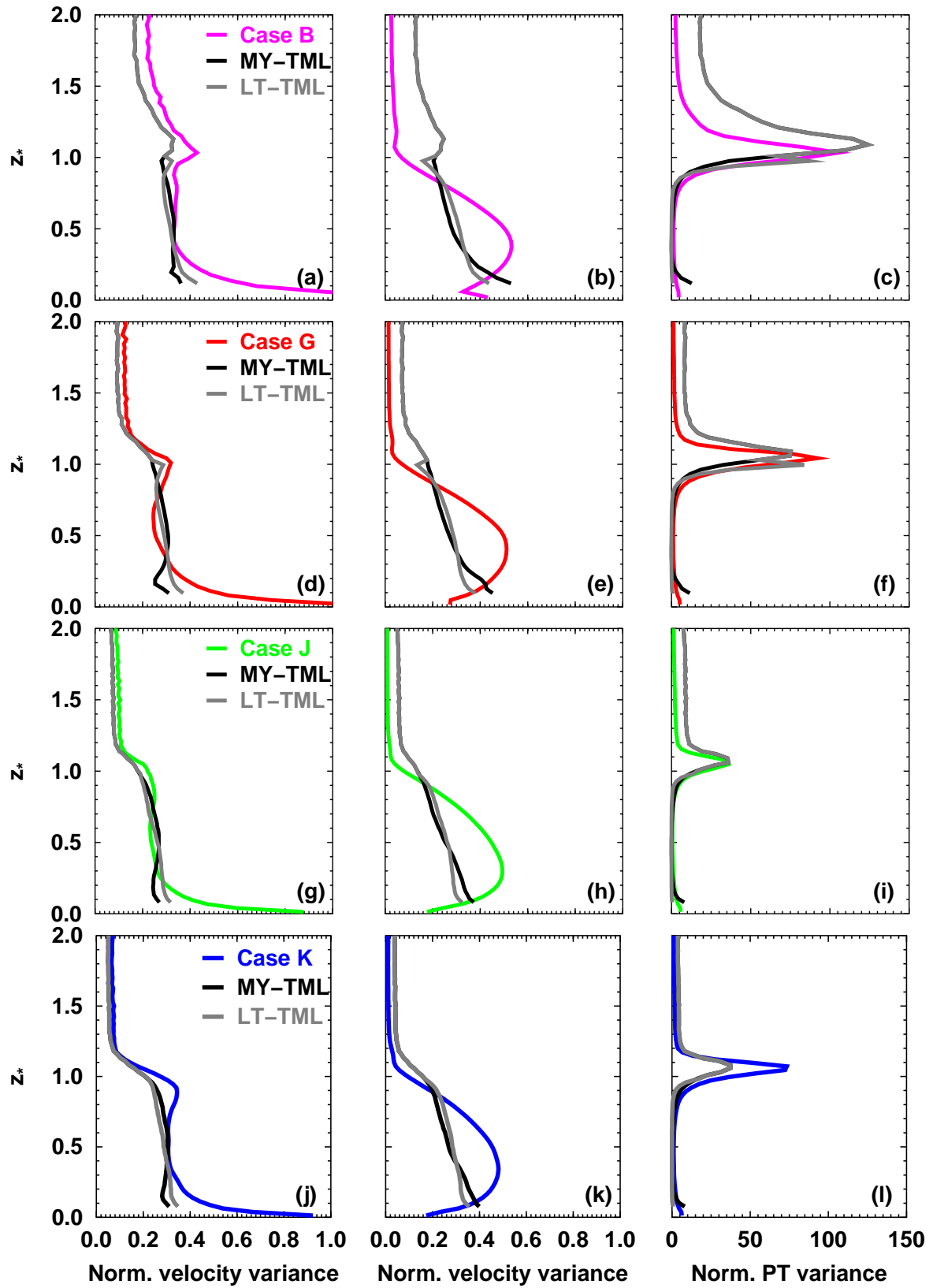


FIGURE 3.24: Normalised variances, derived from LES cases, based on Mellor-Yamada model (MY-TML), and based on present model containing LES-derived look-up table of turbulent mixing length (LT-TML). (a, d, g, j) variance of zonal wind velocity $\langle \overline{u'^2} \rangle / w_*^2$, (b, e, h, k) variance of vertical wind velocity $\langle \overline{w'^2} \rangle / w_*^2$, and (c, f, i, l) resolved part of potential temperature variance $\langle \overline{\theta'^2} \rangle / \theta_*^2$.

Examination of the mesoscale response to turbulent mixing length formulation

Based on a mesoscale simulation of the LITFASS-98 field experiment (Beyrich, 2001), the implications of the new turbulent mixing length formulation on results of atmospheric model simulations at regional scale were examined (Helmert and Hellmuth, 2002). Measurements and mesoscale simulation data of the intensive field campaign (LITFASS), which took place on the 18.06.1998 were used to evaluate the impact of different turbulent mixing formulations in unstable atmospheric conditions. The cloud coverage at the 18.06.1998 was characterised by convective and multi-layered clouds. Furthermore, precipitation events occurred.

4.1 Modelling system and setup of LITFASS

4.1.1 The mesoscale non-hydrostatic limited area model

The mesoscale simulation was based on the non-hydrostatic limited area model of the German Weather Service (DWD) (Doms *et al.*, 1998; Doms and Schättler, 1999). As part of the operational numerical weather prediction system of the DWD, LM is responsible for forecasts at meso- β scale using a horizontal grid resolution of 7 km (Doms *et al.*, 2002). The further improvement of LM is based on integrated approaches including measurements (e.g., Beyrich (2001)) as well as high-resolution numerical simulations of the “LITFASS-Lokal-Modell” (LLM) (Herzog *et al.*, 1998, 2002b) in a very large-eddy simulation mode.

The LM uses the compressible governing equations of atmospheric processes (Doms and Schättler, 1999) in rotated geographical coordinates. Generalised terrain following height coordinates are used in vertical direction (Fig. 4.1). Since this type of vertical coordinates requires an additional prognostic equation for the pressure replacing the continuity equation (Doms and Schättler, 1999), attempts have been made to use z -coordinate representation (Steppeler *et al.*, 2002).

Non-resolved physical processes were treated by the LM using the following parameterisations (Doms and Schättler, 1999; Balzer *et al.*, 2001; Doms *et al.*, 2002):

- TKE-based local turbulence closure approximation (Raschendorfer, 1999) of order 1 1/2 (Mellor and Yamada, 1974, 1982) (MY25) in terms of θ_l and q (see Sec. 2.2 and 3.4.2)
- Surface layer scheme (Raschendorfer, 1999)

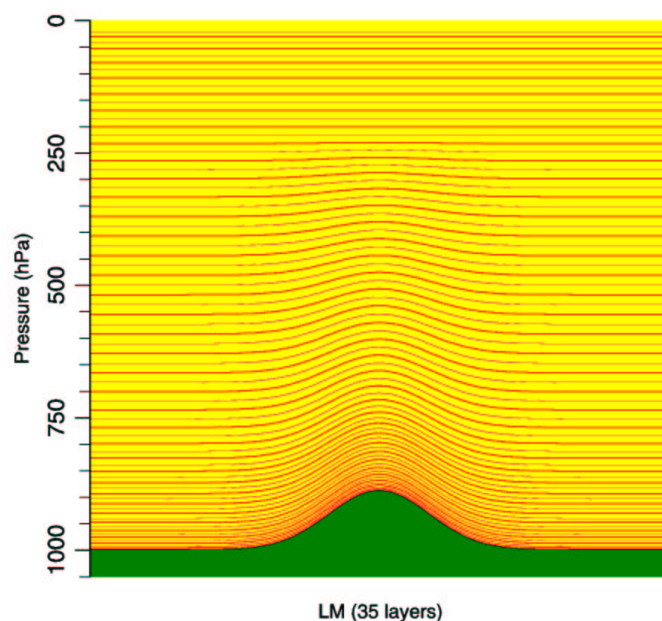


FIGURE 4.1: Generalised terrain following model layers of the Lokal-Modell (LM).

- Grid scale precipitation including parameterised cloud microphysics
- Diagnostic subgrid-scale cloud cover scheme
- Mass flux convection scheme for parameterisation of moist convection (Tiedtke, 1989)
- Radiation scheme for short- and long-wave radiation fluxes (Ritter and Geleyn, 1992)
- Vegetation model and 2-layer soil model (Jacobsen and Heise, 1982)

The model variables were staggered on an Arakawa-C/Lorenz grid to improve the accuracy of the difference approximations (Mesinger and Arakawa, 1976). Second order horizontal and vertical differencing was used for the spatial discretisation of the governing equations. The time integration scheme (Klemp and Wilhelmson, 1978) used small time steps, to take into account the propagation of sound waves.

4.1.2 Initial and boundary conditions of LITFASS

As seen from the surface weather chart of the 18.06.1998, 00:00 UTC (Fig. 4.2), a low-pressure system (Nadine) over the northern Baltic Sea and a high-pressure system (Wladimir) over south-west Europe led to a north-westerly flow over the measurement site of LITFASS. This site was located at the Meteorological Observatory Lindenberg (MOL) (52.167° N, 14.126° E) (see Fig. 4.2). Due to an extended, south-eastward moving warm front from Great Britain to Netherlands, rain showers with rain rates of about 10 mm/24 hrs in the mid-latitude mountains of

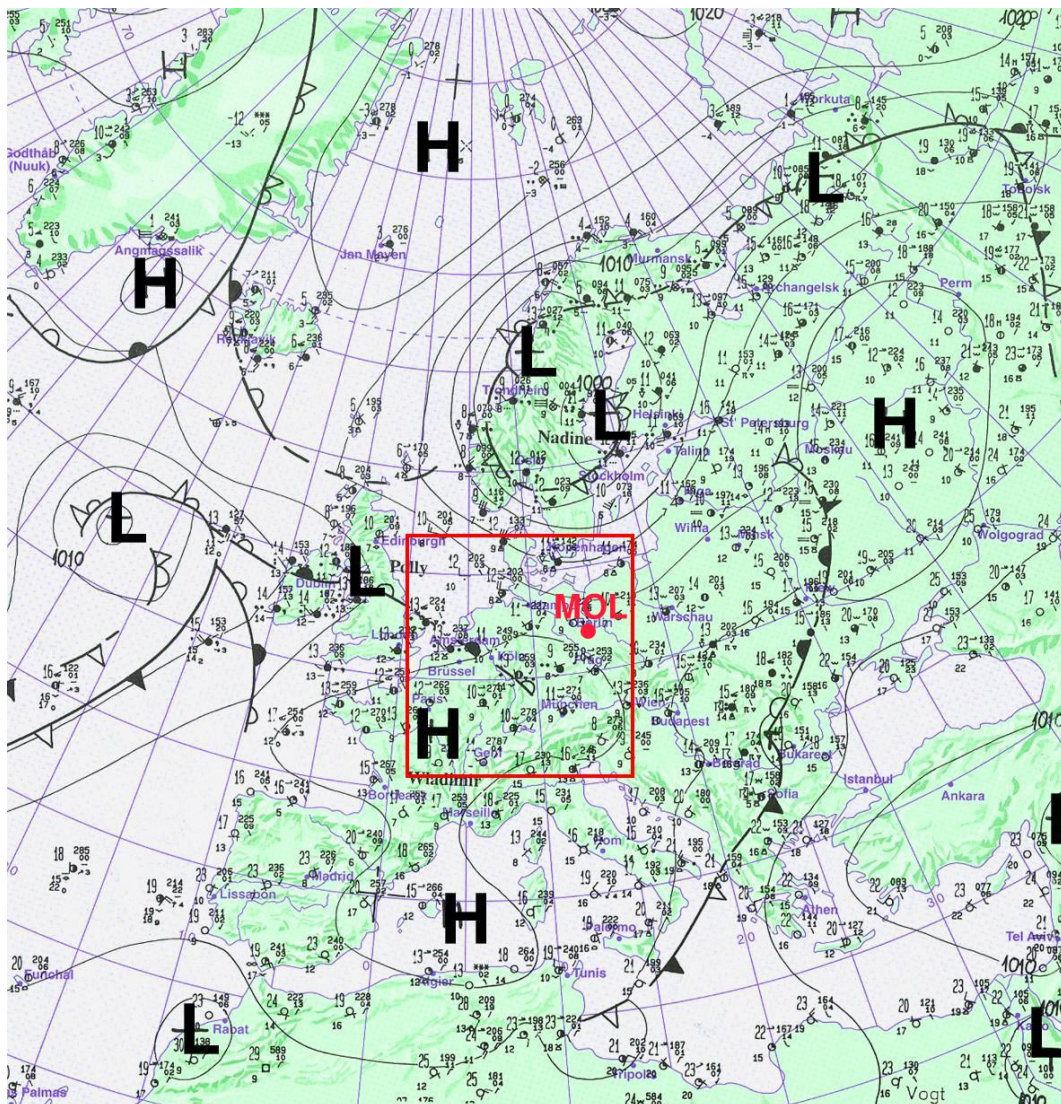


FIGURE 4.2: Surface weather chart (Berliner Wetterkarte) of the 18 June 1998 at 00:00 UTC. The letters “H” and “L” are used to denote high and low pressure systems. The solid red line describes the horizontal domain size of the LM. The location of the measurement site of LITFASS at the Meteorological Observatory Lindenberg is denoted by MOL.

Germany were observed. Synoptic observations in Berlin-Dahlem (52.28° N, 13.18° E) obtained near the measurement site of LITFASS (Tab. 4.1) indicated high-pressure conditions, associated with moderate wind speeds, and multi-level cloud coverage. However, the cloud coverage prevented the nocturnal boundary layer from strong temperature decrease as well as reduced the incoming solar radiation during daytime. The temperature near the surface exceeded 18° C in the afternoon.

Using initial datasets provided by the DWD, two LM simulations (RUN I, RUN II) of 24 hrs

TABLE 4.1: Observed synoptic conditions during LITFASS (18.06.1998) at measurement site Berlin-Dahlem (52.28° N, 13.18° E), where observed parameters are pressure p , 10 minutes average of wind speed U , temperature T , total cloud coverage CLC, low clouds CL, medium clouds CM, high clouds CH and height of the cloud base z_B . The measured mean wind direction was 270°.

Time (UTC)	p (hPa)	U (m/s)	T (K)	CLC (1/8)	CL	CM	CH	z_B (m)
00:00	1022.2	4.1	284.0	0	–	–	–	–
03:00	1022.4	3.1	282.5	1	–	Ac tr	–	–
06:00	1023.2	2.6	284.7	5	Cu hum	Ac tr	Ci spi, cas, flo	1200
09:00	1023.2	4.6	289.4	6	Cu hum	Ac tr	Ci spi, cas, flo	1000
12:00	1022.9	3.6	289.0	6	Cb cap	Ac cbgen	Ci spi, cas, flo	1100
15:00	1022.4	6.7	291.2	6	Cu med, con	Ac len	Ci spi, cas, flo	1200
18:00	1022.6	2.1	289.7	6	Cu, Sc	Ac tr	Ci fib	1100
21:00	1023.7	1.0	286.6	3	Sc cugen	Ac tr	Ci fib	1800
24:00	1023.3	3.1	283.1	0	–	–	–	–

of LITFASS based on LM version 2.16 with a time step of 40 s were performed. Location and horizontal extension of the LM domain consisting of 171×171 grid points in east-west and north-south direction are shown by the red solid line in Fig. 4.2. In vertical direction, 35 terrain following model levels were used (Fig. 4.1).

Both simulations RUN I and RUN II used the Mellor-Yamada scheme Level 2.5 (Raschendorfer, 1999) (see Sec. 2.2) with different formulations of the turbulent mixing length. RUN I used the original scheme, whereas RUN II used the new formulation (see Sec. 3.4.2) based on the LES database derived look-up table of stability dependent integral length scale approximation (Tab. A.2).

As shown by the three-dimensional views of the LITFASS LM domain of RUN I at 00:00 and 12:00 UTC (Fig. 4.3), the observed synoptic conditions were well represented by the LITFASS simulation. The north-westerly flow at 500 hPa level as well as multi-layered clouds were fairly reproduced. Compared to 00:00 UTC, the simulation at 12:00 UTC (Fig. 4.3) is characterised by a decreased cloud cover showing a cellular structure of the clouds over the land surface. This structure indicated convective turbulent cells, which were topped by cumulus clouds.

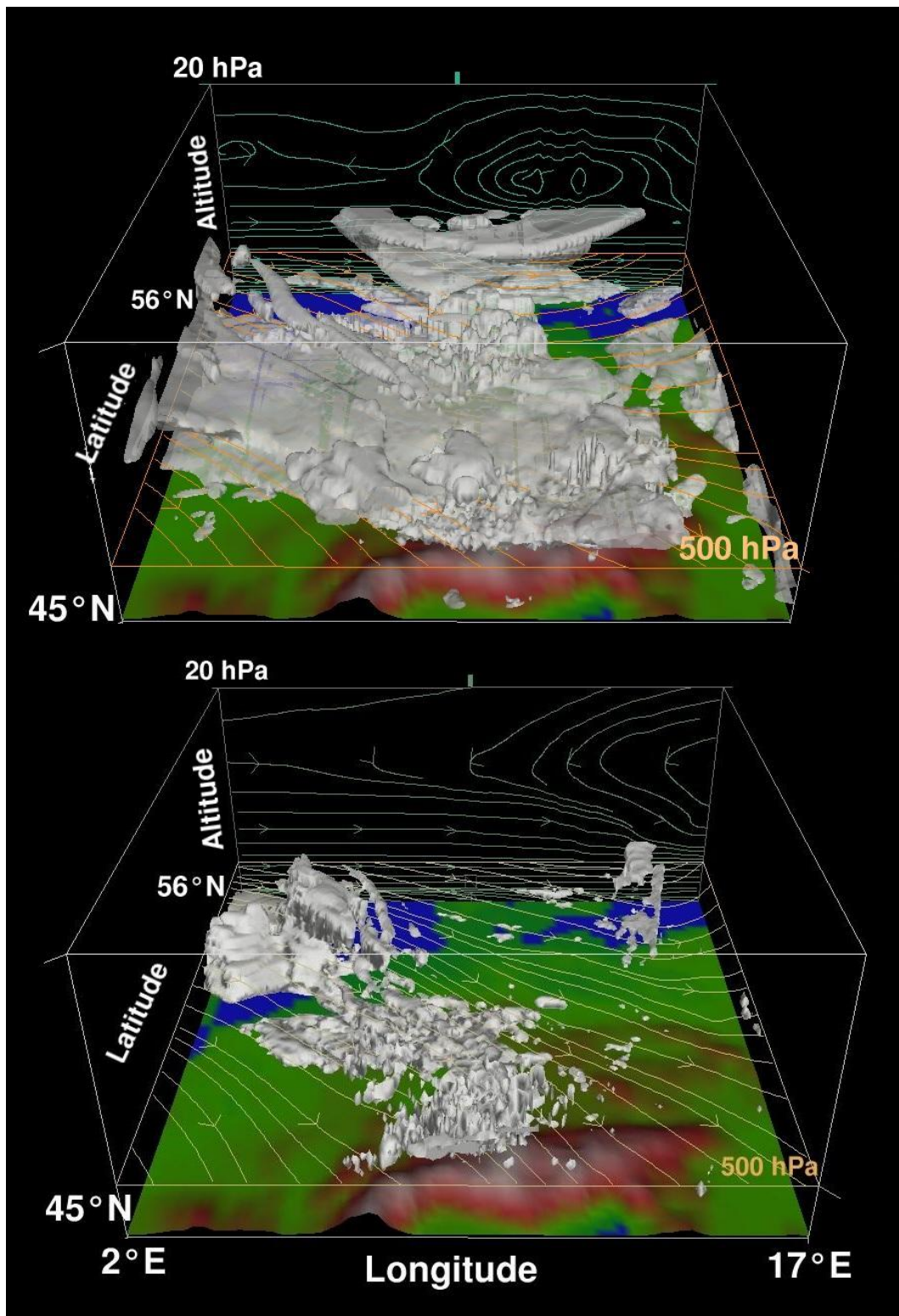


FIGURE 4.3: LITFASS LM domain of RUN I, (top) at 18.06.1998 00:00 UTC and (bottom) at 18.06.1998 12:00 UTC, where the white shaded area is the cloud cover, the orange vector field is the horizontal wind at the 500 hPa level and the green vector field is the vertical wind.

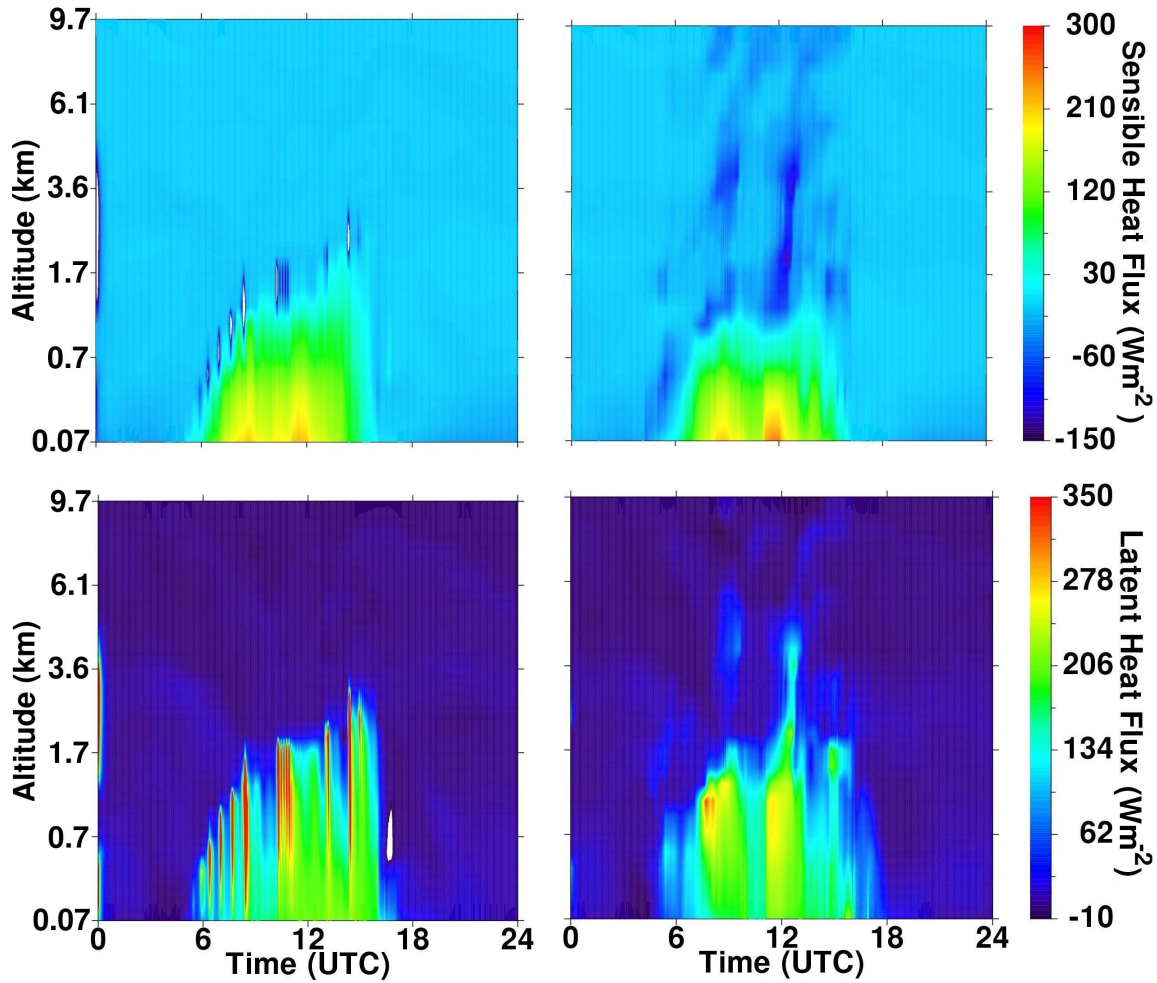


FIGURE 4.4: Time evolution of sensible (top) and latent (bottom) heat flux of LITFASS simulations RUN I (left) and RUN II (right) at grid point (129,109) of the LM domain.

4.2 Intercomparison of the LITFASS simulation results

The impact of different turbulent mixing lengths on the diurnal cycle of sensible and latent heat flux was examined (Fig. 4.4). The general evolution of the sensible and latent heat flux predicted by LITFASS simulations RUN I and RUN II at the measurement site of MOL (LM grid point 129, 109) showed a similar behaviour. The largest deviations between both runs occurred around 12:00 UTC, when the sensible and latent heat flux reached their maximum. The fluxes in the lower CBL $z \leq 500$ m were not strongly affected by changes in turbulent mixing length.

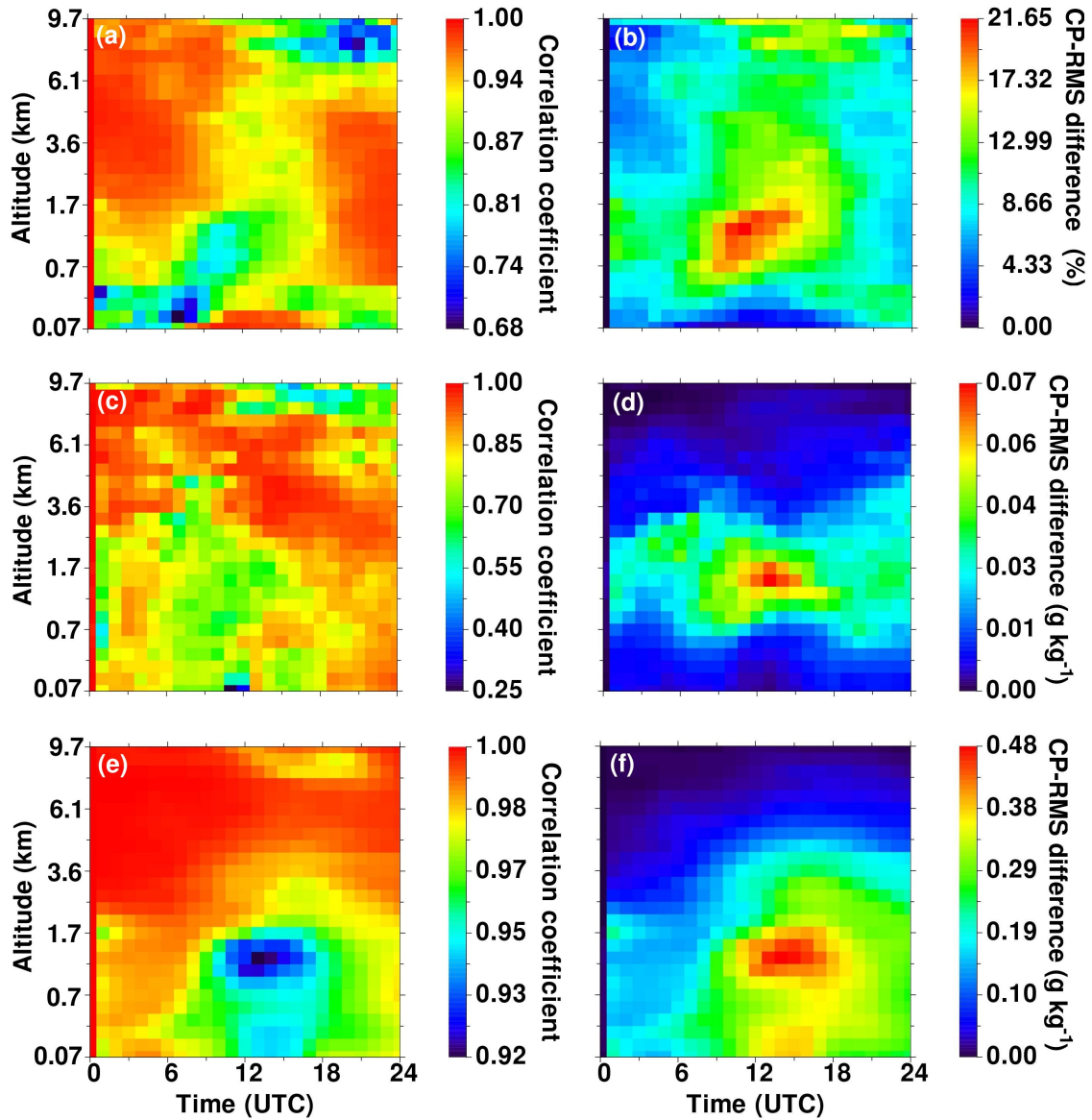


FIGURE 4.5: Time evolution of (left) correlation coefficient and (right) centred pattern root-mean-square difference determined from simulations RUN I and RUN II for (a, b) model cloudiness, (c, d) cloud water content, and (e, f) water vapour in dependence on altitude.

However, strong deviations for sensible and latent heat flux occurred in the upper CBL between both runs, indicated by differences in magnitude and time evolution of the (Fig. 4.4). They emphasised the observed impact of turbulent mixing length formulation (see Sec. 3.4.2) on the parameterised turbulent fluxes in the upper CBL.

To examine differences in the simulation results of RUN I and RUN II by a statistical analysis, correlation coefficient and centred pattern root-mean-square difference (e.g., Taylor (2001)) of

LM variables were used. The correlation coefficient of two 2D fields $A_{i,j}$ and $B_{i,j}$ is defined as

$$\rho_{A,B} = \frac{\frac{1}{N_x N_y} \sum_{i=1}^{N_x} \sum_{j=1}^{N_y} (A_{i,j} - \bar{A}) (B_{i,j} - \bar{B})}{\left\{ \frac{1}{N_x N_y} \sum_{i=1}^{N_x} \sum_{j=1}^{N_y} (A_{i,j} - \bar{A})^2 \right\}^{1/2} \left\{ \frac{1}{N_x N_y} \sum_{i=1}^{N_x} \sum_{j=1}^{N_y} (B_{i,j} - \bar{B})^2 \right\}^{1/2}}, \quad (4.1)$$

where N_x, N_y are the number of grid points in zonal and meridional direction of the LM domain. The mean values \bar{A}, \bar{B} are given as

$$\bar{A} = \frac{1}{N_x N_y} \sum_{i=1}^{N_x} \sum_{j=1}^{N_y} A_{i,j} \quad (4.2)$$

$$\bar{B} = \frac{1}{N_x N_y} \sum_{i=1}^{N_x} \sum_{j=1}^{N_y} B_{i,j}. \quad (4.3)$$

The centred pattern root-mean-square difference of the 2D fields $A_{i,j}$ and $B_{i,j}$ is defined as

$$\delta_{A,B}^{\text{CP}} = \left[\frac{1}{N_x N_y} \sum_{i=1}^{N_x} \sum_{j=1}^{N_y} \left\{ (A_{i,j} - \bar{A}) - (B_{i,j} - \bar{B}) \right\}^2 \right]^{1/2}. \quad (4.4)$$

Based on $A_{i,j}$ corresponding to results of RUN I and $B_{i,j}$ corresponding to results of RUN II horizontal cross sections of predicted 3D fields of LM variables were examined. These are related to cloud coverage $\text{CLC}(x,y,z)$, cloud-water content $q_c(x,y,z)$, and water vapour content $q_v(x,y,z)$.

As shown in Fig. 4.5, the implications of different turbulent mixing lengths for the considered LM variables were indicated by $\rho_{\text{I,II}}$ and $\delta_{\text{I,II}}^{\text{CP}}$. Since identical results of RUN I and RUN II would lead to $\rho_{\text{I,II}} = 1$ and $\delta_{\text{I,II}}^{\text{CP}} = 0$, low values of $\rho_{\text{I,II}}$ and high values of $\delta_{\text{I,II}}^{\text{CP}}$ were related to large deviations between both runs.

Largest deviations were observed around 12:00 UTC, when the strongest convection occurred (Fig. 4.4). Within the entrainment zone, the correlation coefficient showed values of $\rho_{\text{I,II}} = 0.8$ (CLC), $\rho_{\text{I,II}} = 0.6$ (q_c), and $\rho_{\text{I,II}} = 0.92$ (q_v). Here, the centred pattern root-mean-square difference showed maximum values of $\delta_{\text{I,II}}^{\text{CP}} = 22\%$ (CLC), $\delta_{\text{I,II}}^{\text{CP}} = 0.07 \text{ g kg}^{-1}$ (q_c), and $\delta_{\text{I,II}}^{\text{CP}} = 0.048 \text{ g kg}^{-1}$ (q_v). This result indicated a higher sensitivity of CLC and q_c on changes in turbulent mixing lengths. However, a lower sensitivity was found for q_v .

For neutral and stable stratification, the same formulation of turbulent mixing length is used in RUN I as well as RUN II. Thus, deviations between both runs were rather low at night showing $\rho_{\text{I,II}} \sim 1$ and $\delta_{\text{I,II}}^{\text{CP}} \sim 0$.

The implications of different formulations of turbulent mixing length scale on precipitation variables, predicted by RUN I and RUN II were examined. Correlation coefficient and centred pattern root-mean-square difference were determined from 2D fields of amount of rain (sum over

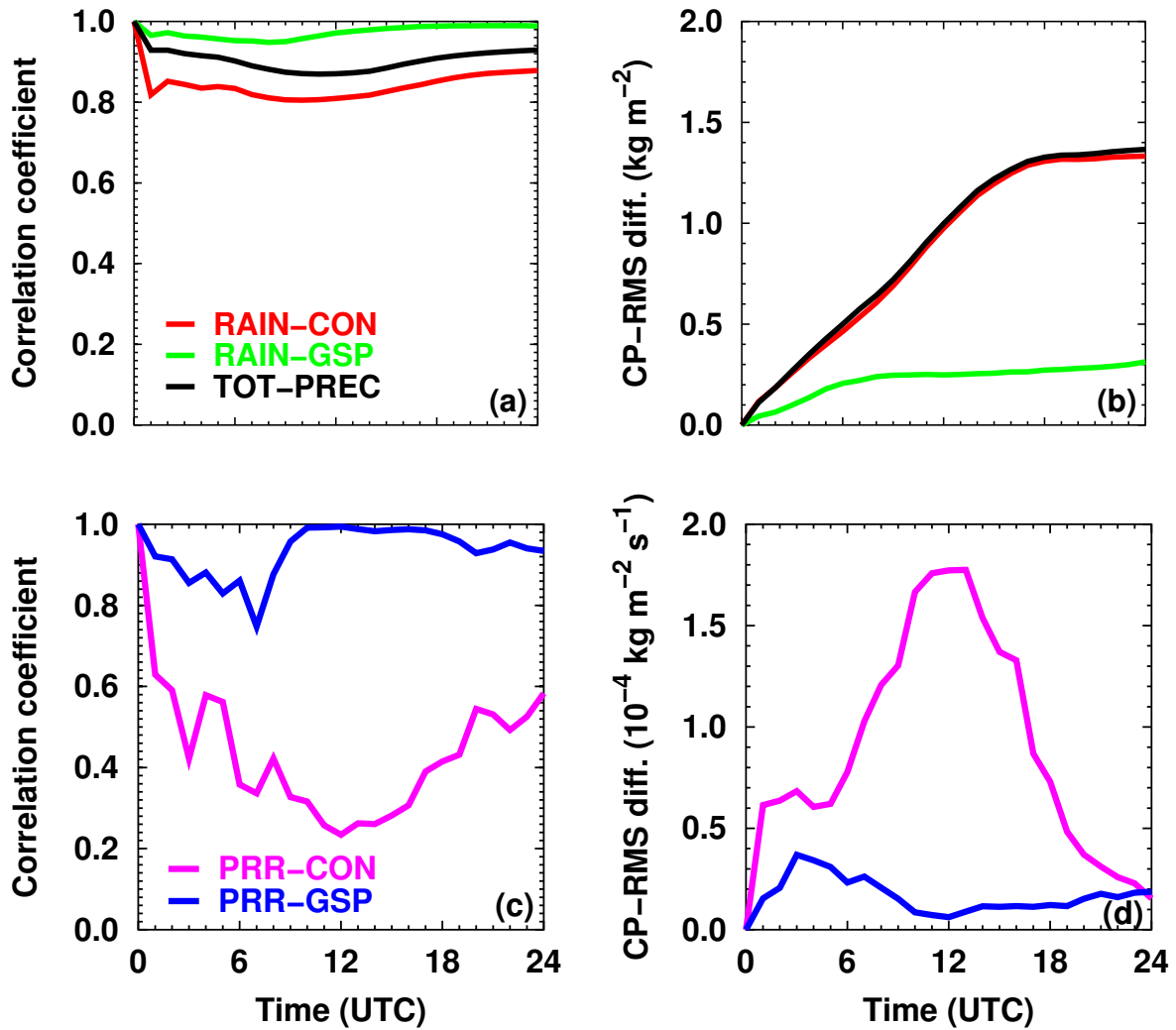


FIGURE 4.6: Time evolution of (a) correlation coefficient of amount of rain from convective (RAIN-CON) and from grid-scale precipitation (RAIN-GSP), and of total amount of precipitation (TOT-PREC), (b) centred pattern root-mean-square difference of RAIN-CON, RAIN-GSP, and TOT-PREC, (c) correlation coefficient of precipitation rates of convective rain (PRR-CON) and of grid-scale rain (PRR-GSP), (d) centred pattern root-mean-square difference of PRR-CON and PRR-GSP determined from simulations RUN I and RUN II.

forecast) from convective precipitation (RAIN-CON), amount of rain from gridscale (RAIN-GSP) precipitation, and amount of rain from total precipitation (TOT-PREC). Furthermore, 2D fields of precipitation rates of convective (PRR-CON) and grid-scale (PRR-GSP) precipitation were taken into account.

Compared to the gridscale precipitation variables (RAIN-GSP, PRR-GSP) and total amount of precipitation, lower values of correlation coefficient assuming a minimum around 12:00 UTC were observed for convective precipitation variables (RAIN-CON, PRR-CON) (Fig. 4.6(a, c)).

Furthermore, a pronounced maximum of centred pattern root-mean-square difference for convective precipitation rate occurred at 12:00 UTC (Fig. 4.6(d)). These results emphasised a stronger sensitivity of convective precipitation variables on changes of turbulent mixing length scale, compared to gridscale precipitation variables. The centred pattern root-mean-square difference of the variables related to amount of precipitation increased with time indicating an accumulation of the deviations between both runs with increasing integration time (Fig. 4.6(b)).

4.3 Verification of the LITFASS simulation results

4.3.1 Verification against satellite data

Based on the model-to-satellite approach (Morcrette, 1991), results of RUN I and RUN II were compared with infrared ($10.5 \mu\text{m}$ - $12.5 \mu\text{m}$) equivalent brightness temperatures T_{IR} and water vapour ($5.7 \mu\text{m}$ - $7.1 \mu\text{m}$) equivalent brightness temperatures T_{WV} , derived from METEOSAT observations (EUMETSAT, 2000). The approximation of T_{IR} and T_{WV} from simulation results took into account 3D fields of temperature, humidity, cloud cover, liquid water content, ice content, and pressure. Furthermore, predicted 2D fields of surface albedo, surface temperature, and surface pressure fields were considered (Hellmuth *et al.*, 2002).

The infrared equivalent brightness temperature was used to compare predicted and observed multilevel cloud coverage (Fig.4.7(a, b, c)). Since highest values of T_{IR} correspond to radiation coming from the surface, medium values of T_{IR} were related to low clouds, and lower values of T_{IR} were related to radiation emitted by medium and high clouds. Furthermore, predicted and observed water vapour equivalent brightness temperatures were considered for examination of cloud coverage (Fig.4.7(d, e, f)). In clear conditions, T_{WV} depends on water content above the 500 hPa level, whereas in cloudy conditions, T_{WV} is determined by cloud top temperature, cloud optical properties, and water vapour above the cloud layer (Roca *et al.*, 1997).

The patterns of observed T_{IR} (Fig.4.7(a)) and T_{WV} (Fig.4.7(d)) indicating an elongation of the clouds to the main flow from north-west to south-east, were well reproduced in both LM runs. However, the observed cloud cover in terms of brightness temperatures was clearly underestimated in both simulations.

Based on correlation coefficient and centred pattern root-mean-square difference, the implications of different turbulent mixing length on computed T_{IR} and T_{WV} were examined. Using $A_{i,j}$ related to interpolated 2D fields of T_{IR} and T_{WV} derived from METEOSAT (Heide, 2003), and $B_{i,j}$ related to computed 2D fields of T_{IR} and T_{WV} from the simulations, $\rho_{\text{M,I}}$, $\rho_{\text{M,II}}$ and $\delta_{\text{M,I}}^{\text{CP}}$, $\delta_{\text{M,II}}^{\text{CP}}$ were calculated after Eqs. (4.1)-(4.4).

Only a weak correlation for T_{IR} and T_{WV} was found between METEOSAT observations and results of RUN I, RUN II (Tab. 4.2). This could be due to an underestimation of the cloud long-wave impact by the assumption of too transparent clouds in the radiation model (Morcrette, 1991). Furthermore, an underestimation of simulation variables, related to computed T_{IR} and T_{WV} is possible.

The investigation of differences between RUN I and RUN II, compared to the METEOSAT observations ($\Delta\rho/\rho_{\text{M,I}}$ and $\Delta\delta^{\text{CP}}/\delta_{\text{M,I}}^{\text{CP}}$) showed in most cases only small deviations. This result

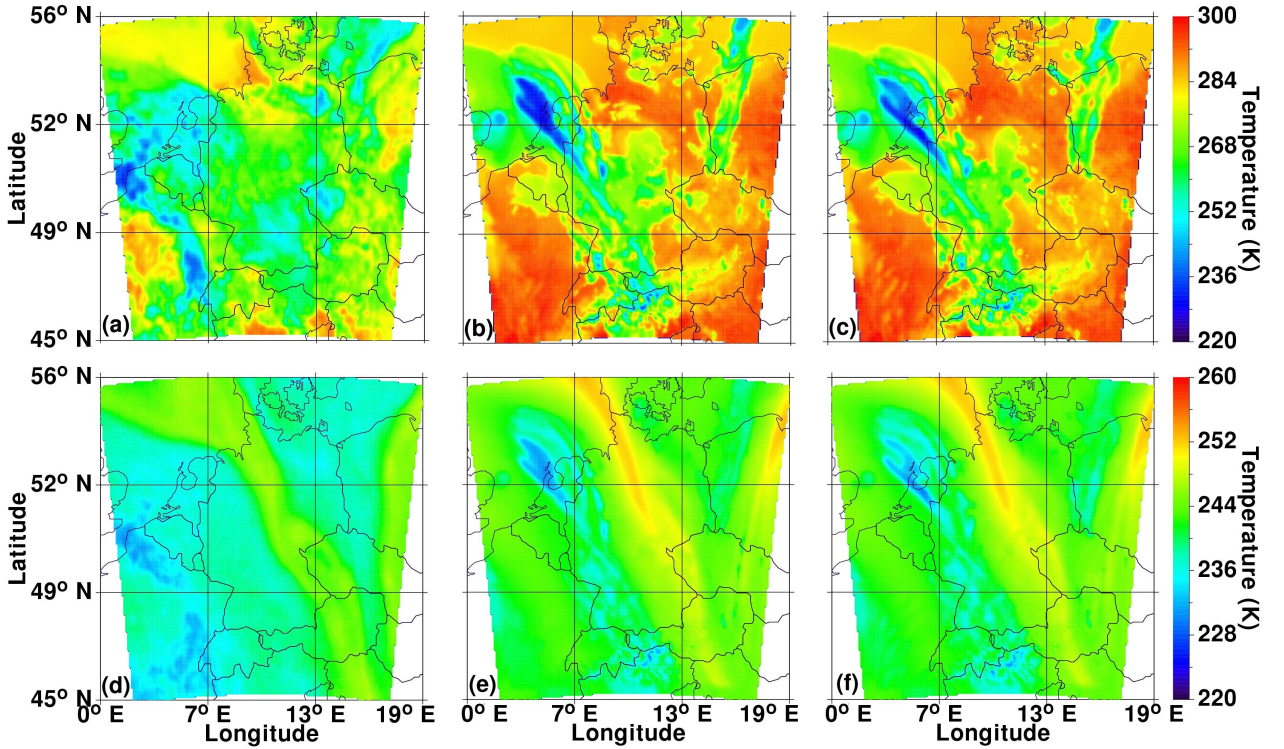


FIGURE 4.7: Verification of LITFASS simulations RUN I and RUN II against METEOSAT observations based on (top) infrared equivalent brightness temperatures and (bottom) water vapour equivalent brightness temperatures observed at 12:00 UTC by (a, d) METEOSAT and computed from LITFASS LM forecast of (b, e) RUN I and (c, f) RUN II using the model-to-satellite approach (Morcrette, 1991).

indicated a rather low sensitivity of T_{IR} and T_{WV} against changes in the formulation of the turbulent mixing length. However, indicated by positive $\Delta\rho/\rho_{\text{M,I}}$ and negative $\Delta\delta^{\text{CP}}/\delta_{\text{M,I}}^{\text{CP}}$, Tab. 4.2 suggested in some cases a better agreement (green areas) with T_{IR} and T_{WV} computed from RUN II and METEOSAT observations.

4.3.2 Verification against model-analysis data

A further examination of the impact of different turbulent mixing length formulations in RUN I and RUN II was performed using analysis data provided by DWD (Vogel and Schubert, 2002). The analysis data resulted from 4D data assimilation of LM (Schraff and Hess, 2002; Wergen, 2002) including specific moisture at surface $q_{v,s}$, 2 m-temperature $T_{2\text{m}}$, 2 m-dew point temperature $T_{d_{2\text{m}}}$, and 2 m-current (integration time) maximum (minimum) temperature $T_{\text{MAX}_{2\text{m}}}$ ($T_{\text{MIN}_{2\text{m}}}$). Furthermore, 10 m-zonal wind velocity $u_{10\text{m}}$, 10 m-meridional wind velocity $v_{10\text{m}}$, 10 m-horizontal wind velocity $U_{10\text{m}}$, and wind direction α as well as coverage with high, medium, and low clouds were taken into account.

The verification was based on correlation coefficient $\rho_{\text{A,I}}$, $\rho_{\text{A,II}}$ and centred pattern root-

TABLE 4.2: Verification of LITFASS simulations against METEOSAT observations of infrared (10.5 μm -12.5 μm) equivalent brightness temperature T_{IR} and water vapour (5.7 μm -7.1 μm) equivalent brightness temperature T_{WV} based on statistical measures (Eqs. (4.1)-(4.4)). Green areas are related to an increase and red areas to a decrease of $\Delta\rho/\rho_{\text{M,I}}$ and $\Delta\delta^{\text{CP}}/\delta_{\text{M,I}}^{\text{CP}}$.

Quantity	Time (UTC)	$\rho_{\text{M,I}}$	$\rho_{\text{M,II}}$	$\frac{\Delta\rho}{\rho_{\text{M,I}}} = \frac{\rho_{\text{M,II}} - \rho_{\text{M,I}}}{\rho_{\text{M,I}}}$ (·100 %)	$\delta_{\text{M,I}}^{\text{CP}}$ (K)	$\delta_{\text{M,II}}^{\text{CP}}$ (K)	$\frac{\Delta\delta^{\text{CP}}}{\delta_{\text{M,I}}^{\text{CP}}} = \frac{\delta_{\text{M,II}}^{\text{CP}} - \delta_{\text{M,I}}^{\text{CP}}}{\delta_{\text{M,I}}^{\text{CP}}}$ (·100 %)
T_{IR}	03:00	0.533	0.535	0.315	11.600	11.524	-0.652
	05:00	0.449	0.449	-0.122	13.011	12.945	-0.509
	09:00	0.417	0.429	2.716	13.624	13.410	-1.573
	12:00	0.304	0.303	-0.464	14.618	14.459	-1.094
	15:00	0.434	0.436	0.605	13.049	12.796	-1.934
	18:00	0.51	0.505	-0.977	11.128	10.793	-3.010
	21:00	0.507	0.506	-0.322	9.105	9.058	-0.525
	23:00	0.434	0.432	-0.429	9.449	9.414	-0.375
T_{WV}	03:00	0.719	0.723	0.504	2.396	2.352	-1.832
	05:00	0.680	0.684	0.574	2.586	2.565	-0.841
	09:00	0.676	0.679	0.375	2.912	2.899	-0.465
	12:00	0.548	0.553	0.963	3.362	3.331	-0.929
	15:00	0.471	0.469	-0.464	3.395	3.411	0.469
	18:00	0.434	0.450	3.847	3.215	3.059	-4.859
	21:00	0.301	0.294	-2.254	3.132	3.104	-0.874
	23:00	0.232	0.219	-5.458	3.215	3.223	0.251

mean-square difference $\delta_{\text{A,I}}^{\text{CP}}$, $\delta_{\text{A,II}}^{\text{CP}}$ (Eqs. (4.1)-(4.4)). Here, A_{ij} was related to 2D fields of analysis data and B_{ij} was related to 2D fields of RUN I, RUN II, respectively. The examination of deviations in wind direction between analysis data (A_{ij}) and simulation data (B_{ij}) was based on the mean deviation, given as

$$\delta\alpha_{\text{A,B}} = \frac{1}{N_x N_y} \sum_{i=1}^{N_x} \sum_{j=1}^{N_y} |\alpha_{A_{i,j}} - \alpha_{B_{i,j}}|. \quad (4.5)$$

Based on $\Delta\rho/\rho_{\text{A,I}}$ and $\Delta\delta^{\text{CP}}/\delta_{\text{A,I}}^{\text{CP}}$, the sensitivity on turbulent mixing length scale was examined using simulations and analysis data (Table 4.3). A large sensitivity was assumed for $\Delta\rho/\rho_{\text{A,I}} \geq +5\%$ and $\Delta\delta^{\text{CP}}/\delta_{\text{A,I}}^{\text{CP}} \leq -5\%$.

TABLE 4.3: Verification of LITFASS simulations against analysis data of 2 m-temperature $T_{2\text{ m}}$, 2 m-dew point temperature $T_{d_{2\text{ m}}}$, current (integration time) 2 m-maximum temperature $T_{\text{MAX}_{2\text{ m}}}$, current (integration time) 2 m-minimum temperature $T_{\text{MIN}_{2\text{ m}}}$, specific moisture at surface q_{v_s} , 10 m-zonal wind velocity $u_{10\text{ m}}$, 10 m-meridional wind velocity $v_{10\text{ m}}$, 10 m-horizontal wind velocity $U_{10\text{ m}}$, wind direction α , coverage with high (CLCH), medium (CLCM), and low clouds (CLCL) based on statistical measures ((Eqs. (4.1)-(4.4) and Eq. (4.5)). Green areas are related to an increase and red areas to a decrease of $\Delta\rho/\rho_{\text{M,I}}$, $\Delta\delta^{\text{CP}}/\delta_{\text{M,I}}^{\text{CP}}$, and $\Delta\delta\alpha/\delta\alpha_{\text{A,I}}$.

Quantity	Time (UTC)	$\rho_{\text{A,I}}$	$\rho_{\text{A,II}}$	$\frac{\Delta\rho}{\rho_{\text{A,I}}}$ (·100 %)	$\delta_{\text{A,I}}^{\text{CP}}$ (units of	$\delta_{\text{A,II}}^{\text{CP}}$ quantity)	$\frac{\Delta\delta^{\text{CP}}}{\delta_{\text{A,I}}^{\text{CP}}}$ (·100 %)	$\delta\alpha_{\text{A,I}}$ (°)	$\delta\alpha_{\text{A,II}}$ (°)	$\frac{\Delta\delta\alpha}{\delta\alpha_{\text{A,I}}}$ (·100 %)
$T_{2\text{ m}}$	06:00	0.95	0.951	0.1	0.84	0.835	-0.616			
	12:00	0.913	0.91	-0.343	1.637	1.714	4.7			
	18:00	0.955	0.954	-0.158	1.088	1.106	1.646			
$T_{d_{2\text{ m}}}$	06:00	0.92	0.912	-0.921	1.278	1.339	4.796			
	12:00	0.761	0.749	-1.456	1.909	1.947	1.967			
	18:00	0.783	0.787	0.423	1.905	1.886	-0.974			
$T_{\text{MAX}_{2\text{ m}}}$	06:00	0.945	0.947	0.231	0.886	0.869	-1.965			
	12:00	0.916	0.918	0.274	1.584	1.609	1.6			
	18:00	0.89	0.891	0.094	1.838	1.881	2.357			
$T_{\text{MIN}_{2\text{ m}}}$	06:00	0.906	0.904	-0.265	1.387	1.407	1.467			
	12:00	0.651	0.648	-0.465	2.769	2.781	0.454			
	18:00	0.948	0.948	0.048	1.189	1.185	-0.374			
q_{v_s}	06:00	0.906	0.909	0.321	1.402	1.414	0.891			
	12:00	0.598	0.516	-13.634	1.604	1.606	0.136			
	18:00	0.667	0.667	0.107	1.526	1.512	-0.914			
$u_{10\text{ m}}$	06:00	0.963	0.956	-0.725	0.834	0.866	3.817			
	12:00	0.849	0.833	-1.841	1.463	1.466	0.199			
	18:00	0.758	0.752	-0.737	1.577	1.566	-0.718			
$v_{10\text{ m}}$	06:00	0.922	0.887	-3.815	0.786	0.9	14.612			
	12:00	0.817	0.826	1.101	1.419	1.328	-6.424			
	18:00	0.797	0.812	1.902	1.231	1.14	-7.351			
$U_{10\text{ m}}$	06:00	0.955	0.944	-1.127	0.864	0.921	6.598			
	12:00	0.857	0.829	-3.363	1.284	1.376	7.175			
	18:00	0.781	0.774	-0.883	1.367	1.352	-1.068			
α	06:00							8.6	8.6	-0.7
	12:00							16.8	15.7	-6.8
	18:00							33.1	33.4	0.9
CLCH	06:00	0.595	0.601	1.006	0.372	0.37	-0.6			
	12:00	0.443	0.423	-4.479	0.446	0.455	2.012			
	18:00	0.333	0.353	6.12	0.418	0.41	-1.89			
CLCM	06:00	0.822	0.823	0.148	0.245	0.245	-0.32			
	12:00	0.705	0.7	-0.82	0.318	0.319	0.392			
	18:00	0.653	0.651	-0.348	0.342	0.341	-0.235			
CLCL	06:00	0.749	0.746	-0.42	0.289	0.291	0.491			
	12:00	0.629	0.698	10.88	0.358	0.319	-10.959			
	18:00	0.711	0.707	-0.592	0.315	0.314	-0.455			

The verification indicated only a weak sensitivity of most near surface variables on formulation of the turbulent mixing length (Table 4.3). Except for q_{v_s} , the $\Delta\rho/\rho_{M,I}$ was smaller than 5 %. Using $\Delta\delta\alpha/\delta\alpha_{A,I}$, the verification of observed and simulated wind direction indicated a sensitivity on turbulent mixing length in the order of $\Delta\delta\alpha/\delta\alpha_{A,I} \sim 7\%$ at 12:00 UTC.

The largest sensitivity was found for the coverage with low clouds at 12:00 UTC. The determined $\Delta\rho/\rho_{A,I} \sim +11\%$ and $\Delta\delta^{CP}/\delta_{A,I}^{CP} \sim -11\%$ suggested that compared to RUN I using the original scheme, the prediction of low cloud coverage was improved by the present model, contained in RUN II.

Due to the large sensitivity of low cloud coverage on turbulent mixing length, a closer examination using the 2D field of CLCL at 12:00 UTC was performed. The analysis data indicated a large area of low clouds, elongated from north-west to south-east of the LM domain (Fig. 4.8(a)). This was well reproduced in both simulations (Fig. 4.8(b,c)). However, the predicted low cloud coverage of RUN II indicated less clouds than RUN I in the north and the north-east of the LM domain (Fig. 4.8(c)). Compared to RUN I, this was in better agreement with the analysis data.

Based on centred subsections of CLCL at 12:00 UTC covering 128×128 LM gridpoints, the 2D covariance (Eq. (2.43)) for CLCL of analysis data and simulations were computed (Fig. 4.8). The stretching of $R_{A,I}^{CLCL}(r_x, r_y)$ and $R_{A,II}^{CLCL}(r_x, r_y)$, respectively reflected the elongation of the CLCL field (Fig. 4.8). This indicated a higher correlation of CLCL in the direction of the elongation than in perpendicular direction. Compared to $R_{A,I}^{CLCL}(r_x, r_y)$, higher values of $R_{A,II}^{CLCL}(r_x, r_y)$ at small positive displacements r_y emphasised the better agreement of CLCL predicted by RUN II with CLCL from the analysis data at the north of the LM domain.

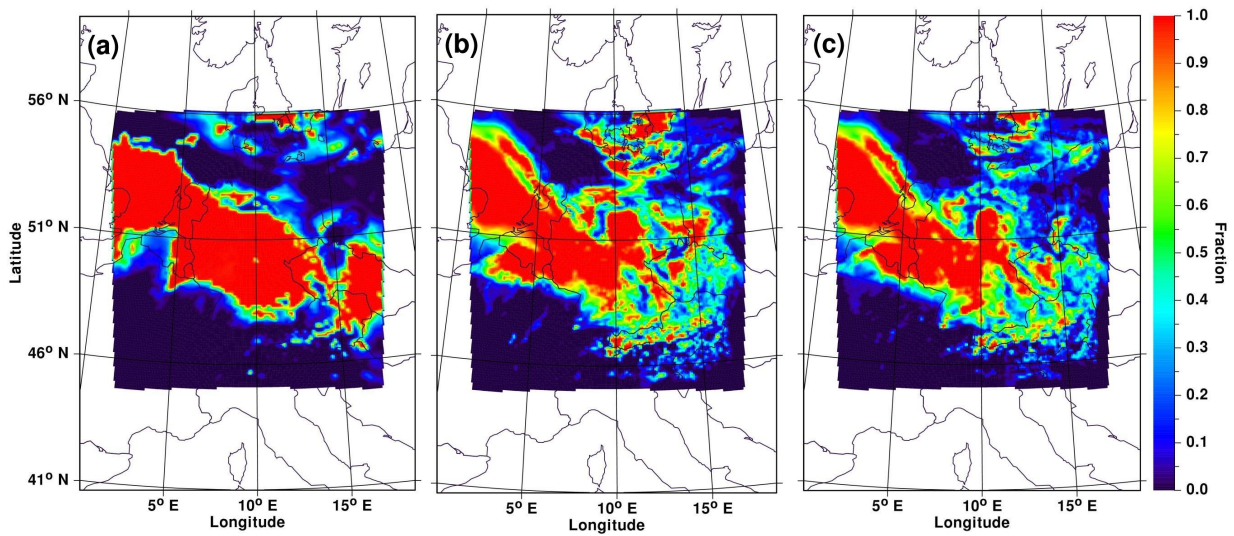


FIGURE 4.8: Coverage with low clouds (CLCL) at 12:00 UTC determined from (a) analysis data, (b) LITFASS simulation RUN I, and (c) LITFASS simulation RUN II.

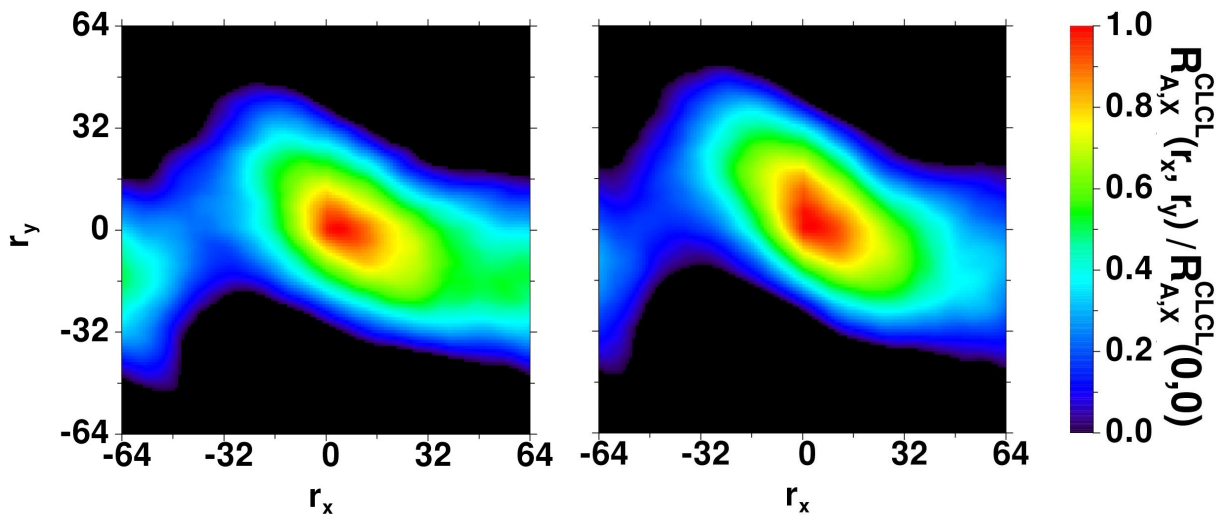


FIGURE 4.9: Normalised 2D covariance of coverage with low clouds (CLCL), (left) based on CLCL of model analysis database and LITFASS simulation RUN I (X=I) and (right) based on CLCL of model analysis database and LITFASS simulation RUN II (X=II).

Conclusions and future directions

Turbulence parameterisations, used in regional and large scale atmospheric models are often based on local closure schemes. However, these schemes are known to show serious deficiencies in simulation of the convective boundary layer, since they fail to represent the impact of coherent turbulence structures on mean variables. Even under convective conditions, these structures are of primary importance. They contain most of the turbulent energy and dominate the vertical turbulent transports.

Based on down-gradient approximation, local closure schemes (e.g., the popular Mellor-Yamada model) often use a master length scale to determine the eddy diffusivity. However, such a master length scale is representative of neutral atmospheric stability. Thus, this approach requires additional dimensionless stability functions to take into account stable and unstable stratification. However, these stability functions depends on local gradient Richardson number. Therefore, they have difficulties to account for varying vertical stratification throughout the whole depth of the CBL. This is primarily important for the parameterisation of entrainment processes in the upper CBL, which strongly influence cloud development. However, clouds have a large impact on radiation balance between the atmosphere and earth's surface. Thus, an improvement of formulations for the turbulent mixing length is of great importance to improve present-day atmospheric models.

The aim of this work was the examination of a new formulation of characteristic turbulence length scales for application in turbulence parameterisation. Since these length scales are related to the energy spectrum of turbulent fluctuations, empirical stability functions are not required any longer. However, this approach requires the determination of characteristic turbulence length scales over a wide range of CBL stability conditions. Although measurements are very useful to examine energy spectra and characteristic turbulence length scales, they are representative only for a limited parameter space. Due to the non-linearity of turbulent processes, a generalisation of characteristic turbulence length scales based on a few measurement results is very difficult or impossible, respectively.

Therefore, in this work the characteristic turbulence length scales were derived from large-eddy simulations. Based on a LES model that considers cloud formation and radiative processes, dry and moist CBLs were simulated. Covering atmospheric stability from $-z_i/L_{MO} = 2 - 48$, these simulations provide high resolution 3D turbulence data. Based on a representative subset of four simulations, the flow statistics and turbulence properties of the simulated CBLs were examined at final state (after 9 hrs integration time). At this time, the simulations were in quasi-steady state, indicated by a linear change with height of the turbulent fluxes of momentum and heat. Compared to the resolved flow statistics, non-resolved turbulence processes had only minor

impact on the LES results except for the near surface range.

The simulated CBLs showed a vertical structure, which agreed well with observations as well as with theoretical expectations, consisting of a well mixed layer, which was topped by an entrainment zone. Indicated by large gradients of mean horizontal wind velocity, temperature, and total water content at CBL top, strong entrainment was simulated. Based on an examination of the variances of horizontal wind velocity and temperature, a dependence on atmospheric stability parameter was found for the entrainment strength. In agreement with observations and theoretical considerations, a strong maximum of vertical velocity variance at mid-CBL was observed indicating that coherent structures contribute the main part to the TKE within the well mixed layer. Based on two-dimensional auto-covariances of vertical velocity, temperature and TWC, coherent structures in the simulated CBLs were examined and an occurrence of role structures was observed. The structure wavelengths of these role structures were in the order of twice the CBL depth at mid-CBL. These findings agreed in order of magnitude with aircraft measurements, numerical simulations, and laboratory experiments.

Taking into account, turbulent fluctuations of vertical velocity, temperature, and TWC, averaged energy spectra and auto-covariance functions in all LES model levels of the simulated CBL were determined. They were used to derive vertical profiles of characteristic turbulence length scales in dependence on atmospheric stability. These length scales were related to peak wavelength and integral length scale, representative of the LES resolved energy-containing range. In agreement with theoretical expectations, both characteristic turbulence length scales indicated a pronounced dependence on CBL stability. Furthermore, the assumption derived from measurements of an analytical relationship between peak wavelength and integral length scale of vertical velocity was confirmed. Moreover, the LES results indicated a similar relationship for characteristic turbulence length scales of temperature and TWC. A dependence on stability was observed for the ratio of peak wavelength to integral length scale of vertical velocity and virtual potential temperature.

A comprehensive verification of the characteristic turbulence length scales of vertical velocity was performed. Although a comparison with laboratory experiments showed some deviations, a good agreement with numerical simulations and atmospheric measurements was found. The differences with laboratory experiments are mainly related to an overestimation of role structures in the laboratory flows associated with an underestimation of entrainment processes. Therefore, further investigations are necessary, e.g., setup of LES input parameter more comparable with laboratory conditions. The LES derived characteristic length scales of virtual potential temperature and TWC constitute a unique data set, required for comparison with future measurements.

Based on non-linear least square fitting, an former approximation for the peak wavelength of vertical velocity was revised by the LES results and extended to a larger parameter space. Furthermore, a new formulation for the integral length scale of vertical velocity was developed using non-linear least square fitting of LES derived integral length scales for different stability parameters. The resulting database of fit parameters reflects the impact of atmospheric stability on the integral length scale approximation. The reliability of this new approximation was examined by a statistical analysis. The results indicated a high significance of the new approximation for integral length scale over the range of simulated stability states.

The application of the new integral length scale approximation in a revised turbulent mix-

ing length formulation for the Mellor-Yamada model was examined. Thus, a verification of the revised Mellor-Yamada scheme using the new turbulent mixing length formulation against the Mellor-Yamada scheme with master length scale was performed. Compared to the original Mellor-Yamada model, the new formulation indicated larger values of eddy diffusivity coefficients in the upper CBL. A comparison with turbulent fluxes and variances derived from LES showed an improvement of the revised Mellor-Yamada scheme for the parameterisation of turbulent fluxes and variances in the upper CBL.

The implications of the revised turbulent mixing length formulation on the evolution of the dynamic and thermodynamic state of the atmosphere at regional scale were examined for a mesoscale model simulation. A simulation scenario based on 24 hrs of the most intensive measurement campaign during the LITFASS-98 field experiment was successfully used as a test case for the revised turbulent mixing length.

A model-to-model comparison showed a strong impact of the mixing length on magnitude and time evolution of sensible and latent heat flux, primarily in the entrainment zone range of the well developed CBL. Furthermore, 3D simulation fields of cloud coverage, cloud-water content, and water vapour as well as two-dimensional precipitation fields of both simulations were examined by a statistical analysis. The results indicated a non-negligible impact of the revised turbulent mixing length on cloud parameters and convective induced precipitation.

The verification of the simulation results against observations was based on analysis data, derived from 4D data assimilation and from satellite observations of METEOSAT. However, the present data assimilation provided only observations related to near-surface variables and to the cloud coverage in discrete model levels. The METEOSAT observations of infrared brightness temperatures have been compared with simulated one from model-to-satellite approach taking into account a large number of predicted 2D and 3D mesoscale fields.

The impact of various turbulent mixing lengths on near-surface fields and brightness temperatures was low as expected. However, for the present simulation the verification against observed cloud coverage, derived from data assimilation indicated an improvement of simulated low cloud coverage in case of the LES derived turbulent mixing length. Compared to simulation results using the master length scale this improvement was in the order of 11 %.

A comprehensive assessment of the new turbulent mixing length formulation requires much more simulations at regional and global scale. However, an improved verification of these simulations needs 3D measurement data of liquid-water content, water vapour and microphysical cloud properties. As a first step in this direction, the new formulation was successfully applied by the DWD Potsdam for LM verification during the whole LITFASS measurement campaign (May/June 1998). It is also intended to be applied in the very large-eddy simulation model of the DWD ("LITFASS Lokal-Modell (LLM)"). The revised scheme can only be evaluated on a statistical base, i.e., running it for a large number of weather situations in a systematic way. In close co-operation with DWD, now the revised turbulence length scheme will be extensively verified in the framework of the routinely NWP procedure.

Thus, the examination results of this thesis can contribute to a further improvement of reliability and significance of atmospheric model simulations. These are required in numerical weather prediction, air pollution modeling as well as regional integrated models for an improved assessment of the implications of global change on natural and social systems.

Non-linear least square fit parameters of peak wavelength and integral length scale

A.1 Peak wavelength of the vertical velocity

TABLE A.1: Parameter set for approximation of $\langle(\lambda_m)_w\rangle$ (Eq. (3.23)), where χ_r^2 and Q are measures for the goodness-of-fit, a_i are fit parameter, and Δa_i the corresponding standard deviations.

Case	χ_r^2	Q	a_0	Δa_0	a_1	Δa_1	a_2	Δa_2	a_3	Δa_3	a_4	Δa_4
A	0.08	1.000	9.45	0.10	1.183	0.042	11.02	0.45	6.3E-2	2.6E-2	1.43	0.34
B	0.28	2.2E-8	11.60	0.19	1.143	0.023	10.72	0.44	5.0E-4	4.2E-4	7.14	0.85
C	1.17	0.086	9.99	0.33	0.754	0.048	18.23	0.85	8.0E-2	3.3E-2	2.32	0.42
D	0.77	0.172	10.86	0.26	0.916	0.012	11.79	0.40	5.5E-5	5.0E-5	9.26	0.94
E	1.12	0.156	11.65	0.56	0.960	0.021	8.91	0.35	4.1E-4	3.6E-4	7.30	0.89
F	1.25	0.022	11.93	0.51	0.807	0.024	11.10	0.54	6.1E-5	1.6E-4	9.06	2.73
G	0.78	0.959	11.87	0.37	1.072	0.017	10.41	0.37	1.6E-4	1.5E-4	8.25	0.96
H	0.94	0.673	12.30	0.19	0.960	0.016	11.38	0.43	2.0E-4	2.0E-4	7.88	0.96
I	0.30	1.000	11.70	0.22	1.066	0.013	9.75	0.23	9.6E-4	4.8E-4	6.38	0.51
J	1.39	0.002	11.00	0.37	0.758	0.014	12.47	0.66	3.0E-7	1.7E-6	14.02	5.81
K	1.02	0.418	11.98	0.29	1.063	0.017	8.98	0.27	9.7E-5	6.7E-5	8.96	0.72
L	0.33	1.000	10.09	0.16	0.968	0.013	10.28	0.26	2.2E-4	1.8E-4	7.76	0.85
M	1.05	0.321	11.07	0.28	0.868	0.017	10.67	0.30	3.4E-4	3.1E-4	7.28	0.91
N	0.23	1.000	10.55	0.26	0.884	0.006	9.66	0.20	9.2E-4	3.4E-4	6.46	0.37

A.2 Integral length scale of the vertical velocity

TABLE A.2: Parameter set for approximation of $\langle \Lambda_w \rangle$ (Eq. (3.24)), where χ_r^2 and Q are measures for the goodness-of-fit, a_i are fit parameter, and Δa_i the corresponding standard deviations.

Case	χ_r^2	Q	a_0	Δa_0	a_1	Δa_1	a_2	Δa_2	a_3	Δa_3
A	0.59	1.000	1.910	0.091	0.4905	0.0074	0.8382	0.0188	0.969	0.132
B	0.04	1.000	1.992	0.025	0.4773	0.0033	0.8910	0.0026	1.444	0.047
C	3.73	3.1E-44	1.754	0.144	0.3092	0.0169	0.5610	0.4045	-0.104	0.781
D	0.42	1.000	1.756	0.047	0.4251	0.0057	0.9004	0.0046	1.390	0.082
E	0.16	1.000	1.819	0.051	0.3603	0.0019	0.8933	0.0038	1.378	0.049
F	0.03	1.000	1.857	0.009	0.3630	0.0013	0.9074	0.0022	1.822	0.046
G	0.29	1.000	1.704	0.015	0.3930	0.0041	0.8991	0.0046	2.457	0.140
H	0.07	1.000	1.736	0.016	0.3581	0.0014	0.8961	0.0020	2.281	0.047
I	0.61	1.000	1.736	0.009	0.3886	0.0039	0.8877	0.0058	1.591	0.082
J	0.14	1.000	1.402	0.019	0.3219	0.0016	0.8552	0.0060	1.565	0.060
K	0.33	1.000	1.659	0.012	0.4087	0.0038	0.8452	0.0086	0.780	0.068
L	0.23	1.000	1.584	0.025	0.3321	0.0029	0.8732	0.0059	1.605	0.080
M	0.17	1.000	1.570	0.012	0.3166	0.0020	0.9211	0.0024	2.708	0.062
N	1.54	3.2E-5	1.506	0.029	0.3510	0.0034	0.9586	0.0041	3.818	0.220

A.3 Peak wavelength of the virtual potential temperature

TABLE A.3: Parameter set for approximation of $\langle(\lambda_m)_{\theta_v}\rangle$ (Eq. (3.26)), where χ_r^2 and Q are measures for the goodness-of-fit, a_i are fit parameter, and Δa_i the corresponding standard deviations.

Case	χ_r^2	Q	a_0	Δa_0	a_1	Δa_1
A	0.70	0.996	34.52	2.30	1.1462	0.0143
B	0.12	1.000	24.86	0.49	1.4258	0.0046
C	6.39	0.000	22.51	1.27	1.1976	0.0163
D	2.47	1.5E-17	20.41	0.70	1.0785	0.0118
E	1.83	4.8E-9	22.48	1.08	1.0048	0.0103
F	0.70	0.998	19.81	0.79	1.0061	0.0053
G	0.80	0.944	29.62	0.44	1.2731	0.0027
H	0.79	0.964	22.79	1.55	1.0430	0.0068
I	0.36	1.000	23.67	0.46	1.0659	0.0056
J	0.98	0.550	20.11	0.47	1.0049	0.0084
K	1.62	3.6E-6	21.25	0.51	1.0800	0.0076
L	0.70	0.998	20.20	0.74	0.9815	0.0060
M	1.16	0.085	22.37	1.58	0.9651	0.0037
N	0.56	1.000	19.25	1.37	0.8625	0.0055

A.4 Integral length scale of the virtual potential temperature

TABLE A.4: Parameter set for approximation of $\langle \Lambda_{\theta_v} \rangle$ (Eq. (3.26)), where χ_r^2 and Q are measures for the goodness-of-fit, a_i are fit parameter, and Δa_i the corresponding standard deviations.

Case	χ_r^2	Q	a_0	Δa_0	a_1	Δa_1
A	3.85	1.4E-44	8.36	0.43	0.2942	0.0053
B	1.04	0.373	5.26	0.47	0.3919	0.0082
C	3.57	2.4E-41	5.24	0.31	0.2321	0.0033
D	0.29	1.000	5.34	0.11	0.2985	0.0017
E	2.86	1.2E-27	4.49	0.13	0.2175	0.0021
F	0.31	1.000	4.81	0.25	0.2502	0.0025
G	0.31	1.000	5.90	0.31	0.3157	0.0034
H	1.02	0.420	4.17	0.16	0.2299	0.0037
I	1.43	0.001	4.17	0.30	0.2447	0.0027
J	2.13	3.8E-13	3.84	0.10	0.2280	0.0035
K	2.35	1.4E-17	3.93	0.31	0.2583	0.0031
L	0.54	1.000	4.83	0.16	0.2078	0.0015
M	1.03	0.383	4.65	0.17	0.2173	0.0033
N	1.98	1.5E-11	5.18	0.60	0.2644	0.0026

A.5 Peak wavelength of the total water content

TABLE A.5: Parameter set for approximation of $\langle(\lambda_m)_q\rangle$ (Eq. (3.26)), where χ_r^2 and Q are measures for the goodness-of-fit, a_i are fit parameter, and Δa_i the corresponding standard deviations.

Case	χ_r^2	Q	a_0	Δa_0	a_1	Δa_1
A	0.96	0.612	52.48	7.23	1.4507	0.0174
B	0.84	0.874	48.58	6.22	1.8668	0.0150
C	0.62	1.000	38.06	1.42	1.5448	0.0047
D						
E	0.28	1.000	29.32	0.73	1.1417	0.0038
F	0.23	1.000	28.31	0.83	1.1964	0.0053
G	2.99	1.2E-24	44.55	3.52	1.6502	0.0153
H	0.26	1.000	43.41	0.37	1.7413	0.0126
I						
J	0.63	1.000	33.34	1.89	1.3863	0.0105
K	0.58	1.000	40.06	1.28	1.2989	0.0065
L	0.02	1.000	52.17	1.02	1.7871	0.0057
M	0.06	1.000	43.71	1.49	1.4780	0.0047
N	0.13	1.000	48.98	2.18	1.8003	0.0171

A.6 Integral length scale of the total water content

TABLE A.6: Parameter set for approximation of $\langle \Lambda_q \rangle$ (Eq. (3.26)), where χ_r^2 and Q are measures for the goodness-of-fit, a_i are fit parameter, and Δa_i the corresponding standard deviations.

Case	χ_r^2	Q	a_0	Δa_0	a_1	Δa_1
A	2.06	1.6E-11	14.39	1.98	0.3705	0.0076
B	0.25	1.000	13.77	1.10	0.5688	0.0047
C	0.33	1.000	8.40	0.26	0.3465	0.0020
D						
E	1.36	0.003	5.85	0.14	0.2437	0.0022
F	0.05	1.000	8.47	0.23	0.3109	0.0006
G	1.22	0.057	9.92	0.47	0.4737	0.0048
H	0.26	1.000	12.55	0.49	0.5918	0.0031
I						
J	1.51	1.1E-4	8.30	1.56	0.3536	0.0065
K	0.44	1.000	10.03	0.54	0.3405	0.0042
L	0.14	1.000	13.37	0.42	0.5434	0.0038
M	0.01	1.000	12.74	0.22	0.4711	0.0009
N	0.34	1.000	13.17	0.52	0.4939	0.0031

Approximation of peak wavelength and integral length scale

B.1 Approximation of the peak wavelength

FIGURE B.1: Horizontally averaged peak wavelengths $\langle(\lambda_m)_w\rangle$, $\langle(\lambda_m)_{\theta_v}\rangle$, and $\langle(\lambda_m)_q\rangle$ (coloured solid lines) for (a-c) cases B, (d-f) G, (g-i) J and (j-l) K, where the black solid lines denote the fit approximation (Eq. (3.23)) using fit parameter of Tab. A.1,A.3, and A.5. Grey shaded areas denote the standard deviations $\sigma_{(\lambda_m)_w}$, $\sigma_{(\lambda_m)_{\theta_v}}$, and $\sigma_{(\lambda_m)_q}$.

B.2 Approximation of the integral length scale

FIGURE B.2: Horizontally averaged integral length scales $\langle\Lambda_w\rangle$, $\langle\Lambda_{\theta_v}\rangle$, and $\langle\Lambda_q\rangle$ (coloured solid lines) for (a-c) cases B, (d-f) G, (g-i) J, and (j-l) K, where the black solid lines denote the fit approximation (Eq. (3.24)) using fit parameter of Tab. A.2,A.4, and A.6. Grey shaded areas denote the standard deviations σ_{Λ_w} , $\sigma_{\Lambda_{\theta_v}}$, and σ_{Λ_q} .

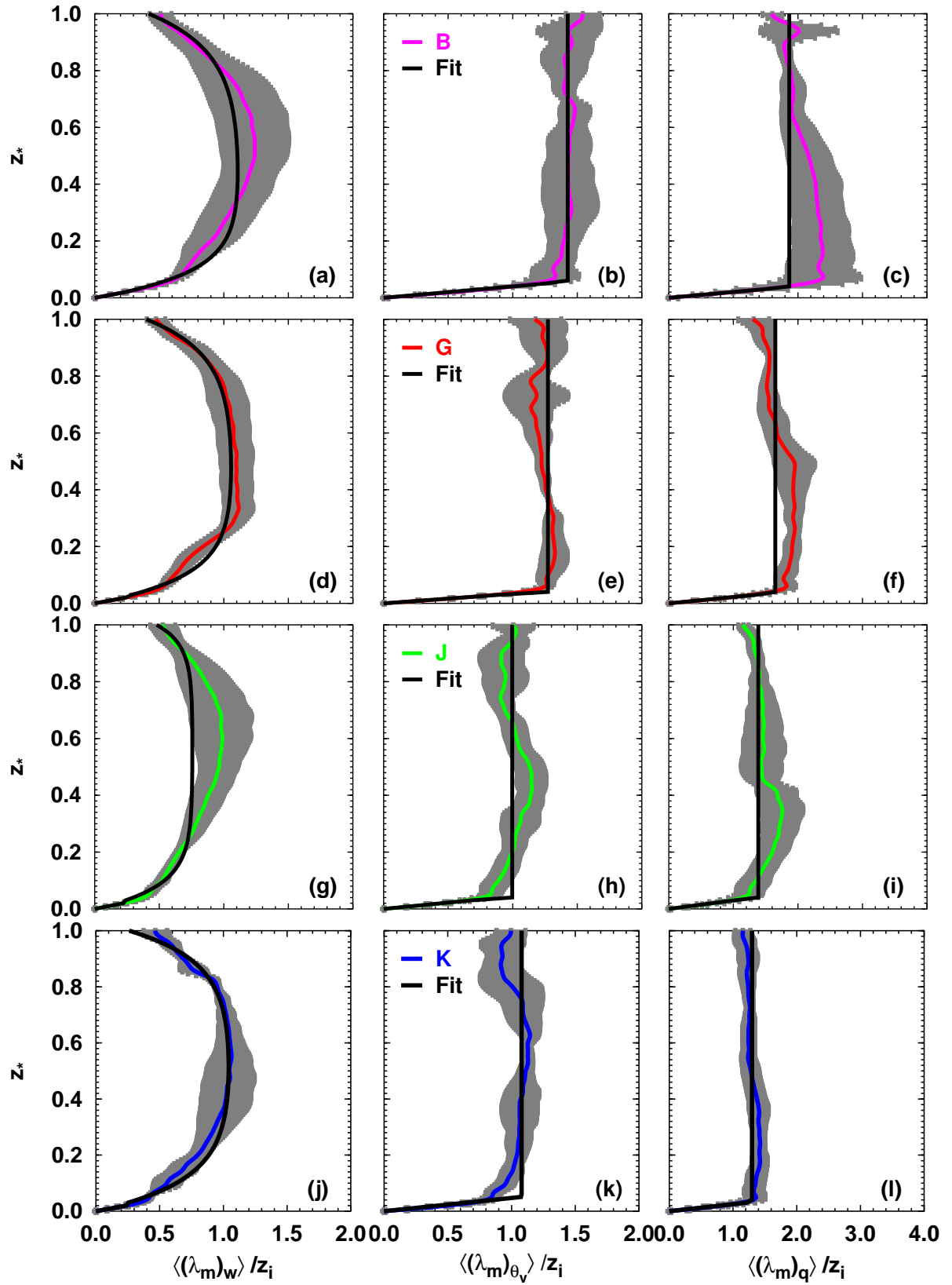


FIGURE B.1:

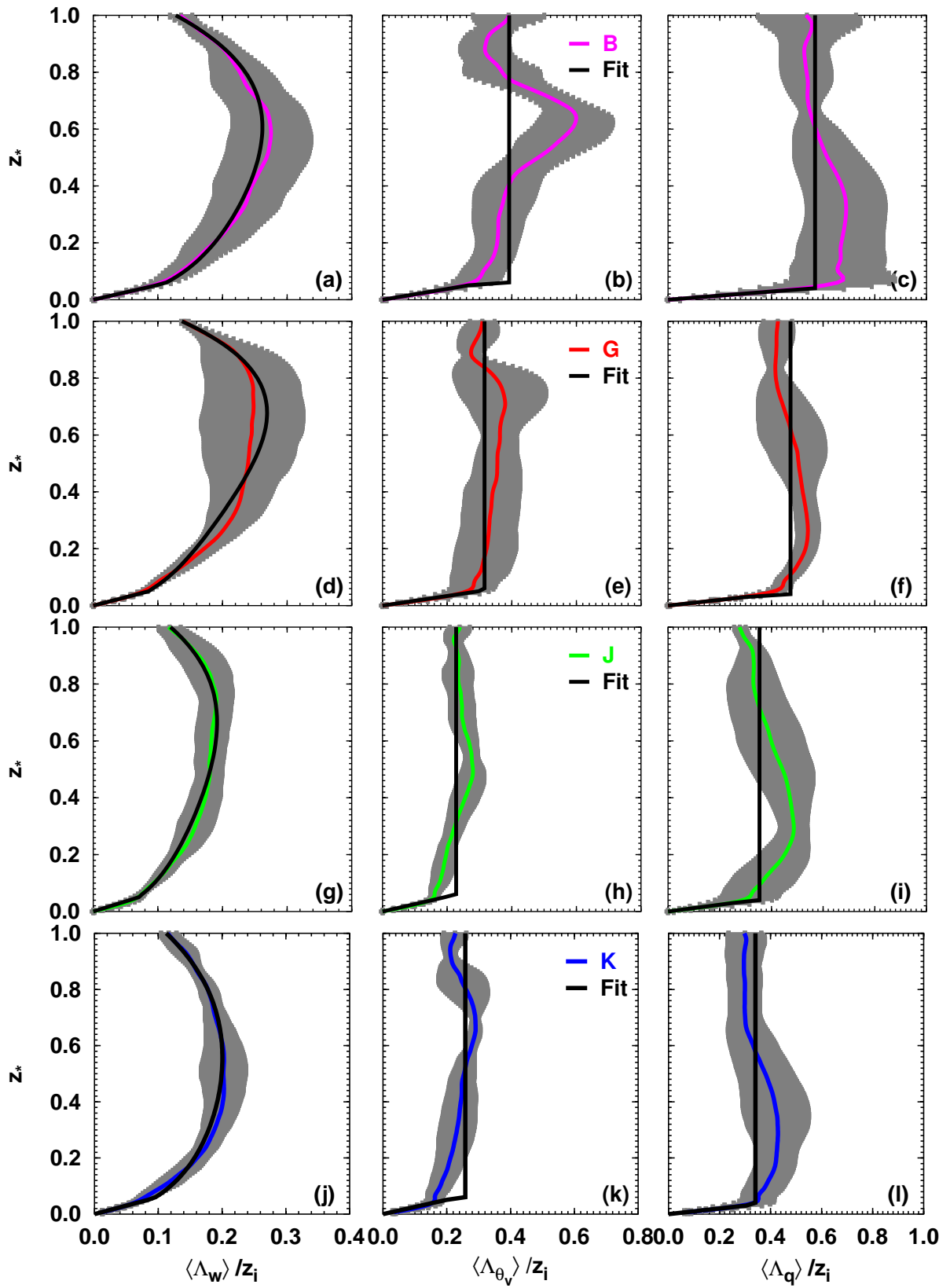


FIGURE B.2:

Nomenclature

Greek Letters

α	wind direction	γ_ϕ	counter-gradient eddy diffusivity
β	Bowen ratio	Γ_{θ_l}	lapse rate of liquid water potential temperature
χ	flow variable	κ	von-Karman constant
χ_r	statistical parameter	Λ_1	particular length scale of the MY-model
$\Delta\delta^{\text{CP}}$	difference of centred pattern root-mean-square difference	Λ_2	particular length scale of the MY-model
$\Delta\rho$	difference of correlation coefficient	Λ_χ	integral length scale of a flow variable
Δt	time step	λ_m	peak wavelength
Δx	zonal grid resolution	ν	fluid viscosity
Δy	meridional grid resolution	ϕ	scalar variables
Δz	vertical grid resolution	ϕ'	subgrid-scale fluctuations of scalar variables
$\Delta\theta_l$	temperature jump at initial boundary layer height	Φ_M	general stability function
δ	Kronecker symbol	Φ_{χ_i}	Fourier transform of variable χ_i
$\delta\alpha_{A,B}$	mean deviation of wind direction	π_E	Exner function
$\delta_{A,B}^{\text{CP}}$	centred pattern root-mean-square difference of two-dimensional fields	σ_χ	standard deviation of a flow variable
ε	dissipation	τ_{ij}	residual stress tensor
ε_m	model dissipation rate	θ	potential temperature
η	Kolmogorov length scale	θ_l	liquid water potential temperature
$\Gamma_\theta^>$	lapse rate of potential temperature above CBL top within the entrainment zone	θ_v	virtual potential temperature
		θ_*	mixed layer convective temperature scale
		$\theta_{v,s}$	virtual potential temperature of near surface air

$\rho_{A,B}$	correlation coefficient of two-dimensional fields	E_χ^y	meridional spectral energy of a flow variable
Roman Letters		E_χ	spectral energy of a flow variable
l	size of a coherent turbulent region (eddy)	e_χ	turbulent energy of a flow variable
l_0	length scale of energy-containing range	f	Coriolis parameter
l_ε	dissipation length scale	F_1	stability expression
l_k	turbulent mixing length scale	F_2	stability expression
l_{ε_χ}	dissipation length scale of a flow variable	F_3	stability expression
ε_χ	dissipation of a flow variable	F_4	stability expression
\mathcal{C}_{ij}	cross stress tensor	g	earth acceleration
\mathcal{L}_{ij}	Leonard stress tensor	G_M	stability expression of momentum
\mathcal{R}_{ij}	Reynolds stress tensor	G_M	stability expression of scalars
A	two-dimensional mesoscale field	k	wavenumber
A_χ	structure parameter of a flow variable	K_χ	eddy diffusivity of flow variable χ
a_i	fit parameter	K_ϕ	eddy diffusivity for scalars
B	constant of relationship for peak wavenumber	K_M	eddy diffusivity for momentum
B	two-dimensional mesoscale field	k_m	peak wavenumber
C_χ	Kolmogorov constant	L	length scale of the flow
c_p	specific heat at constant pressure	l	master length scale of the MY-model
E	model turbulent kinetic energy	l_0	asymptotic length scale
e	residual kinetic energy	L_1	first dual-choice length scale
E_χ^B	Bezier approximated spectral energy of a flow variable	l_1	particular length scale of the MY-model
E_χ^x	zonal spectral energy of a flow variable	L_2	second dual-choice length scale
		l_2	particular length scale of the MY-model
		l_{down}	downward displacement
		l_{up}	upward displacement

L_D	model domain size in one direction	r	displacement
L_S	structure wavelength	$R_{A,X}^{CLCL}$	covariance of low cloud coverage
L_V	latent heat of vaporisation of water	R_{χ}^x	zonal auto-covariance of a flow variable
L_x	zonal model domain size	R_{χ}^y	meridional auto-covariance of a flow variable
L_y	meridional model domain size	R_1	stability expression
L_z	vertical model domain size	R_d	gas constant
$l_{\sigma_z^2}$	averaging length of a flow variable	r_x	zonal displacement
L_{MO}	Monin-Obukhov length scale	r_y	meridional displacement
M	index of fit parameters	$R_{\chi_i \chi_i}$	auto-covariance of a flow variable
N_a	number of parameters	$R_{\chi_i \chi_j}$	covariance of two flow variables
N_D	number of model gridpoints in one direction	S_{ϕ}	stability function for scalars
n_D	number of degrees of freedom	S_E	stability function for turbulent kinetic energy
N_x	zonal number of gridpoints	S_M	stability function for momentum
N_y	meridional number of gridpoints	T	temperature
p	pressure	t_*	convective time scale
p_0	initial pressure	$T_{2\text{ m}}$	2 m-temperature
P_b	buoyancy production	t_{av}	averaging time
P_s	shear production	t_{max}	time of finish of averaging process
Q	goodness-of-fit	t_{min}	time of start of averaging process
q	total water content	T_{IR}	infrared equivalent brightness temperature
q_*	mixed layer convective humidity scale	$T_{MAX_{2\text{ m}}}$	2 m-current maximum temperature
q_c	cloud-water content	$T_{MIN_{2\text{ m}}}$	2 m-current minimum temperature
q_l	liquid water content	T_{WV}	water vapour equivalent brightness temperature
q_v	water vapour content		
q_{v_s}	specific moisture at surface		

$T_{d_{2\text{m}}}$	2 m-dew point temperature	$q^>$	total water content above the initial boundary layer height
U	wind speed	Re	Reynolds number
u	vertical wind	Ri	local gradient Richardson number
u	zonal wind	Constants	
u_*	friction velocity	$A_1 =$	0.92
$U_{10\text{ m}}$	10 m-horizontal wind velocity	$A_2 =$	16.6
$u_{10\text{ m}}$	10 m-zonal wind velocity	$B_1 =$	0.74
u_g	zonal geostrophic wind	$B_2 =$	10.1
u_i	velocity components	$C =$	0.24 ± 0.04
u'_i	subgrid-scale fluctuations of velocity components	$c_0 =$	5.9
v	meridional wind	$C_1 =$	0.08
$v_{10\text{ m}}$	10 m-meridional wind velocity	$c_1 =$	1.8
v_g	meridional geostrophic wind	$c_2 =$	4.0
w_*	convective velocity scale	$c_3 =$	0.0003
w_{LS}	large scale subsidence	$c_4 =$	8.0
x	cartesian coordinate	Abbreviations	
y	cartesian coordinate	1D	one dimensional
z	cartesian coordinate	2D	two dimensional
z_*	normalised height	3D	three dimensional
z_0	roughness length	4D	four dimensional
z_B	height of cloud base	CBL	convective boundary layer
z_T	inversion height above cloud top	CLC	cloud coverage
$z_{i,0}$	initial boundary layer height	CLCH	cloud coverage of high clouds
$q^<$	total water content below the initial boundary layer height	CLCL	cloud coverage of low clouds
		CLCM	cloud coverage of medium clouds

DNS	direct numerical simulation	PRR-CON	precipitation rate of convective precipitation
DWD	Deutscher Wetterdienst	PRR-GSP	precipitation rate of gridscale precipitation
GCM	general circulation model	RAIN-CON	amount of rain from convective precipitation
IFT	Leibniz-Institut für Troposphärenforschung	RAIN-GSP	amount of rain from gridscale precipitation
LES	large-eddy simulation	RIM	regional integrated model
LITFASS	Lindenberg Inhomogeneous Terrain - Fluxes between Atmosphere and Surface: a longterm Study	SEMAPHORE	Structure des Echanges Mer-Atmosphere, Proprietes des Heterogeneites Oceaniques: Recherche Experimentale
LLM	Lindenberger Lokal-Modell	SGS	subgrid scale
LM	non-hydrostatic limited area model	Tab.	Table
LT	look-up table	TKE	turbulent kinetic energy
LT-TML	look-up table turbulent mixing length formulation	TMLF	turbulent mixing length formulation
LWC	liquid water content	TMLS	turbulent mixing length scale
MCBL	marine convective boundary layer	TOT-PREC	amount of rain from total precipitation
MM	mesoscale model	TWC	total water content
MOL	Meteorological Observatory Lindenberg	UTC	universal time
MPI	Max-Planck Institute		
MY	local closure approximation of order 1 1/2 after Mellor and Yamada (1974) and Mellor and Yamada (1982)		
MY-TML	turbulent mixing length formulation of Mellor and Yamada (1974) and Blackadar (1962)		
MY25	Level 2.5 local closure approximation of order 1 1/2 after Mellor and Yamada (1974) and Mellor and Yamada (1982)		
NWP	numerical weather prediction		
PBL	planetary boundary layer		

List of Figures

2.1	Characteristic spatial and temporal scales of atmospheric processes and corresponding atmospheric models with varying scale of interest.	10
3.1	Time evolution of vertically integrated total (resolved+subgrid) TKE (case K). . .	28
3.2	Vertical profiles of mean LES flow variables of the subset simulation cases. . . .	33
3.3	Vertical profiles of averaged normalised LES variances of the subset simulation cases.	35
3.4	Vertical profiles of averaged turbulent fluxes of the subset simulation cases. . . .	37
3.5	LES domain of case K.	38
3.6	Horizontal cross sections of the LES domain at various CBL levels indicating fluctuations of LES flow variables.	39
3.7	Two-dimensional normalised auto-covariances based on turbulent fluctuations of LES flow variables, shown in Fig. 3.6.	40
3.8	Wavenumber weighted averaged normalised 1D energy spectra in various LES model levels.	42
3.9	Ratio of peak wavelengths related to different sampling pathways.	43
3.10	Horizontally averaged peak wavelengths derived from a subset of LES.	44
3.11	Averaged normalised mean 1D auto-covariances of subset simulations in various LES model levels.	46
3.12	Horizontally averaged integral length scales derived from a subset of LES	48
3.13	Ratio of integral length scales related to different sampling pathways.	49
3.14	Ratio of peak wavelength to integral length scale.	50
3.15	Integral length scales based on LES data of Khanna and Brasseur (1998) (KB98) and LES cases I, II, III, and D.	52
3.16	Peak wavelength based on LES of Graf and Schumann (1991) (GS91) and LES case B.	53
3.17	Mean flow variables of SEMAPHORE and LES case IV.	54
3.18	Comparison of peak wavelength and integral length scale based on observations during SEMAPHORE, integral length scale approximation and LES case IV. . . .	55
3.19	Peak wavelength based on measurements and LES case B.	56
3.20	Peak wavelengths based on wind tunnel measurements and LES cases B, C, and D. .	57
3.21	Vertical profiles of the stability functions of momentum and scalars.	60
3.22	Vertical profiles of turbulent mixing lengths and eddy diffusivity coefficients. . .	61

3.23	Turbulent fluxes, derived from LES cases, based on the Mellor-Yamada model, and based on present model containing LES-derived look-up table of turbulent mixing length.	62
3.24	Normalised variances, derived from LES cases, based on Mellor-Yamada model, and based on present model containing LES-derived look-up table of turbulent mixing length.	64
4.1	Generalised terrain following model layers of the Lokal-Modell (LM).	66
4.2	Surface weather chart (Berliner Wetterkarte) of the 18 June 1998 at 00:00 UTC.	67
4.3	LITFASS LM domain of RUN I, at 18.06.1998 00:00 UTC and at 12:00 UTC.	69
4.4	Time evolution of sensible and latent heat flux of LITFASS simulations RUN I and RUN II.	70
4.5	Time evolution of correlation coefficient and centred pattern root-mean-square difference determined from simulations RUN I and RUN II for model cloudiness, cloud water content, and water vapour.	71
4.6	Time evolution of correlation coefficient and centred pattern root-mean-square difference determined from simulations RUN I and RUN II for RAIN-CON, RAIN-GSP, TOT-PREC, PRR-CON, and PRR-GSP.	73
4.7	Verification of LITFASS simulations against METEOSAT observations.	75
4.8	Coverage with low clouds (CLCL) at 12:00 UTC determined from analysis data and from LITFASS simulations.	79
4.9	Normalised 2D covariance of coverage with low clouds based on model analysis database and LITFASS simulations.	79
B.1	Horizontally averaged peak wavelength of LES flow variables of subset LES together with fit approximations.	91
B.2	Horizontally averaged integral length scale of LES flow variables of subset LES together with fit approximations.	91

List of Tables

3.1	Initial parameters of the large-eddy simulations	27
3.2	LES boundary layer properties	30
3.3	Boundary layer properties based on LES data of Graf and Schumann (1991) (GS91), Khanna and Brasseur (1998) (KB98), and LES cases I to III, D and B . . .	51
3.4	Marine boundary layer properties based on observations during the SEMAPHORE campaign (Lambert and Durand, 1999; Lambert <i>et al.</i> , 1999; Durand <i>et al.</i> , 2000) and LES case IV	54
3.5	Boundary layer properties based on wind tunnel measurements and LES cases B, C, and D	56
4.1	Observed synoptic conditions during LITFASS (18.06.1998) at measurement site Berlin-Dahlem (52.28° N, 13.18° E)	68
4.2	Verification of LITFASS simulations against METEOSAT observations	76
4.3	Verification of LITFASS simulations against analysis data	77
A.1	Parameter set for approximation of $\langle(\lambda_m)_w\rangle$	85
A.2	Parameter set for approximation of $\langle\Lambda_w\rangle$	86
A.3	Parameter set for approximation of $\langle(\lambda_m)_{\theta_v}\rangle$	87
A.4	Parameter set for approximation of $\langle\Lambda_{\theta_v}\rangle$	88
A.5	Parameter set for approximation of $\langle(\lambda_m)_q\rangle$	89
A.6	Parameter set for approximation of $\langle\Lambda_q\rangle$	90

Bibliography

Abdalla, K. and McFarlane, N. (1997) A new-second order turbulence closure scheme for the planetary boundary layer. *J. Atmos. Sci.* **54**, 1850–1867.

Ahlers, G.; Xu, X. (2001) Prandtl-number dependence of heat transport in turbulent Rayleigh-Benard convection. *Phys. Rev. Lett.* **86**, 3320–3323.

Alekseev, V., Dymnikov, V., Galin, V., Volodin, E. M., Barker, H. W., Cess, R. D., Zhang, M. H., CohenSolal, E., LeTreut, H., Colman, R. A., Fraser, J. R., McAvaney, B. J., Dazlich, D. A., Fowler, L. D., Randall, D. A., DelGenio, A. D., Lo, K. K. W., Dix, M. R., Esch, M., Roeckner, E., Gates, W. L., Potter, G. L., Taylor, K. E., Hack, J. J., Ingram, W. J., Kiehl, J. T., Royer, J. F., Timbal, B., Meleshko, V. P., Sporyshev, P. V., Morcrette, J. J., Schlesinger, M. E., Wang, W., and Wetherald, R. T. (1996) Cloud feedback in atmospheric general circulation models: An update. *J. Geophys. Res.* **101**, 12791–12794.

André, J.-C., Moor, G. D., Lacarrère, P., Therry, G., and du Vachat, R. (1978) Modeling the 24-hour evolution of the mean and turbulent structures of the planetary boundary layer. *J. Atmos. Sci.* **35**, 1861–1883.

Andrén, A., Brown, A. R., Graf, J., Mason, P. J., Moeng, C.-H., Nieuwstadt, F. T. M., and Schumann, U. (1994) Large-eddy simulation of a neutrally stratified boundary layer: A comparison of four computer codes. *Quart. J. R. Meteorol. Soc.* **120**, 1457–1484.

Arritt, R. W. (1987) The effect of water surface temperature on lake breezes and thermal internal boundary layers. *Boundary-Layer Meteorology* **40**, 101–125.

Ayotte, K. W., Sullivan, P. P., Andrén, A., Doney, S. C., Holtslag, A. A. M., Large, W. G., McWilliams, J. C., Moeng, C.-H., Otte, M. J., Tribbia, J. J., and Wyngaard, J. C. (1996) An evaluation of neutral and convective planetary boundary-layer parameterizations relative to large eddy simulations. *Boundary-Layer Meteorology* **79**, 131–175.

Balzer, K., Buchhold, M., Damrath, U., Paul, G., Hanisch, T., Hess, R., Kirchner, R., Majewski, D., Rühland, D., Vogel, G., and Wergen, W. (2001) Quarterly Report of the Operational NWP-Models of the Deutscher Wetterdienst 27, Deutscher Wetterdienst, Business Area Research and Development.

Batchelor, G. K. (1953) *The theory of homogeneous turbulence*. Cambridge University Press, Cambridge.

- Bélair, S., Mailhot, J., Strapp, J. W., and MacPherson, J. I. (1999) An examination of local versus nonlocal aspects of a TKE-based boundary layer scheme in clear convective conditions. *J. Appl. Met.* **38**, 1499–1518.
- Beniston, M. (1998) *From Turbulence to Climate: Numerical Investigations of the Atmosphere with a Hierarchy of Models*. Springer-Verlag, Berlin, Heidelberg.
- Berkowicz, R. (1984) Spectral methods for atmospheric diffusion modelling. *Boundary-Layer Meteorology* **30**, 201–220.
- Beyrich, F. (2001) *Zusammenfassung der Ergebnisse aus dem Projekt LITFASS: Lindenberg Inhomogeneous Terrain - Fluxes between Atmosphere and Surface: a long-term study*. Arbeitsergebnisse 70, Deutscher Wetterdienst- Forschung und Entwicklung.
- Blackadar, A. K. (1962) The vertical distribution of wind and turbulent exchange in a neutral atmosphere. *J. Geophys. Res.* **67**, 3095–3102.
- Bonnert, E. (2003) Auf dem Chip Gipfel – ISSCC 2003: Leistung zählt. *c't Magazin für Computertechnik* **5**. Available at <http://www.heise.de/ct/03/05/018/>.
- Bott, A. (1989a) A positive definite advection scheme obtained by non-linear normalization of the advective fluxes. *Mon. Wea. Rev.* **117**, 1006–1015.
- Bott, A. (1989b) Reply. *Mon. Wea. Rev.* **117**, 2633–2636.
- Bougeault, P. and Lacarrère, P. (1989) Parameterization of orography-induced turbulence in a mesobeta-scale model. *Mon. Wea. Rev.* **117**, 1872–1890.
- Brown, A. and Grant, A. (1997) Non-local mixing of momentum in the convective boundary layer. *Boundary-Layer Meteorology* **84**, 1–22.
- Brown, A. R., Cederwall, T., Chlond, A., Duynkerke, P. G., Golaz, J.-C., Khairoutdinov, M., Lewellen, D. C., Lock, A. P., Macvean, M. K., Moeng, C.-H., Neggers, R. A., Siebesma, A. P., and Stevens, B. (2002) Large-eddy simulation of the diurnal cycle of shallow cumulus convection over land. *Quart. J. R. Meteorol. Soc.* **128**, 1075–1093.
- Bösenberg, J. (1998) Ground-based differential absorption lidar for water-vapor and temperature profiling: Methodology. *Appl. Opt.* **37**, 3845–3860.
- Busch, N. E. and Larsen, S. E. (1972) *Spectra of turbulence in the atmospheric surface layer*. Riso Report 256.
- Caughey, S. J. and Palmer, S. G. (1979) Some aspects of turbulence structure through the depth of the convective boundary layer. *Quart. J. R. Meteorol. Soc.* **105**, 811–827.
- Cheng, Y., Canuto, V. M., and Howard, M. (2002) An improved model for the turbulent PBL. *J. Atmos. Sci.* **59**, 1550–1565.

- Chlond, A. (1992) Three-dimensional simulation of cloud street development during a cold air outbreak. *Boundary-Layer Meteorology* **58**, 161–200.
- Chlond, A. (1994) Locally modified version of Bott's advection scheme. *Mon. Wea. Rev.* **122**, 111–125.
- Chlond, A. (1999) *Grobstruktursimulation - Eine Methode zur Berechnung turbulenter atmosphärischer Strömungen*. Max-Planck-Institut für Meteorologie, Hamburg.
- Chlond, A. and Wolkau, A. (2000) Large-eddy simulation of a nocturnal stratocumulus-topped marine atmospheric boundary layer: An uncertainty analysis. *Boundary-Layer Meteorology* **95**, 31–55.
- Chrobok, G., Raasch, S., and Etling, D. (1992) A comparison of local and nonlocal turbulence closure methods for the case of a cold air outbreak. *Boundary-Layer Meteorology* **58**, 69–90.
- Corrsin, S. (1951) On the spectrum of isotropic temperature fluctuations in an isotropic turbulence. *J. Appl. Phys.* **22**, 469–473.
- Cuijpers, J. W. M. and Holtslag, A. A. M. (1998) Impact of skewness and nonlocal effects on scalar and buoyancy fluxes in convective boundary layers. *J. Atmos. Sci.* **55**, 151–162.
- Deardorff, J. W. (1970a) Convective velocity and temperature scales for the unstable boundary layer. *J. Atmos. Sci.* **27**, 1211–1213.
- Deardorff, J. W. (1970b) A numerical study of the three-dimensional channel flow at large Reynolds numbers. *J. Fluid Mech.* **41**, 453–480.
- Deardorff, J. W. (1972) Theoretical expressions for the counter-gradient vertical heat flux. *J. Geophys. Res.* **77**, 5900–5904.
- Deardorff, J. W. (1973) The use of subgrid transport equations in a three-dimensional model of atmospheric turbulence. *J. Fluids Eng.* **95**, 429–438.
- Deardorff, J. W. (1974) Three-dimensional numerical study of the height and mean structure of a heated planetary boundary layer. *Boundary-Layer Meteorology* **7**, 81–106.
- Deardorff, J. W. (1980) Stratocumulus-capped mixed layers derived from a three-dimensional model. *Boundary-Layer Meteorology* **18**, 495–527.
- Degrazia, G. A., Velho, H. F. C., and Carvalho, J. C. (1997) Nonlocal exchange coefficients for the convective boundary layer derived from spectral properties. *Contr. Atmos. Phys.* **70**, 57–64.
- Doms, G., Gassmann, A., Heise, E., Raschendorfer, M., Schraff, C., and Schrodin, R. (2002) Parameterization issues in the non-hydrostatic NWP-Model LM. In *ECMWF Seminar Proceedings: Key Issues in the Parameterization of Subgrid Physical Processes*. Available at <http://www.cosmo-model.org/>.

- Doms, G. and Schättler, U. (1999) *The nonhydrostatic limited-area model LM (Lokal-Modell) of DWD*. Tech. Rep. Part I: Scientific Documentation, Deutscher Wetterdienst, Geschäftsbereich Forschung und Entwicklung. Available at <http://www.cosmo-model.org/>.
- Doms, G., Schättler, U., Steppeler, J., and Wicker, L. (1998) Development of the nonhydrostatic regional model LM at DWD. *Research Activities in Atmospheric and Oceanic Modelling* **27**, 5.17–5.18.
- Druilhet, A. and Durand, P. (1997) Experimental investigation of atmospheric boundary layer turbulence. *Atmospheric Research* **43**, 345–388.
- Dubrulle, B. and Niino, H. (1992) On a diagnostic equation for a turbulent length scale. In *Autumn Conference of Japan Meteorological Society*, pp. 214–214. Japan Meteorological Society.
- Durand, P., Thoumieux, F., and Lambert, D. (2000) Turbulent length-scales in the marine atmospheric mixed layer. *Quart. J. R. Meteorol. Soc.* **126**, 1889–1912.
- Duynkerke, P. G. and Driedonks, A. G. M. (1987) A model for the turbulent structure of the stratocumulus topped atmospheric boundary layer. *J. Atmos. Sci.* **44**, 43–64.
- Ebert, E. E., Schumann, U., and Stull, R. B. (1989) Nonlocal turbulent mixing in the convective boundary layer evaluated from large-eddy simulation. *J. Atmos. Sci.* **46**, 2178–2207.
- EUMETSAT (2000) *The METEOSAT system*. EUMETSAT – European Organisation for the Exploitation of Meteorological Satellites. Available at <http://www.eumetsat.de/>.
- Fiedler, B. H. and Moeng, C.-H. (1985) A practical integral closure model for mean vertical transport of a scalar in a convective boundary layer. *J. Atmos. Sci.* **42**, 359–363.
- Frisch, U. (1995) *Turbulence; The legacy of A.N. Kolmogorov*. Cambridge University Press.
- Galperin, B. and Orszag, S. A., editors (1993) *Large-eddy simulation of complex engineering and geophysical flows*. Cambridge University Press.
- Garrat, J. (1993) Sensitivity of climate simulations to land-surface and atmospheric boundary layer treatment: a review. *J. Climate* **6**, 419–449.
- Gibson, G. and Wielicki, B. A. (2002) *CERES – Clouds and the earth's radiant energy system*. NASA Langley Research Center. Available at <http://asd-www.larc.nasa.gov/ceres/ASDCeres.html>.
- Gossard, E. (1960) Power spectra of temperature, humidity and refractive index from aircraft and tethered balloon measurements. *IRE Trans. Antennas Propag.* **AP-8(2)**, 186–201.
- Graf, J. and Schumann, U. (1991) Simulation der konvektiven Grenzschicht im Vergleich mit Flugzeugmessungen beim LOTREX-Experiment. *Meteorol. Rdsch.* **43**, 140–148.

- Grossmann, S. and Lohse, D. (2001) Thermal convection for large Prandtl numbers. *Phys. Rev. Lett.* **86**, 3316–3319.
- Harrison, E., Minnis, P., Barkstrom, B., Ramanathan, V., Cess, R., and Gibson, G. (1990) Seasonal variation of cloud radiative forcing derived from the earth radiation budget experiment. *J. Geophys. Res.* **95**, 18687–18703.
- Heide, B. (2003) *Verifikation von LM-Bewölkungsvorhersagen anhand von METEOSAT Satellitenbildern*. Diploma thesis, Universität Leipzig.
- Hellmuth, O. (2000) Diagnostic determination of mixing layer height and entrainment layer thickness in the convective boundary layer using a spectral entraining jet model. *Meteorologische Zeitschrift* **9**, 283–298.
- Hellmuth, O., Heide, B., and Vogel, G. (2002) *Model-to-satellite approach for cloud verification using the Local Model (LM)*. Biennial report 2001/2002, Leibnitz-Institute for Tropospheric Research.
- Hellmuth, O. and Helmert, J. (2002) Parameterization of turbulence-enhanced nucleation in large scale models: conceptual study. In *Air Pollution Modeling and Its Application XV* (Edited by Borrego, C. and Schayes, G.), Proceedings of twenty-fifth NATO/CCMS international technical meeting on air pollution modeling and its application. Kluwer Academic/ Plenum Publishers, New York.
- Helmert, J. (1999) *Zur Parameterisierung der Mächtigkeit der Entrainmentschicht unter Verwendung von Large Eddy Simulations- und LIDAR-Daten*. Diploma thesis, Universität Leipzig.
- Helmert, J. and Hellmuth, O. (2000) *On the influence of large-eddy simulation (LES)-based turbulence parameters on mesoscale cloud forecast*. Biennial report 1999/2000, Leibnitz-Institute for Tropospheric Research.
- Helmert, J. and Hellmuth, O. (2002) *On the impact of turbulence length-scales, derived from large-eddy simulations on predicted mesoscale fields using the "Lokal-Modell"*. Biennial report 2001/2002, Leibnitz-Institute for Tropospheric Research. In press.
- Helmert, J. and Hellmuth, O. (2003) Revised mixing length parametrization for the convective boundary layer from large-eddy simulation. *Quart. J. R. Meteorol. Soc.* Submitted.
- Herzog, H.-J., Schubert, U., and Vogel, G. (1998) LLM - ein wesentliches Teilprojekt des DWD-Projektes LITFASS. In *Annalen der Meteorologie*, vol. 37, pp. 469–470. Deutsche Meteorologen-Tagung, Deutscher Wetterdienst, Offenbach am Main.
- Herzog, H.-J., Schubert, U., Vogel, G., Fiedler, A., and Kirchner, R. (2002a) *LLM - the High-Resolving Nonhydrostatic Simulation Model in the DWD - Project LITFASS (Part I: Modelling Technique and Simulation Method)*. COSMO Technical Report 4. Available at <http://www.cosmo-model.org/>.

- Herzog, H.-J., Vogel, G., and Schubert, U. (2002b) LLM - a nonhydrostatic model applied to high-resolving simulations of turbulent fluxes over heterogeneous terrain. *Theor. Appl. Clim.* **73**. In press.
- Højstrup, J. (1982) Velocity spectra in the unstable boundary layer. *J. Atmos. Sci.* **39**, 2239–2248.
- Holt, T. and Raman, S. (1988) A review and comparative evaluation of multilevel boundary layer parameterizations for first-order and turbulent kinetic energy closure schemes. *Rev. Geophys.* **26**, 761–780.
- Holton, J. R. (1972) *An Introduction to Dynamic Meteorology*. Academic Press, New York.
- Holtslag, A. A. M. and Boville, B. A. (1993) Local versus nonlocal boundary-layer diffusion in a global climate model. *J. Climate* **6**, 1825–1842.
- Holtslag, A. A. M. and Moeng, C.-H. (1991) Eddy diffusivity and countergradient transport in the convective atmospheric boundary layer. *J. Atmos. Sci.* **48**, 1690–1698.
- Holtslag, A. A. M. and Nieuwstadt, F. T. M. (1986) Scaling the atmospheric boundary layer. *Boundary-Layer Meteorology* **25**, 990–1001.
- Holtslag, A. A. M., van Meijgaard, E., and Rooy, W. C. D. (1995) A comparison of boundary layer diffusion schemes in unstable conditions over land. *Boundary-Layer Meteorology* **76**, 69–95.
- IPCC (2002) *Climate Change 2001. The third assessment report of the IPCC*. IPCC- International Panel on Climate Change. Cambridge University Press: Cambridge, New York, Melbourne.
- Jacobsen, I. and Heise, E. (1982) A new economic method for the computation of the surface temperature in numerical models. *Contr. Atmos. Phys.* **55**, 128–141.
- Janjić, Z. I. (2001) *Nonsingular Implementation of the Mellor-Yamada Level 2.5 Scheme*. Office Note 437, National Centers for Environmental Prediction.
- Jonker, H. J. J., Duynkerke, P. G., and Cuijpers, J. W. M. (1997) Energy spectra in the mesoscale range: An LES study. In *Proc. 12th Symp. on Boundary Layers and Turbulence*, pp. 225–226. Amer. Meteor. Soc., Vancouver, BC, Canada.
- Jonker, H. J. J., Duynkerke, P. G., and Cuijpers, J. W. M. (1999) Mesoscale fluctuations generated by boundary layer convection. *J. Atmos. Sci.* **56**, 801–808.
- Kaimal, J. C. and Finnigan, J. J. (1994) *Atmospheric Boundary Layer Flows. Their Structure and Measurement*. Oxford University Press.

- Kaimal, J. C., Wyngaard, D. A., Haugen, D. A., Coté, O. R., Izumi, Y., Caughey, S. J., and Readings, C. J. (1976) Turbulence structure in the convective boundary layer. *J. Atmos. Sci.* **33**, 2152–2169.
- Kaimal, J. C., Wyngaard, D. A., Izumi, Y., and Coté, O. R. (1972) Spectral characteristics of surface-layer turbulence. *Quart. J. R. Meteorol. Soc.* **98**, 563–589.
- Kaiser, R. (1996) *Windkanalstudie konvektiver Grenzschichtströmungen mit angehobener Temperaturinversion*. Ph.D. thesis, Institut für Hydrologie und Wasserwirtschaft, Universität Karlsruhe (TH).
- Kaiser, R. and Fedorovich, E. (1998) Turbulence spectra and dissipation rates in a wind tunnel model of the atmospheric convective boundary layer. *J. Atmos. Sci.* **55**, 580–594.
- Keller, L. V. and Friedman, A. A. (1924) Differentialgleichung für die turbulente Bewegung einer kompressiblen Flüssigkeit. In *Proc. 1st Intern. Congr. Appl. Mech., Delft*, pp. 395–405.
- Kershaw, R. and Gregory, D. (1997) Parametrization of momentum transport by convection i: Theory and cloud modelling results. *Quart. J. R. Meteorol. Soc.* **123**, 1133–1151.
- Khanna, S. and Brasseur, J. G. (1998) Three-dimensional buoyancy- and shear-induced local structure of the atmospheric boundary layer. *J. Atmos. Sci.* **55**, 710–743.
- Klemp, J. and Wilhelmson, R. (1978) The simulation of three-dimensional convective storm dynamics. *J. Atmos. Sci.* **35**, 1070–1096.
- Kolmogorov, A. N. (1941) The local structure of turbulence in incompressible viscous fluid for very large Reynolds numbers. *Dokl. Akad. Nauk SSSR* **30**, 299–303.
- Lambert, D. and Durand, P. (1999) The marine atmospheric boundary layer during SEMAPHORE. I: Mean vertical structure and non-axisymmetry of turbulence. *Quart. J. R. Meteorol. Soc.* **125**, 495–512.
- Lambert, D., Durand, P., Thoumieux, F., Bénech, B., and Druilhet, A. (1999) The marine atmospheric boundary layer during SEMAPHORE. II: Turbulence profiles in the mixed layer. *Quart. J. R. Meteorol. Soc.* **125**, 513–528.
- Lenschow, D. H., Mann, J., and Kristensen, L. (1994) How long is long enough when measuring fluxes and other turbulence statistics? *J. Atmos. Oceanic Technol.* **11**, 661–673.
- Lenschow, D. H. and Stankov, B. B. (1986) Length scales in the convective boundary layer. *J. Atmos. Sci.* **43**, 1189–1209.
- Lenschow, D. H., Wulfmeyer, V., and Senff, C. (2000) Measuring second- through fourth-order moments in noisy data. *J. Atmos. Ocean. Tech.* **17**, 1330–1347.
- Leonard, A. (1974) Energy cascade in large-eddy simulations of turbulent fluid flows. *Adv. Geophys.* **18 A**, 237–248.

- Lesieur, M. (1990) *Turbulence in Fluids*. 2nd Edition. Kluwer, Dordrecht.
- Lin, C.-L., McWilliams, J. C., Moeng, C.-H., and Sullivan, P. P. (1996) Coherent structures and dynamics in a neutrally stratified planetary boundary layer flow. *Phys. Fluid* **8**, 2626–2639.
- Lohou, F., Campistron, B., Druilhet, A., Foster, P., and Pages, J. P. (1998) Turbulence and coherent organizations in the atmospheric boundary layer: a radar-aircraft experimental approach. *Boundary-Layer Meteorology* **86**, 147–179.
- Lohou, F., Druilhet, A., Campistron, B., Redelsperger, J.-L., and Saïd, F. (2000) Numerical study of the impact of coherent structures on vertical transfers in the atmospheric boundary layer. *Boundary-Layer Meteorology* **97**, 361–383.
- Louis, J.-F. (1979) A parametric model of vertical eddy fluxes in the atmosphere. *Boundary-Layer Meteorology* **17**, 187–202.
- Lüpkes, C. and Schlünzen, K. H. (1996) Modelling the arctic convective boundary-layer with different turbulence parameterizations. *Boundary-Layer Meteorology* **79**, 107–130.
- Lumley, J. L. and Panofsky, H. A. (1964) *The structure of atmospheric turbulence*. John Wiley & Sons.
- Mailhot, J. and Benoit, R. (1982) A finite-element model of the atmospheric boundary layer suitable for use with numerical weather prediction models. *J. Atmos. Sci.* **39**, 2249–2266.
- Marquardt, D. W. (1963) An algorithm for least squares estimation of nonlinear parameters. *SIAM J. Appl. Math.* **11**, 431–441.
- Mason, P. J. (1989) Large-eddy simulation of the convective atmospheric boundary layer. *J. Atmos. Sci.* **46**, 1492–1516.
- Mason, P. J. and Brown, A. R. (1999) On subgrid models and filter operations in large eddy simulations. *J. Atmos. Sci.* **56**, 2101–2114.
- McComb, W. D. (1990) *The Physics of Fluid Turbulence*. Oxford University Press, Oxford.
- Mellor, G. L. and Yamada, T. (1974) A hierarchy of turbulence closure models for planetary boundary layer. *J. Atmos. Sci.* **31**, 1791–1806.
- Mellor, G. L. and Yamada, T. (1982) Development of a turbulence closure model for geophysical fluid problems. *Rev. Geophys. Space Phys.* **20**, 851–875.
- Mesinger, F. and Arakawa, A. (1976) *Numerical methods used in atmospheric models*, vol. 1. GARP Publ. Series.
- Métais, O. and Ferziger, J., editors (1997) *New tools in turbulence modelling*. Springer-Verlag Berlin Heidelberg New York.

- Müller, E., Foken, T., Heise, E., and Majewski, M. (1995) *LITFASS - a nucleus for a BALTEX field experiment*. Arbeitsergebnisse 33, Deutscher Wetterdienst- Forschung und Entwicklung.
- Müller, G. and Chlond, A. (1996) Three-dimensional numerical study of cell-broadening during cold-air outbreaks. *Boundary-Layer Meteorology* **81**, 289–323.
- Moeng, C.-H. (1984) A large-eddy simulation model for the study of planetary boundary-layer turbulence. *J. Atmos. Sci.* **41**, 2052–2062.
- Moeng, C.-H., Cotton, W. R., Bretherton, C., Chlond, A., Khairoutdinov, M., Krueger, S., Lewellen, W. S., MacVean, M. K., Pasquier, J. R. M., Rand, H. A., Siebesma, A. P., Stevens, B., and Sykes, R. I. (1996) Simulation of a stratocumulus-topped planetary boundary layer: Intercomparison among different numerical codes. *Bull. Amer. Meteorol. Soc.* **77**, 261–278.
- Moeng, C.-H. and Randall, D. A. (1984) Problems in simulating the stratocumulus-topped boundary layer with a third-order closure model. *J. Atmos. Sci.* **41**, 1588–1600.
- Moeng, C.-H. and Sullivan, P. P. (1994) A comparison of shear-and buoyancy-driven planetary boundary layer flows. *J. Atmos. Sci.* **51**, 999–1022.
- Moeng, C.-H. and Wyngaard, J. C. (1986) An analysis of closures for pressure-scalar covariances in the convective boundary layer. *J. Atmos. Sci.* **43**, 2499–2513.
- Moeng, C.-H. and Wyngaard, J. C. (1988) Spectral analysis of large-eddy simulations in the convective boundary layer. *J. Atmos. Sci.* **45**, 3573–3587.
- Monin, A. S. and Yaglom, A. M. (1975) *Statistical Fluid Mechanics: Mechanics of Turbulence*. MIT Press, Cambridge, MA.
- Morcrette, J. J. (1991) Evaluation of model-generated cloudiness: Satellite observed and model-generated diurnal variability of brightness temperature. *Mon. Wea. Rev.* **119**, 1205–1224.
- Muschinski, A. (1996) A similarity theory of locally homogeneous and isotropic turbulence generated by a Smagorinsky-type LES. *J. Fluid Mech.* **325**, 239–260.
- Nakanishi, M. (2001) Improvement of the mellor-yamada turbulence closure model based on large-eddy simulation data. *Boundary-Layer Meteorology* **99**, 349–378.
- Nieuwstadt, F. T. M., Mason, P. J., Moeng, C.-H., and Schumann, U. (1993) Large-eddy simulation of the convective boundary layer: A comparison of four computer codes. In *Turbulent shear flows*, vol. 8, Springer Edition, pp. 343–367.
- O'Brien, J. J. (1970) A note on the vertical structure of the eddy exchange coefficient in the planetary boundary layer. *J. Atmos. Sci.* **27**, 1213–1215.
- Panchev, S. (1971) *Random Functions and Turbulence*. Pergamon Press, Oxford.

- Perera, M., Fernando, H., and Boyer, D. L. (1994) Turbulent mixing at an inversion layer. *J. Fluid Mech.* **267**, 275–298.
- Piacsek, S. A. and Williams, G. P. (1970) Conservation properties of convection difference schemes. *J. Comput. Phys.* **376**, 392–405.
- Pielke, R. A. and Mahrer, Y. (1975) Representation of the heated planetary boundary layer in mesoscale models with coarse vertical resolution. *J. Atmos. Sci.* **32**, 2288–2308.
- Pope, S. B. (2000) *Turbulent flows*. Cambridge University Press.
- Press, W. H., Teukolsky, A. A., Vetterling, W. T., and Flannery, B. P. (1996) *Numerical Recipes in Fortran 77. The Art of Scientific Computing. Volume 1 of Fortran Numerical Recipes*. Cambridge University Press.
- Ramanathan, V., Cess, R., Harrison, E., Minnis, P., Barkstrom, B., Ahmad, E., and Hartmann, D. (1989) Cloud-radiative forcing and climate: Results from the earth radiation budget experiment. *Science* **243**, 57–63.
- Raschendorfer, M. (1999) Quarterly Report of the Operational NWP-Models of the Deutscher Wetterdienst Special topic: The new turbulence parameterization of LM 19, Deutscher Wetterdienst, Business Area Research and Development.
- Renner, E. (2002) The Black Triangle area - Fit for Europe? Numerical air quality studies for the Black Triangle area. *AMBIO* **31**, 231–235.
- Reynolds, W. C. (1990) The potential and limitations of direct and large eddy simulations. In *Whither turbulence? Turbulence at the cross roads*, Springer Edition, pp. 313–343.
- Richardson, L. F. (1922) *Weather Prediction by Numerical Process*. Cambridge University Press, Cambridge.
- Ritter, B. and Geleyn, J.-F. (1992) A comprehensive radiation scheme for numerical weather prediction models with potential applications in climate simulations. *Mon. Wea. Rev.* **120**, 303–325.
- Roca, R., Picon, L., Desbois, M., Treut, H. L., and Morcrette, J.-J. (1997) Direct comparison of METEOSAT water vapor channel data and general circulation model results. *Geophysical Research Letters* **24**, 147–150.
- Schmidt, H. and Schumann, U. (1989) Coherent structure of the convective boundary layer deduced from large-eddy simulation. *J. Fluid Mech.* **200**, 511–562.
- Schraff, C. and Hess, R. (2002) Realisierung der Datenassimilation im LM. *Promet* **27**.
- Schröter, M., Bange, J., and Raasch, S. (2000) Simulated airborne flux measurements in a LES generated convective boundary layer. *Boundary-Layer Meteorology* **95**, 437–456.

- Schumann, U., Hauf, T., Höller, H., Schmidt, H., and Volkert, H. (1987) A mesoscale model for the simulation of turbulence, clouds or flow over mountains: Formulation and validation examples. *Contr. Atmos. Phys.* **61**, 413–446.
- Siebesma, A. and Cuijpers, J. (1995) Evaluation of parametric assumptions for shallow cumulus convection. *J. Atmos. Sci.* **52**, 650–666.
- Siebesma, A. P., Bretherton, C. S., Brown, A. R., Chlond, A., Cuxart, J., Duynkerke, P. G., Jiang, H., Khairoutdinov, M., Lewellen, D. C., Moeng, C.-H., Stevens, B., and Stevens, D. E. (2002) A large-eddy simulation intercomparison study of shallow cumulus convection. *J. Atmos. Sci.* Accepted.
- Sommeria, G. and Deardorff, J. W. (1977) Subgrid-scale condensation in models of nonprecipitating clouds. *J. Atmos. Sci.* **34**, 344–355.
- Steppeler, J., Bitzer, H.-W., Minotte, M., and Bonaventura, L. (2002) Nonhydrostatic atmospheric modeling using a z-coordinate representation. *Mon. Wea. Rev.* **130**, 2143 – 2149.
- Stevens, B. and Lenschow, D. H. (2001) Observations, experiments and large-eddy simulation. *Bull. Amer. Meteorol. Soc.* **82**, 283–294.
- Stevens, D. E., Ackerman, A. S., and Bretherton, C. S. (2002) Effects of domain size and numerical resolution on the simulation of shallow cumulus convection. *J. Atmos. Sci.* **59**, 3285–3301.
- Stull, R. (1984) Transient turbulence theory. Part I: The concept of eddy-mixing across finite distances. *J. Atmos. Sci.* **41**, 3351–3367.
- Stull, R. (1993) Review of non-local mixing in turbulent atmospheres: Transient theory. *Boundary-Layer Meteorology* **62**, 21–96.
- Stull, R. B. (1997) *An Introduction to Boundary Layer Meteorology*. Kluwer Academic Publishers, Dordrecht/ Boston/ London.
- Stull, R. B. and Driedonks, A. G. M. (1987) Applications of transient turbulence parameterization to atmospheric boundary-layer simulations. *Boundary-Layer Meteorology* **40**, 209–239.
- Sullivan, P. P., Moeng, C.-H., Stevens, B., Lenschow, D. H., and Mayor, S. D. (1998) Structure of the entrainment zone capping the convective atmospheric boundary layer. *J. Atmos. Sci.* **55**, 3042–3064.
- Sun, W. Y. and Chang, C.-Z. (1986) Diffusion model for a convective layer. Part I: Numerical simulation of convective boundary layer. *J. Climate Appl. Meteor.* **25**, 1445–1453.
- Sykes, R. I., Lewellen, W. S., and Henn, D. S. (1988) A numerical study of the development of cloud street spacing. *J. Atmos. Sci.* **45**, 2556–2569.

- Taylor, K. E. (2001) Summarizing multiple aspects of model performance in a single diagram. *J. Geophys. Res.* **106**, 7183–7192.
- Therry, G. and Lacarrère, P. (1983) Improving the eddy kinetic energy model for planetary boundary layer description. *Boundary-Layer Meteorology* **25**, 63–88.
- Tiedtke, M. (1989) A comprehensive mass flux scheme for cumulus parameterisation in large-scale models. *Mon. Wea. Rev.* **117**, 1779–1799.
- Troen, I. and Mahrt, L. (1986) A simple model of the atmospheric boundary layer; sensitivity to surface evaporation. *Boundary-Layer Meteorology* **37**, 129–148.
- Vogel, G. and Schubert, U. (2002) Deutscher Wetterdienst, pers. comm.
- Wergen, W. (2002) Datenassimilation - ein Überblick. *Promet* **27**. Available at <http://www.dwd.de/de/Funde/Analyse/Assimilation/Assimilation.html>.
- WGBU (1995) *Scenario for the derivation of global CO₂ reduction targets and implementation strategies. Statement on the occasion of the first conference of the parties to the framework convention on climate change in Berlin*. German Advisory Council on Global Change (WGBU): Annual Report 1995. WGBU, Bremerhaven.
- WGBU (1996) *World in Transition: The Research Challenge*. German Advisory Council on Global Change (WGBU): Annual Report 1996. Springer: Berlin, Heidelberg, New York.
- Williams, G. P. (1969) Numerical integration of the three-dimensional Navier-Stokes equations for incompressible flows. *J. Fluid Mech.* **37**, 727–750.
- Williams, T. and Kelly, C. (1995) *Gnuplot – An Interactive Plotting Program*. Version 3.6.
- Willis, G. E. and Deardorff, J. W. (1974) A laboratory model of the unstable planetary boundary layer. *J. Atmos. Sci.* **31**, 1297–1307.
- Wulfmeyer, V. (1999) Investigations of humidity skewness and variance profiles in the convective boundary layer and comparison of the latter with large eddy simulation results. *J. Atmos. Sci.* **56**, 1077–1087.
- Wyngaard, J. C. and Brost, R. A. (1984) Top-down bottom-up diffusion of a scalar in the convective boundary layer. *J. Atmos. Sci.* **41**, 102–112.
- Wyngaard, J. C. and Coté, O. R. (1974) The evolution of a convective planetary boundary Layer. A higher-order-closure model study. *Boundary-Layer Meteorology* **7**, 289–308.
- Xue, M., Zong, J., and Droegemeier, K. K. (1996) Parameterization of PBL turbulence in a multi-scale nonhydrostatic model. In *11th Conf. on Num. Wea. Prediction, Norfolk, VA*. Ameri. Meteor. Soc.

- Yamada, T. (1983) Simulations of nocturnal drainage flows by a q^2l turbulence closure model. *J. Atmos. Sci.* **40**, 91–106.
- Zilitinkevich, S., Gryanik, V. M., Lykossov, V. N., and Mironov, D. V. (1999) Third-order transport and nonlocal turbulence closures for convective boundary layers. *J. Atmos. Sci.* **56**, 3463–3477.

Danksagung

Mein herzlicher Dank gilt allen, die mich während der Promotion unterstützend begleitet haben. Besonders danke ich Herrn Prof. E. Renner, dass er mir durch die Bereitstellung des interessanten Themas und sein förderndes Interesse die Promotion in der Abteilung Modellierung des Leibniz-Instituts für Troposphärenforschung ermöglicht hat.

Meinem Betreuer, Olaf Hellmuth, danke ich ganz besonders für die fachliche Unterstützung und die ausgezeichnete Zusammenarbeit während der gesamten Promotion. Für die Bereitstellung des Grobstrukturmodells (LES), gilt mein besonderer Dank Andreas Chlond und Herrn Prof. Graßl (Max-Planck-Institut für Meteorologie, Hamburg). Ohne die konstruktiven Hinweise von Andreas Chlond und Frank Müller zu Struktur und Initialisierung des Grobstrukturmodells wäre dessen erfolgreiche Implementierung am IfT nicht möglich gewesen.

Mein Dank gilt auch Herrn Dr. Z. Janjic (National Centers for Environmental Prediction, USA) und Herrn Dr. Raschendorfer (Deutscher Wetterdienst) für ihre wertvollen Hinweise und Anregungen zur Verbesserung der Turbulenzparameterisierung nach Mellor-Yamada. Tijana Janjic und Hans-Stefan Bauer (Universität Hohenheim) danke ich für die konstruktiven Diskussionen über mikro- und mesoskalige Simulationen.

Eine Verifizierung der Ergebnisse aus den Grobstruktursimulationen mit experimentellen Messergebnissen wäre nicht möglich gewesen, ohne die Bereitstellung von Daten durch Herrn Dr. R. Kaiser, Herrn Dr. E. Fedorovich und Herrn Dr. P. Durand, denen ich dafür herzlich danke. Für die Unterstützung während der Simulationsläufe des mesoskaligen Lokal-Modells (LM) sowie für die wertvollen Hinweise aus den konstruktiven Diskussionen danke besonders Herrn Dr. H.-J. Herzog und Herrn Dr. G. Vogel (Meteorologisches Observatorium des Deutschen Wetterdienstes, Potsdam). Darüberhinaus sei an dieser Stelle Frau Dr. U. Schubert und Frau R. Kirchner für die Bereitstellung von Satelliten- und Analysedaten herzlich gedankt.

Viele konstruktive Hinweise zum Manuskript der Dissertation gaben mir Karoline Diehl, Sabine Wurzler und Holger Siebert. Vielen Dank dafür. Desweiteren danke ich allen Mitarbeitern der Abteilung Modellierung für das gute Arbeitsklima und die vielfältige Unterstützung durch Anregungen und Diskussionen. An dieser Stelle sei besonders Barbara Heide für die Unterstützung bei der Berechnung synthetischer Satellitendaten, Kerstin Müller für die Unterstützung bei der Recherche und Beschaffung von Literatur sowie Wolfram Schröder und Birgit Heinrich für die Hilfe bei der Datenkonvertierung und Auswertung der Analysedaten gedankt. Ohne die Betreuung der IT-Infrastruktur durch Frank Riedel und Thomas Jagemann hätten die zahlreichen Simulationsläufe nicht so reibungslos über Nacht laufen können.

Den Doktoranden des Institutes danke ich für die vielfältigen Anregungen und Diskussion im Rahmen der Doktorandenvorträge und darüber hinaus. Besonders danke ich meinen Mitstreitern im Zimmer 113 für die angenehme Arbeitsatmosphäre und die gute Zusammenarbeit.

Ein besonders herzlicher Dank gilt meiner "Kattl" sowie meinen Familie(n), die mir Kraft, Unterstützung und Motivation während aller Phasen der Promotion gegeben haben.

Lebenslauf

Name: Jürgen Helmert
Geburtsdatum: 02. 09. 1973
Geburtsort: Karl-Marx-Stadt
Wohnort: Lilienweg 4
09648 Altmittweida



Schulbildung

1980 - 1990
Allgemeinbildende polytechnische Oberschule
Abschluß: mittlere Reife

Berufsbildung

1990 - 1993
Höhere Berufsfachschule Jena-Göschwitz
Ausbildung zum staatlich geprüften physikalisch-technischen Assistenten mit fachgebundener Hochschulreife
Abschlußarbeit zum Thema: „Hologramm-Interferometrische Mikroskopie als Meßverfahren in der Mikrosystemtechnik“

Hochschulbildung

1994 - 1999
Universität Leipzig
Studiengang Physik/Diplom
Diplomarbeit zum Thema: „Zur Parametrisierung der Mächtigkeit der Entrainmentschicht unter Verwendung von Large-Eddy-Simulations- und LIDAR-Daten“

Berufstätigkeit

seit November 1999
Wissenschaftlicher Mitarbeiter am Leibniz-Institut für Troposphärenforschung, Leipzig
Dissertation zum Thema: "Determination of characteristic turbulence length scales from large-eddy simulation of the convective planetary boundary layer“

Bibliographische Beschreibung

Helmert, Jürgen

Determination of characteristic turbulence length scales from
large-eddy simulation of the convective planetary boundary layer

(Bestimmung charakteristischer Turbulenzlängenskalen basierend auf
Grobstruktursimulationen der konvektiven planetaren Grenzschicht)

Universität Leipzig, Dissertation

117 S., 172 Lit., 36 Abb., 14 Tab.

Referat:

Turbulente Austauschprozesse in der atmosphärischen Grenzschicht spielen eine Schlüsselrolle beim vertikalen Impuls-, Energie- und Stofftransport in der Erdatmosphäre. In meso- und globalskaligen Atmosphärenmodellen sind turbulente Austauschprozesse jedoch subskalig und müssen unter Verwendung geeigneter Schliessungsansätze parametrisiert werden. Hierbei spielt die Spezifikation der charakteristischen Turbulenzlängenskala in Abhängigkeit vom Stabilitätszustand der Atmosphäre eine entscheidende Rolle. Gegenwärtig verwendete Ansätze, die auf der Verwendung der turbulenten Mischungslänge für neutrale Schichtung sowie dimensionsloser Stabilitätsfunktionen basieren, zeigen vor allem Defizite im oberen Bereich der konvektiven Grenzschicht sowie in der Entrainmentzone, wo starke vertikale Gradienten auftreten.

In der vorliegenden Arbeit wurden hochaufgelöste dreidimensionale Grobstruktursimulationen der trockenen und feuchten Grenzschicht für ein weites Spektrum von Stabilitätsbedingungen durchgeführt. Erste und zweite Momente atmosphärischer Strömungsvariablen wurden aus den simulierten hydro- und thermodynamischen Feldern berechnet und diskutiert.

Die Spektraleigenschaften turbulenter Fluktuationen der Strömungsvariablen, das raumzeitliche Verhalten kohärenter Strukturen sowie charakteristische Turbulenzlängenskalen wurden abgeleitet. Eine Verifizierung der charakteristischen Turbulenzlängenskalen erfolgte durch Vergleich mit Ergebnissen früherer numerischer Simulationen, mit Turbulenzmessungen in der atmosphärischen Grenzschicht sowie mit Laborexperimenten.

Mit Hilfe der nichtlinearen Datenmodellierung wurden leicht verwendbare Approximationen der charakteristischen Turbulenzlängenskalen abgeleitet und deren statistische Signifikanz diskutiert. Unter Verwendung dieser Approximationen wurde ein existierendes Parametrisierungsmodell revidiert und mit Hilfe von Grobstruktursimulationen verifiziert.

Desweiteren wurde der Einfluß der turbulenten Mischungslänge auf die Prognose mesokaliger Felder untersucht. Hierzu wurde mit dem Lokal-Modell des Deutschen Wetterdienstes eine entsprechende Sensitivitätsstudie durchgeführt. Anhand von Satellitendaten und Analysedaten aus der 4D-Datenassimilation wurden die Simulationsergebnisse verifiziert.